

STRATEGIC REENTRY TECHNOLOGY PROGRAM, PHASE II
(STREET-Aii)

FINAL REPORT
VOLUME I

TASK 4.2

A Two-Layer Model of High Speed Two- and Three-Dimensional Turbulent
Boundary Layers with Pressure Gradient and Surface Mass Injection.

Prepared by

AVCO GOVERNMENT PRODUCTS GROUP
AVCO SYSTEMS DIVISION
201 Lowell Street
Wilmington, Massachusetts 01887

AVSD-C474-71-RR, Vol. I
Contract F04701-C-0002
CDRL ITEM A005

71

November 1971

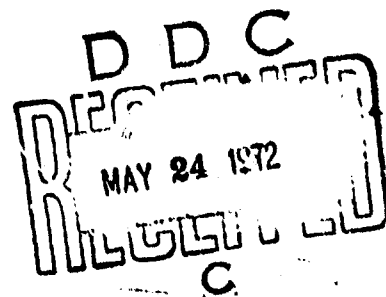
THIS DOCUMENT IS APPROVED FOR PUBLIC RELEASE;
DISTRIBUTION UNLIMITED.

"THE VIEWS AND CONCLUSIONS CONTAINED IN THIS DOCUMENT ARE
THOSE OF THE AUTHORS AND SHOULD NOT BE INTERPRETED AS
NECESSARILY REPRESENTING THE OFFICIAL POLICIES, EITHER
EXPRESSED OR IMPLIED, OF THE ADVANCED RESEARCH PROJECTS
AGENCY OR THE UNITED STATES GOVERNMENT."

Prepared for

SPACE AND MISSILE SYSTEMS ORGANIZATION
DEPUTY FOR REENTRY SYSTEMS
AIR FORCE SYSTEMS COMMAND
Norton Air Force Base, California 92409

Reproduced by
NATIONAL TECHNICAL
INFORMATION SERVICE
U S Department of Commerce
Springfield VA 22151



Unclassified

Security Classification

DOCUMENT CONTROL DATA - R & D

(Security classification of title, body of abstract and indexing annotation must be entered when the overall report is classified)

1. ORIGINATING ACTIVITY (Corporate author) Avco Government Products Group Avco Systems Division 201 Lowell Street, Wilmington, Massachusetts		2a. REPORT SECURITY CLASSIFICATION None	
		2b. GROUP	
3. REPORT TITLE Strategic Reentry Technology Program, Phase II (STREET-AII) Final Report, Volume I, Task 4.2			
4. DESCRIPTIVE NOTES (Type of report and inclusive dates) Final Report, Vol. I			
5. AUTHOR(S) (First name, middle initial, last name)			
6. REPORT DATE November 1971		7a. TOTAL NO. OF PAGES 92	7b. NO. OF ILLUSTRATIONS 36
8a. CONTRACT OR GRANT NO. F04701-C-0002, CDRL Item AC05		8b. ORIGINATOR'S REPORT NUMBER(S) AVSD-0474-71-RR, Vol. I	
8c. PROJECT NO. 71		8d. OTHER REPORT NO(S) (Any other numbers that may be assigned this report) SAMSO-TR-72-25	
10. DISTRIBUTION STATEMENT This document is approved for public release; distribution unlimited.			
11. SUPPLEMENTARY NOTES		12. SPONSORING MILITARY ACTIVITY Space and Missile Systems Organization Deputy for Reentry Systems Air Force Systems Command Norton Air Force Base, California 92439	
13. ABSTRACT <p>A two-layer model of the three-dimensional compressible turbulent boundary layer is developed which is applicable to flows with pressure gradient and surface mass transfer. The model is based on the small cross-flow approximation in which the spreading metric is determined by the inviscid streamline pattern. A modified Mangler transformation is employed which permits transformation of the boundary layer equations to a two-dimensional form without transforming the turbulent stress or heat flux. It turns out that the computational speed of the method is rapid enough to enable equation for the inviscid stream reflection to be coupled with the present method for calculation of strong (supercritical) interactions, such as in the region downstream of the critical point to re-attaching flows or in regions of strong blowing.</p> <p>Solution of the inner (wall) layer for the velocity and enthalpy is obtained using mixing length theory and the thin layer jet model. This solution is obtained without using a compressibility transformation and leads to a generalized law of the wall with mass injection. The stress and heat flux in the inner layer are found by enforcing the law of the wall into the full conservation equations and integrating away from the surface. In the outer wake layer, an integral momentum method is used along with appropriate matching conditions with the inner layer. This report shows that the dynamics of the turbulent boundary layer depends on the coupling and interaction of the inner and outer layers. In fact, the model is really designed to bring out the nature of this inner and outer layer interaction.</p> <p>Several solutions and experimental comparisons are presented. In particular, the effect of positive and negative pressure gradients on the relative scale of the inner and outer layers is demonstrated as well as the effect on the stagnation enthalpy-velocity relationship. Results are presented for relaxing flows where C_f and $h_{f,1}$ initially are far from their equilibrium values. Solutions for boundary layers far out of fluid dynamic equilibrium such as flow over an abrupt expansion and flow over a wavy wall are also given.</p> <p>The theory is compared with a number of experiments for both uniform and discontinuous distributions of surface mass injection. Solutions have been obtained for values of M_∞, ρ_∞, μ_∞ as large as 0.95, which is well into the range of massive blowing. Results are also presented for ablation and transpiration cooling where the injection distribution is determined by an energy balance along the surface.</p>			

DD FORM 1473
1 NOV 65

Unclassified

Security Classification

Unclassified

Security Classification

14.	KEY WORDS	LINK A		LINK B		LINK C	
		ROLE	WT	ROLE	WT	ROLE	WT
	Strategic Reentry Technology Program, Phase II Two-Layer Model of High Speed Two- and Three-Dimensional Turbulent Boundary Layers with Pressure Gradient and Surface Mass Injection						

Unclassified

Security Classification

SAMSO-TR-72-25

STRATEGIC REENTRY TECHNOLOGY PROGRAM, PHASE II
(STREET-A II)

FINAL REPORT
VOLUME I

TASK 4.2

A Two-Layer Model of High Speed Two- and Three-Dimensional Turbulent
Boundary Layers with Pressure Gradient and Surface Mass Injection.

Prepared by

AVCO GOVERNMENT PRODUCTS GROUP
AVCO SYSTEMS DIVISION
201 Lowell Street
Wilmington, Massachusetts 01887

Technical Report
No. SAMSO-TR-72-25

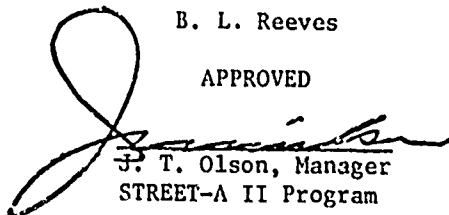
AVSD-0474-71-RR, Vol. I
Contract F04701-71-C-0002
CDRL ITEM A005

November 1971

by

B. L. Reeves

APPROVED



J. T. Olson, Manager
STREET-A II Program

THIS DOCUMENT IS APPROVED FOR PUBLIC RELEASE;
DISTRIBUTION UNLIMITED.

"THE VIEWS AND CONCLUSIONS CONTAINED IN THIS DOCUMENT ARE
THOSE OF THE AUTHORS AND SHOULD NOT BE INTERPRETED AS
NECESSARILY REPRESENTING THE OFFICIAL POLICIES, EITHER EX-
PRESSED OR IMPLIED, OF THE ADVANCED RESEARCH PROJECTS AGENCY
OR THE UNITED STATES GOVERNMENT"

Prepared for

SPACE AND MISSILE SYSTEMS ORGANIZATION
DEPUTY FOR REENTRY SYSTEMS
AIR FORCE SYSTEMS COMMAND
Norton Air Force Base, California 90409

FOREWORD

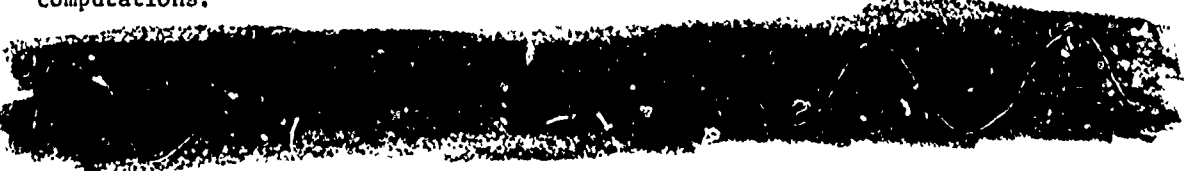
This is the final report on the Strategic Reentry Technology Program Phase II (STREET-AII). A two-layer model of high-speed two- and three-dimensional turbulent boundary layers with pressure gradient and surface mass injection is presented.

A complete description of the turbulent boundary layer computer program, including a program listing, is available in a separate AVCO/SAMSO document.

This research was sponsored by the Advanced Research Projects Agency of the Department of Defense (ARPA Order 1359) and by the Space and Missile Systems Organization, Air Force Systems Command, under Contract F04701-71-C-0002. Captain R. Padfield (RNSE) served as Project Officer during the first half of the effort. Captain M. L. Anderson (RNSE) is the current Project Officer.

ACKNOWLEDGEMENTS

The author expresses his appreciation to Mr. H. Baum and Mr. D. Siegelman for their many helpful discussions during the early stages of this work, and to Mr. H. Buss for writing the computer program and assisting with some of the computations.



Capt. M. L. Anderson, STREET-AII
Project Officer, RNSE
Air Force Systems Command
Norton AFB, California

ABSTRACT

A two-layer model of the three-dimensional compressible turbulent boundary layer is developed which is applicable to flows with pressure gradient and surface mass transfer. The model is based on the small cross-flow approximation in which the spreading metric is determined by the inviscid streamline pattern. A modified Mangler transformation is employed which permits transformation of the boundary layer equations to a two-dimensional form without transforming the turbulent stress or heat flux. It turns out that the computational speed of the method is rapid enough to enable equations for the inviscid stream deflection to be coupled with the present method for calculations of strong (supercritical) interactions, such as in the region downstream of the critical point in re-attaching flows or in regions of strong blowing.

Solution of the inner (wall) layer for the velocity and enthalpy is obtained using mixing length theory and the thin layer Couette model. This solution is obtained without using a compressibility transformation and leads to a generalized law of the wall with mass injection. The stress and heat flux in the inner layer are found by inserting the law of the wall into the full conservation equations and integrating away from the surface. In the outer wake layer, an integral moment method is used along with appropriate matching conditions with the inner layer. This report shows that the dynamics of the turbulent boundary layer depends on the coupling and interaction of the inner and outer layers. In fact, the model is really designed to bring out the nature of this inner and outer layer interaction.

Several solutions and experimental comparisons are presented. In particular, the effect of positive and negative pressure gradients on the relative scale of the inner and outer layers is demonstrated as well as the effect on the stagnation enthalpy-velocity relationship. Results are presented for relaxing flows where \tilde{C}_f and $(2\tilde{C}_H/C_f)$ initially are far from their equilibrium values. Solutions for boundary layers far out of fluid dynamic equilibrium such as flow over an abrupt expansion and flow over a wavy wall are also given.

The theory is compared with a number of experiments for both uniform and discontinuous distributions of surface mass injection. Solutions have been obtained for values of $M = \rho_w v_w / \rho_e u_e$ as large as 0.05, which is well into the range of massive blowing. Results are also presented for ablation and transpiration cooling where the injection distribution is determined by an energy balance along the surface.

CONTENTS

1.0 INTRODUCTION	1
2.0 TURBULENT BOUNDARY LAYER MODEL	3
2.1 Equations of Motion and Coordinate Systems	3
2.2 Turbulence Model	5
3.0 SOLUTION OF INNER LAYER AND MATCHING CONDITIONS	9
4.0 MOMENT INTEGRAL METHOD FOR OUTER LAYER	15
5.0 INITIAL CONDITIONS AND INTEGRAL THICKNESSES	19
6.0 FINAL VELOCITY AND ENTHALPY PROFILES	21
7.0 COMPUTER RESULTS AND EXPERIMENTAL COMPARISONS	25
7.1 Results for Zero Injection	25
7.2 Results for Uniform and Discontinuous Distributions of Surface Mass Injection	45
7.2.1 Ablation and Transpiration Cooling: Solutions for Flows with the Mass Injection Distribution Determined by an Energy Balance at the Surface	53
8.0 CONCLUDING REMARKS	55
9.0 REFERENCES	57

APPENDICES

1 MATCHING CONDITIONS	61
2 INTEGRAL FUNCTIONS FOR MOMENT EQUATIONS IN OUTER LAYER	69
3 ENTRAINMENT AND OTHER SWALLOWING RELATIONSHIPS	71

ILLUSTRATIONS

Figure 1	α Variation with M_e , H_w , v_w Obtained from Experimental Values of \bar{B}	22
2	Relaxing Flow - Abrupt Removal of Positive Pressure Gradient, $M_e = 0$	26
3	Comparison of Law of the Wall with Data for Surface Mass Injection	26
4	\tilde{C}_f versus Re_θ for Equilibrium $dP/dx = 0$	27
5	Effect of M_e on \tilde{C}_f	27
6	Relaxing Flows at $M_e = \text{Constant} = 2.6$	29
7	Relaxing Flow - Initial $H \neq A+BU$, $M_e = 3.6$ $H_w/H_e = 0.5$	29
8a	Effect of dP/dx on \tilde{C}_f	30
8b	Effect of dP/dx on θ and Velocity Ratio at Match Point	30
8c	Effect of dP/dx on H versus U Profile and on Reynolds Analogy	30
9	Comparison with Data, $dP/dx < 0$	31
10	Comparison with Data, $dP/dx < 0$	31
11	Comparison of Two-Layer Model with Bradshaw Method, $H_w/H_e = 0.9$, $Re_{\theta_0} = 10^3$	32
12	Comparison with Lewis, Strong Positive and Negative Pressure Gradients	32
13	Comparison with Lewis, Moderate Pressure Gradient.....	33
14	Theoretical \tilde{C}_f Variations for Experiments Performed by Lewis	33
15	Comparison with Data, $dP/dx < 0$	35
16	Comparison with Data on an Axisymmetric Compression Surface .	35
17	Comparison with Data on an Axisymmetric Compression Surface .	36
18	Waisted Body of Revolution	36
19	Waisted Body of Revolution	36

ILLUSTRATIONS (Cont'd)

Figure 20	Relaxation Produced by Change in Spreading Metric: Effect of Cone Angle for a Given Initial Profile	37
21a	Effect of Angle of Attack on Boundary Layer Thickness on Nose Tip, $M_\infty = 16$	37
21b	Boundary Layer Momentum Thickness on Nose Tip	38
21c	Mach Number, Stanton Number, and Skin Friction on Nose Tip, $M_\infty = 16$	38
22	Effect of Initial \tilde{C}_f and $2 C_H/\tilde{C}_f$ on \tilde{C}_f Variation with Re_θ at $M_e = 9.37$, Zero Pressure Gradient	41
23	Local Flow Properties for a Turbulent Boundary Layer over a Wavy Wall	41
24	Effect of Surface Roughness on Turbulent Boundary Layer on Sharp Cone	43
25	Relaminarizing Flow: Heat Transfer Distribution on a Sharp Biconic	43
26	Relaminarizing Flow: Heat Transfer Distribution on a Sharp Biconic	44
27	Relaminarizing Flow: Heat Transfer Distribution on a Sharp Biconic	44
28	Effect of Blowing on \tilde{C}_f for Incompressible Flow	47
29	Variation of \tilde{C}_f with Blowing	47
30	Variation of \tilde{C}_f with Blowing at Mach 6.7	47
31	Form Parameter Comparison, $dp/dx = 0$	48
32	Variation of δ^*/θ with Blowing at Mach 6.7	48
33	Variations of θ and δ^* at $M_e = 2.5$	49
34	Variations of θ and δ^* at $M_e = 3.5$	49
35	Momentum Thickness Distributions on a Sharp Cone at Mach 8 ..	50
36	Discontinuous Decrease in Blowing, Incompressible Flow	51
37	Discontinuous Increase in Blowing, Incompressible Flow	51
38	Velocity Profiles with Injection, $M_e = 0$	52

ILLUSTRATIONS (Concl'd)

Figure 39	Velocity Profiles with Injection, $M_e = 3.5$	52
40	Blowing and Heating Distributions Around a Spherical Nose with Coupled Energy Balance at the Surface	54
41	Skin Friction Variations in a Negative Pressure Gradient with $\omega = 1, 2,$ and 3 in Turbulent Production Integral, α_0	56

LIST OF SYMBOLS

Symbols

a	sonic velocity
a^*	$(1 - \bar{U}_m)$
A^2	parameter in Crocco integral for wall layer, Eq. (24)
A_i	coefficients defined in Appendix 2
B	parameter in Crocco integral for wall layer, Eq. (25)
\bar{B}	empirical "constant" in law of the wall
B_i	coefficients defined in Appendix 2
C_f	skin friction coefficient, Eq. (38), $\tilde{C}_f = 2C_f$
C_f'	$(u_r/u_e)^2$ or $(h_w/h_e) C_f$
C_H	Stanton number
C_p	specific heat at constant pressure
E_i	coefficients defined in Appendix 2
F	inverse turbulent Reynolds number in outer layer, Eq. (48)
h	static enthalpy
h^+	h/h_w
H	stagnation enthalpy
\bar{H}	H/H_e
I_i	coefficients defined in Appendix 2
J_i	flux integrals in inner layer, Eqs. (30) and (33), (34)
K	empirical constant in law of the wall, $K = 0.40$
ℓ	mixing length
L	reference length in coordinate transformation, Eq. (6)
M_e	Mach number at edge of boundary layer
m	exponent of stagnation enthalpy profiles in outer layer, Eq. (36)

LIST OF SYMBOLS (Cont'd)

Symbols (Cont'd)

m_e	$[(\gamma - 1)/2] M_e^2$
m	mass flux in inner layer
M	surface mass injection parameter $\rho_w \tilde{v}_w / \rho_e \tilde{u}_e$
n	exponent of velocity profiles in outer layer, Eq. (35)
p	static pressure
Pr_L	molecular Prandtl number
Pr_t	turbulent Prandtl number
q	heat flux
$r(\tilde{x})$	spreading metric of inviscid streamlines
Re_y	$y^+ / (u_r / u_e)$
St	modified Stanton number, Eq. (37)
\tilde{u}, \tilde{v}	velocity components in physical coordinates \tilde{x}, \tilde{y} , respectively
u, v	velocity components in transformed, "two-dimensional" coordinates x, y , respectively
U, V	velocity components in transformed, constant density coordinates X, Y , respectively
\bar{U}	U / U_e
\tilde{u}^+	\tilde{u} / \tilde{u}_r
\tilde{u}_r	friction velocity, $(\tau_w / \rho_w)^{1/2}$
$y_m(x)$	thickness of inner layer (match point)
\tilde{y}^+	$\tilde{u}_r \tilde{y} / \nu_w$
γ	ratio of specific heats
δ	thickness of outer layer in transformed, constant density coordinates X, Y
δ_e	thickness of boundary layer (two-dimensional)
δ_i^*	"incompressible" displacement thickness
δ^*	displacement thickness (two-dimensional)
$\tilde{\delta}_e, \tilde{\delta}^*$	thickness and displacement thickness in physical coordinates
ϵ	turbulent eddy viscosity

LIST OF SYMBOLS (Concl'd)

Symbols (Concl'd)

σ	exponent in temperature viscosity law, $\mu \sim T^\sigma$
η	normalized coordinate in outer layer, Eq. (39)
θ	momentum thickness (two-dimensional)
$\tilde{\theta}$	momentum thickness in physical coordinates
μ	viscosity
ν	kinematic viscosity
ξ	\tilde{u}/\tilde{u}_e
ρ	density
τ	stress
Φ	dimensionless mixing length function, Eq. (56)
ψ	stream function
ω	exponent in eddy viscosity variation across outer layer, Eq. (46)

Subscripts

e	edge of boundary layer
m	at match point y_m
o	isentropic stagnation conditions behind normal shock, also initial conditions
s	local stagnation conditions at edge of layer
w	wall conditions
aw	adiabatic wall conditions

TASK 4.3

A TWO-LAYER MODEL OF HIGH SPEED TWO- AND THREE-DIMENSIONAL TURBULENT BOUNDARY LAYERS WITH PRESSURE GRADIENT AND SURFACE MASS INJECTION.

1.0 INTRODUCTION

Accurate prediction of turbulent boundary layers about reentry bodies is of critical importance in calculating wall friction and heat transfer, observables (initial conditions for near wake calculations), communication (guidance, and telemetry), and reentry aerodynamics in general. Recently, interest in maneuvering and lifting reentry vehicles has placed added emphasis on developing methods for predicting three-dimensional turbulent boundary layers over bodies at angle of attack and for predicting turbulent boundary layer separation and reattachment. Separation occurring on control surfaces and on the leeward side of bodies at angle of attack are problems of much interest, but are flows for which current theories are either incomplete or inadequate. For example, the wake-like model of turbulent separation and reattachment¹ has yet to be extended to three-dimensional flows, and the model itself is incapable of treating the important region downstream of the critical point in two-dimensional reattaching flows.

The objective of this task is to produce a method which will yield wall conditions and boundary layer profiles sufficiently accurate for subsequent calculations of electron concentration through a three-dimensional turbulent boundary layer. The work is aimed at computing flow fields around arbitrary bodies at angle of attack, with particular emphasis on calculating boundary layers in strong positive and negative pressure gradients with surface mass injection. Entropy layer swallowing in regions downstream of a blunted nose is also being considered.

A two-layer model has been developed for this purpose in which an analytical solution for the inner layer, based on a compressible law of the wall, is matched with a moment integral method in the outer layer. Solution of the inner layer is obtained without the use of a compressibility transformation. In the outer layer the explicit appearance of the density is removed from the convection terms in the conservation equations without transforming the turbulent stress and heat flux.

The model is based on the tacit assumption that the inner and outer layers can be treated distinctly, but that as the flow proceeds downstream the two layers are free to interact with one another. In fact, the model is intended to bring out the nature of this inner and outer layer interaction. The relative scale of the inner and outer layers (location of the match point \tilde{y}_m) is computed as an integral property of the flow, similar to the calculation of the momentum thickness and displacement thickness, and depends on the upstream history of the layer. At separation, for example, which now can be predicted by the model if the pressure distribution is prescribed, $\tilde{C}_f \rightarrow 0$, $\tilde{y}_m/\delta_c \rightarrow 0$ and $(u/u_c)_m \rightarrow 0$ so that the boundary layer is dominated by the outer layer (or dominated by the "wake component" in the terminology of Coles²). One of the unique features

of the model is that the stability of the system of ordinary differential equations can be used to establish upper and lower bounds on the turbulent production integral $\int \tau du$ in the outer layer. Stable solutions up to Mach 10 for a wide range of wall to free stream temperature ratios show that compressibility has little effect on the properly normalized lateral stress profiles, confirming the results of Maise and McDonald.³

The computational speed of the method is sufficiently rapid that the whole boundary layer flow field on bodies at angle of attack can be calculated (except, of course, the leeward side at large angles of attack). It also appears that the computational speed is rapid enough to permit calculations of supercritical boundary layer-inviscid stream interactions.

The model is based on the small cross-flow approximation in which the boundary layer equations are solved along inviscid streamlines. In this coordinate system the cross-flow component of velocity in the layer is uncoupled from the streamwise momentum and energy equations and can be ignored as long as the approximation is valid. For flow around bodies at angle of attack, inviscid streamline patterns and the spreading metric are computed by integrating the inviscid momentum equation normal to inviscid streamlines on the body using either experimental or calculated inviscid pressure distributions.⁴

2.0 TURBULENT BOUNDARY LAYER MODEL

2.1 EQUATIONS OF MOTION AND COORDINATE SYSTEMS

If the boundary layer equations are written following inviscid streamlines and the cross flow in the boundary layer normal to the local inviscid streamline direction can be assumed small, the mean flow equations are

$$\frac{\partial}{\partial \tilde{x}} (\rho \tilde{u} r) + \frac{\partial}{\partial \tilde{y}} (\rho \tilde{v} r) = 0 \quad (1)$$

$$\rho \tilde{u} \frac{\partial \tilde{u}}{\partial \tilde{x}} + \rho \tilde{v} \frac{\partial \tilde{u}}{\partial \tilde{y}} = - \frac{d P_e}{d \tilde{x}} + \frac{\partial r}{\partial \tilde{y}} \quad (2)$$

$$\rho \tilde{u} \frac{\partial H}{\partial \tilde{x}} + \rho \tilde{v} \frac{\partial H}{\partial \tilde{y}} = \frac{\partial}{\partial \tilde{y}} (q + \tilde{u} r) \quad (3)$$

where $r(\tilde{x})$ is the spreading metric determined by the inviscid flow streamline geometry. Here, because the cross-flow component of velocity is assumed small, the uncoupled cross-flow momentum equation is ignored and it is further assumed that the additional contributions to turbulent stress and heat flux resulting from fluctuations in the cross flow velocity are likewise small.

Thus,

$$r = \mu \frac{\partial \tilde{u}}{\partial \tilde{y}} - \rho \overline{u'v'} \quad (4)$$

and

$$q = k \frac{\partial h}{\partial \tilde{y}} - \rho \overline{v'h'} \quad (5)$$

Clearly, for a body at large angle of attack these stress and heat flux models will break down in a region on the leeward side because strong cross flows with additional contributions to the Reynolds stress would have to be included along with interaction with the outer flow.

The explicit appearance of the spreading metric in the equations of motion can be eliminated by means of a modified Mangler transformation. Although it turns out that $r(\tilde{x})$ later appears in a constant of integration in the compressible law of the wall, the transformation is convenient since it is possible to remove r from the continuity equation without transforming the stress or heat flux. Letting

$$dx = \frac{r(\tilde{x})}{L} d\tilde{x} \text{ and } dy = \frac{r(\tilde{x})}{L} d\tilde{y} \quad (6)$$

with

$$u = \tilde{u}, \quad v = \tilde{v} + \frac{\tilde{u} \tilde{y}}{r} \frac{dr}{d\tilde{x}} \quad (7)$$

Eqs. (1) through (3) become

$$\frac{\partial(\rho u)}{\partial x} + \frac{\partial(\rho v)}{\partial y} = 0 \quad (8)$$

$$\rho u \frac{\partial u}{\partial x} + \rho v \frac{\partial u}{\partial y} = - \frac{dp_e}{dx} + \frac{\partial r}{\partial y} \quad (9)$$

$$\rho u \frac{\partial H}{\partial x} + \rho v \frac{\partial H}{\partial y} = \frac{\partial}{\partial y} (q + u r) \quad (10)$$

where r and q are still defined by Eqs. (4) and (5). Solution of the inner layer is obtained directly using Eqs. (8) - (10) without further transformation of the coordinates to remove the explicit appearance of the density. The reason for this is twofold. First, within the framework of the present model for the inner layer an analytic solution can be obtained without introducing a compressibility transformation. Thus, no useful simplification would be provided by such a transformation. Second, Maise and McDonald³ have shown that a compressibility transformation leads to generally poor results for the turbulent stress distributions across the boundary layer even for constant pressure, adiabatic flows. They also showed poor correlation of experimental velocity profiles using the transformation for constant pressure flows with heat transfer. More recently, Lewis, et. al.⁵ attempted to generalize Coles' transformation but they also found significant deviation between experimental velocity profiles and profiles predicted using the transformation, especially in the wall layer. They showed that the discrepancy between profiles increased with increasing Mach number so that for flow on a flat plate at Mach 6, for example, a difference of 20 percent in velocity profiles can be expected. Although not all of this discrepancy should be attributed to the transformation, there appears to be little justification for using it in the wall layer, particularly in flows with heat transfer and pressure gradient.

In the outer wake-like layer, however, where we use an integral moment method, a simple compressibility transformation is used to remove the explicit appearance of the density from Eqs. (8) through (10). This can be accomplished without transforming the stress and heat flux by letting

$$dX = dx, \quad dY = \frac{a_c}{a_o} \frac{\rho}{\rho_o} dy \quad (11)$$

$$\Psi = \psi, \quad U = (a_o/a_e)u \quad (12)$$

$$V = \frac{\rho}{\rho_o} v + U \frac{\partial Y}{\partial x}$$

so that Eqs. (8) through (10) become

$$\frac{\partial U}{\partial X} + \frac{\partial V}{\partial Y} = 0 \quad (13)$$

$$U \frac{\partial U}{\partial X} + V \frac{\partial U}{\partial Y} = (H/H_e) U_e \frac{dU_e}{dX} + \frac{a_o}{a_e \rho_o} \frac{\partial r}{\partial Y} \quad (14)$$

$$U \frac{\partial H}{\partial X} + V \frac{\partial H}{\partial Y} = \frac{1}{\rho_o} \frac{\partial}{\partial Y} \left(q + \frac{a_e}{a_o} U r \right) \quad (15)$$

Here r and q are still the physical stress and heat flux defined by Eqs. (4) and (5). Eqs. (13) through (15) are used to develop the integral moment equations for the outer layer.

With the equations of motion and proper coordinate systems developed for the inner and outer layers, we now proceed to the turbulence model used in the two-layer model.

2.2 TURBULENCE MODEL

In order to develop a scheme for integrating Eqs. (1) through (3), or their transformed counterparts Eqs. (8) through (10), it is necessary to have some knowledge either of the relationships between r , q and the mean flow quantities p , u , H (provided such relationships exist) or have additional independent differential equations for r and q . Several model equations^{6,7} for the stress and heat flux based on the latter approach have been developed recently and, hopefully, these will provide new insight into the way the stress and heat flux respond to changes in boundary conditions as the flow proceeds downstream. To date, however, all these approaches using differential equations for r and q have had to invoke assumptions for closure of the unknown correlation functions which are either pure hypothesis or whose physical basis has only been demonstrated in incompressible flows. At moderate Mach numbers, however, say up to $M_e \approx 7$ there is considerable experimental evidence that the turbulent boundary layer may be divided into an inner wall layer and an outer wake layer, as in incompressible flow. In the wall layer the properly normalized experimental velocity and enthalpy profiles have been shown to be functions of the local wall stress, heat flux and injection rate and except for the streamwise variations of these quantities are more or less independent of the upstream history of the layer.^{8,9} This is precisely the result predicted by mixing length theory and the thin layer, Couette model, which leads to a compressible law of the wall and a Crocco integral for the inner layer. For flows with surface mass injection Danberg and Squire have shown that this same model accurately predicts the velocity distribution in the

wall layer. In fact, the experimental evidence for the Van Driest¹⁰ form of the law of the wall for $M = 0$ and the Squire form of this law for $M \neq 0$ is now so strong that the model equations for the turbulent stress either "reduce" to this law near the wall or are matched to it.

In this paper a first approximation for the velocity and enthalpy profiles in the inner layer is used in which the laminar sublayer and transition layer is neglected and the flow is assumed to be fully turbulent to the wall. Maise and McDonald have shown that in this region the mixing length varies linearly away from the surface, i.e. $l = K \tilde{y}$ with $K = 0.40$, for Mach numbers up to about five. Thus, with the additional assumption that $Pr_t = 1$ in the first approximation, the stress and heat flux in the inner layer are

$$\tau \approx \rho K^2 \tilde{y}^2 (\partial \tilde{u} / \partial \tilde{y})^2 \quad (16)$$

$$q \approx \rho K^2 \tilde{y}^2 (\partial \tilde{u} / \partial \tilde{y}) (\partial h / \partial \tilde{y}) \quad (17)$$

The error incurred in computing integral properties such as θ and the wall stress by neglecting the sublayer is small, except, perhaps, in very strong negative pressure gradients. Second approximation profiles are subsequently computed which include the laminar contribution to the total stress and are not restricted to $Pr_t = 1$ or $Pr_L = 1$.

Even for flows in positive or negative pressure gradients there is considerable experimental evidence that the law of the wall gives an accurate representation of the velocity profile over some distance \tilde{y}_m away from the surface. If we accept the generalized law of the wall as being applicable to flows with surface mass injection and pressure gradient, the remaining questions to be answered insofar as the inner layer is concerned are (a) the determination of the lateral stress and heat flux profiles, which are required for matching with the outer layer, and (b) calculation of the distance from the surface \tilde{y}_m at which the velocity profile departs from the law of the wall. Following Coles'² suggestion for incompressible flows, the stress and heat flux profiles are found by inserting the wall law into the full momentum and energy equations and integrating these equations away from the surface. In this way the stress and heat flux in the inner layer depend on the past history of the layer as well as on local properties, and are unhooked from a purely local determination through mixing length and the local velocity gradient.

The determination of the length scale \tilde{y}_m results from a consideration of the matching or interaction of the inner and outer layers. Thus, attention is turned to the outer layer where the evaluation of the stress and heat flux is much more questionable. Bradshaw concluded, from his measurements in relaxing incompressible boundary layers, that the stress in the outer layer depends on the whole history of the layer and cannot be found from local mean flow properties as in equilibrium layers. Thus, according to Bradshaw and others, the use of an eddy viscosity or mixing length theory in the outer layer of rapidly adjusting flows must be held suspect because for these flows there is no simple relationship between the turbulent stress and mean velocity gradient. If this is the case, then the relative scale of the inner and outer layers, \tilde{y}_m , likewise cannot be determined from the local velocity gradient, as is usually assumed

in conventional finite difference methods,^{11,12} for example, but must be found from the whole history of the flow. In the present theory we have attempted to avoid using a simple local relation for determining $\tilde{\gamma}_m$. By taking a higher moment of the momentum equation, $\tilde{\gamma}_m$ is found as one of the integral properties of flow.

In the present two-layer model it turns out that a relation for the stress along the match point $\tilde{\gamma}_m$ is required along with a relation for the "production" integral in the outer layer

$$\int (r/r_m) du$$

The stress along the match point is evaluated using an eddy viscosity normalized by the constant density displacement thickness, as was suggested by the calculations of Maise and McDonald. Thus along $\tilde{\gamma}_m$

$$\tau_m = \rho_m \epsilon_m (\partial \tilde{u} / \partial \tilde{y})_m \quad (18)$$

where

$$\epsilon = F u_e \tilde{\delta}_i^* , \quad F = \text{constant} \quad (19)$$

Thus, while the evaluation of τ_m is subject to some of the objections of "localness", the location of the match point $\tilde{\gamma}_m$ where τ_m is evaluated depends on the upstream history of the layer.

Because the turbulent boundary layer has been divided into two more or less distinct layers which are free to interact with one another, the present model might be expected to reveal certain consequences of this inner and outer layer interaction that are not quite so apparent in other models. Indeed, this turns out to be true because the two-layer model provides upper and lower bounds on the magnitude of the turbulent production integral over the outer layer. If estimates for this integral are made which are too small or too large, integrations of the system of equations downstream develop instabilities where $n \rightarrow 0$ for the former and $n \rightarrow \infty$ for the latter. Thus, we find that the production integral over the outer layer cannot be assumed negligibly small nor can it be evaluated using a constant eddy viscosity across the outer layer, as was suggested by Clauser.¹³ Both assumptions give unstable solutions, although the Clauser assumption is stable for Mach numbers below about 2.5.

Thus we find that the stability of the system of equations, which reflects on the stability of the interaction between the inner and outer layers, provides a means of evaluating the production integral over the outer layer. This is a most useful and important result because the production integral contains the influence of turbulent intermittency at the boundary layer edge and the effects of long-time stress "memory" of large eddies in flows which are far from equilibrium. By evaluating the production integral as though the density were constant across the outer layer and by using a cubic variation of ϵ between $\tilde{\gamma}_m$ and $\tilde{\delta}_e$ with $\epsilon \rightarrow 0$ at the outer edge, stable solutions have been obtained up to Mach 10

for wall to free stream stagnation temperature ratios between 0.05 and 1.0. These results for the bounds on the production integral and the assumptions used to produce stable solutions verify to some extent the results of Maise and McDonald who showed that compressibility has little effect on the lateral stress profiles (when normalized by the wall stress) up to about Mach 5. A cubic variation of ϵ for $\tilde{y}_m < \tilde{y} < \tilde{\delta}_e$ is also consistent with the ϵ variations inferred by Maise and McDonald³ and Bradshaw.¹⁴

3.0 SOLUTION OF INNER LAYER AND MATCHING CONDITIONS

Experiments in compressible turbulent boundary layers with moderate pressure gradients and surface mass injection have shown that even at hypersonic speeds there is an inner (wall) layer in which velocity and temperature gradients normal to the surface are so large that terms involving x derivatives in the conservation equations are generally negligible. The lateral extent of this inner layer \tilde{y}_m at any given point \tilde{x} is determined by previous history of the layer and by local conditions such as magnitude and sign of the pressure gradient or strength of injection. In large positive pressure gradients or with large blowing the extent of the inner layer may become vanishingly small, while in negative pressure gradients \tilde{y}_m may approach the edge of the layer.

With mixing length theory used to determine the stress and heat flux, and a thin layer Couette model of the flow near the wall, a generalized law of the wall for the velocity and enthalpy with surface mass injection is obtained. These velocity and enthalpy profiles are then inserted back into the full continuity, momentum and energy equations, which are integrated away from the surface to give the stress, heat flux and mass flux at the outer edge of the inner layer. This operation "unhooks" the stress and heat flux from purely local quantities such as the velocity and enthalpy gradients. The velocity, enthalpy, stress, heat flux and mass flux at the edge of the wall layer can be obtained analytically, and these expressions, along with certain auxiliary relations for normal and streamwise derivatives of the velocity and enthalpy, are used for matching with the integral method in the outer layer. One of the key features of the present two layer model is that the integral equations in the outer layer ultimately determine the lateral extent of the wall layer (or in Coles' terminology the strength of the wake component); it is not specified implicitly in advance in terms of the eddy viscosity or mixing length variation as in virtually all other methods.

With the possible exception of boundary layers in very strong pressure gradients we assume that a wall layer exists in which $\ell = K\tilde{y}$ and the velocity and enthalpy profiles are closely approximated by a Couette flow model. Neglecting the laminar sublayer (in the first approximation) and setting $Pr_t = 1$, the equations for the stress and heat flux obtained by integrating the momentum and energy equations away from the surface are

$$\tau(\tilde{y}) = \tau_w + \rho_w \tilde{v}_w \tilde{u} = \rho K^2 \tilde{y}^2 \left(\frac{\partial \tilde{u}}{\partial \tilde{y}} \right)^2 \quad (20)$$

$$q(\tilde{y}) = q_w - \tilde{u} \tau(\tilde{y}) + \rho_w \tilde{v}_w (H - H_w) = \rho K^2 \tilde{y}^2 \left(\frac{\partial \tilde{u}}{\partial \tilde{y}} \right) \left(\frac{\partial h}{\partial \tilde{y}} \right) \quad (21)$$

Dividing the second equation by the first and integrating the result gives a Crocco integral, which is always valid in the inner layer, independent of pressure gradient or surface mass injection.

$$H/H_w = 1 + B (\tilde{u}/\tilde{u}_e) \quad (22)$$

or

$$h/h_w = 1 + B (\tilde{u}/\tilde{u}_e) - A^2 (\tilde{u}/\tilde{u}_e)^2 \quad (23)$$

where

$$A^2 = [m_e / (1 + m_e)] (H_e / H_w) \quad (24)$$

$$B = [2 m_e / (1 + m_e)] (H_e / H_w) (St / C_f) \quad (25)$$

Substituting for $\rho = \rho_w (h_w / h)$ in the expression for $r(\tilde{y})$, defining $M \equiv \rho_w \tilde{u}_w / \rho_e \tilde{u}_e$ and integrating from the edge of the laminar sublayer to any point $\tilde{y}^+ \equiv \tilde{y} u_r / \nu_w$, with $\xi \equiv \tilde{u} / \tilde{u}_e$, gives

$$\int_{\xi_s}^{\xi} \frac{d\xi}{[(h/h_w)(C_f + M\xi)]^{1/2}} = \left[(1 + m_e) \frac{H_w}{H_e} \right]^{1/2} \frac{1}{K} \ln \frac{\tilde{y}^+}{\tilde{y}_s^+}$$

which can be written, after changing the limits of integration

$$(h_w/h_e)^{-1/2} \int_0^{\xi} \frac{d\xi}{[(h/h_w)(C_f + M\xi)]^{1/2}} = \frac{1}{K} \ln \tilde{y}^+ + \bar{B}$$

where \bar{B} is the empirical "constant"

$$\bar{B} \equiv - \frac{1}{K} \ln \tilde{y}_s^+ + (h_w/h_e)^{-1/2} \int_0^{\xi_s} \frac{d\xi}{[(h/h_w)(C_f + M\xi)]^{1/2}}$$

Whereas in incompressible flow $\bar{B} \approx 5$, the experiments of Danberg and Squire at supersonic speeds have demonstrated that \bar{B} is a function of M and H_w/H_e , which can be approximated by the curve fits*:

$$\left. \begin{aligned} 0 < M_e < 3.5 : \bar{B}/\bar{B}_{M=0} &= 1 - 0.6 \times 10^3 M (M_e/3.5)^{3/2} \\ M_e > 3.5 : \bar{B}/\bar{B}_{M=0} &= 1 - 0.6 \times 10^3 M \end{aligned} \right\} \bar{B} \geq 0$$

with

$$M_e > 5 : \bar{B}_{M=0} = 5 + 8 (1 - H_w/H_e),$$

$$M_e < 5 : \bar{B}_{M=0} = 5 + 8 \left(1 - \frac{H_w}{H_e} \right) \left(\frac{M_e}{5} \right)$$

* A linear extrapolation of \bar{B} data presented in Danberg was used for $H_w/H_e < 0.5$. Profile data is desperately needed to verify (or modify) the values of \bar{B} (and values of α , Section 6.0) that are indicated for highly cooled walls.

Defining*

$$C_1 = (B - \sqrt{B^2 + 4A^2})/2A^2, \quad C_2 = (B + \sqrt{B^2 + 4A^2})/2A^2$$

$$C_3 = C_f/M, \quad k^2 = (C_2 - C_1)/(C_3 + C_2), \quad \sin^2 \theta = (C_2 - \xi)/(C_2 - C_1)$$

and since $\ln \tilde{y}^+ = \ln y^+ + \ln L/t$

the compressible law of the wall becomes

$$-2 \left[\frac{h_e/h_w}{A^2 M (C_3 + C_2)} \right]^{1/2} [\mathcal{F}(\theta, k) - \mathcal{F}(\theta_{\xi=0}, k)] = \frac{1}{K} \ln [(C_f')^{1/2} Re_y] + \frac{1}{K} \ln \frac{L}{r} + \bar{B} \quad (26)$$

where

$$\mathcal{F}(\theta, k) = \int_0^\theta \frac{d\theta}{(1 - k^2 \sin^2 \theta)^{1/2}} \quad (27)$$

$$y^+ = y u_\tau / \nu_w = (C_f')^{1/2} Re_y \quad (28)$$

$$Re_y = \frac{\rho_s}{\rho_o} \left(\frac{\rho_o a_o}{\mu_o} \right) \left(\frac{H_e}{H_w} \right)^{(1+\sigma)} (1+m_e)^{-\frac{(3\gamma-1)}{2(\gamma-1)}} M_e y \quad (29)$$

For $M=0, k=0$ and the elliptic integrals $\mathcal{F}(\theta, k)$ reduce to arcsin functions, and the law of the wall is given by the Van Driest "generalized" velocity distribution.¹⁰ Evaluating the law of the wall at y_m gives the velocity ratio $(u/u_e)_m = \bar{U}_m$ along the match point. Actually, what we require for matching with the outer layer is the streamwise derivative of $(u/u_e)_m$, which is found by differentiating the law of the wall.

With the velocity profile given by the law of the wall and the enthalpy profile given by the Crocco integral in the inner layer, exact expressions for the stress and heat flux at y_m can be obtained by integrating the momentum and energy equations away from the surface, i.e.,

*For large blowing, $\sin^2 \theta$ and k^2 are redefined, i.e. $k^2 = (C_3 + C_2)/(C_2 - C_1)$ and $\sin^2 \theta = (C_2 - \xi)/(C_2 + C_3)$ so that k^2 is always less than one.

$$\begin{aligned}
r_m - r_w &= \frac{dp}{dx} y_m + \int_0^{y_m} \left(\rho u \frac{\partial u}{\partial x} + \rho v \frac{\partial u}{\partial y} \right) dy \\
&= \frac{dp}{dx} y_m + \frac{d}{dx} \int_0^{y_m} \rho u (u - u_m) dy + \int_0^{y_m} \rho u dy \cdot \frac{du_m}{dx} + \rho_w v_w u_m
\end{aligned}$$

and

$$\begin{aligned}
(q + ur)_m - q_w &= \int_0^{y_m} \left(\rho u \frac{\partial H}{\partial x} + \rho v \frac{\partial H}{\partial y} \right) dy \\
&= \frac{d}{dx} \left[\frac{H_w B}{u_e} \int_0^{y_m} \rho u (u - u_m) dy \right] + \int_0^{y_m} \rho u dy \cdot \frac{dH_m}{dx} + \left(\frac{H_w B}{u_e} \right) \rho_w v_w u_m
\end{aligned}$$

where the integrals in these expressions are evaluated using Eqs. (23) and (26).
For example, if

$$J_1 = \int_0^{y_m} \frac{\rho u}{\rho_w u_e} dy \quad \text{and} \quad J_2 = \int_0^{y_m} \frac{\rho u}{\rho_w u_e} \left(\frac{u}{u_e} - \frac{u_m}{u_e} \right) dy \quad (30)$$

then

$$J_i = \frac{K v_w}{u_r} \frac{u_e}{u_r} e^{-K\bar{B}} \int_0^{\bar{U}_m} \frac{j_i \exp[af(\xi)]}{(h/h_w)^{3/2} \left(1 + \frac{M}{C_f} \xi \right)^{1/2}} d\xi \quad (31)$$

which can be integrated repeatedly by parts if

$$a = K(u_e/u_r), \quad Z = \exp[af(\xi)]$$

$$f(\xi) = \int_0^{\bar{U}_m} \frac{d\xi}{(h/h_w)^{1/2} \left(1 + \frac{M}{C_f} \xi\right)^{1/2}}, \quad g(\xi) = \frac{J_i}{a(h/h_w)}$$

$$j_i = \xi \text{ for } J_1, \quad j_i = \xi(\xi - \bar{U}_m) \text{ for } J_2$$

to give

$$\int g(\xi) dz = \exp[af(\xi)] \left\{ g(\xi) - \frac{g'(\xi)}{af'(\xi)} + \frac{1}{a^2 f'(\xi)} \frac{d}{d\xi} \left(\frac{g'}{f'} \right) - \dots \right\} \quad (32)$$

where $\frac{1}{a} \sim 0(C_f^{1/2}) < 1$. By approximating $h/h_w \approx h_m/h_w$ in $f(\xi)$ and $g(\xi)$ and $\left(1 + \frac{M}{C_f} \xi\right) \approx \left(1 + \frac{M}{C_f} \bar{U}_m\right)$ in $f(\xi)$ the above series truncates with the term $O(\alpha^{-1})$ for J_1 , and $O(\alpha^{-2})$ for J_2 so that*

$$J_1 = \frac{\bar{U}_m y_m}{(h_m/h_w)} - \frac{1}{K} \left(\frac{u_r}{u_e} \right) \frac{y_m}{(h_m/h_w)^{1/2}} \left(1 + \frac{M}{C_f} \bar{U}_m \right)^{1/2} \quad (33)$$

$$J_2 = - \frac{1}{K} \left(\frac{u_r}{u_e} \right) \frac{\bar{U}_m y_m}{(h_m/h_w)^{1/2}} \left(1 + \frac{M}{C_f} \bar{U}_m \right)^{1/2} + \frac{2}{K^2} \left(\frac{u_r}{u_e} \right)^2 y_m \left(1 + \frac{M}{C_f} \bar{U}_m \right) \quad (34)$$

The expressions for J_1 and J_2 are the key results for the evaluation of the stress, heat flux and mass flux in the inner layer. With J_1 and J_2 given by Eqs. (33) and (34) the evaluation of r_m and $(q + ur)_m$ is straightforward (although somewhat lengthy) and the results are given in Appendix 1.

Solution of wall layer for the velocity, enthalpy, stress and heat flux has been obtained analytically in terms of the given wall and edge conditions ($M_e, H_w/H_e$ and M); three "parameters" (y_m, C_f and St), and two empirical "constants" (K and \bar{B}). By matching this inner solution with an integral moment method for the outer layer the three "parameters" y_m, C_f and St are determined. In addition to $u/u_e, H/H_e, r$ and $q, \partial u/\partial y$ and $\partial H/\partial y$ are also matched. These expressions are given in Appendix 1 along with certain other auxiliary expressions (such as $d\bar{U}_m/dx, d\bar{H}_m/dx$, etc.) required for the matching.

* These approximations yield identical results for the leading term of the series as the exact expressions for f and g , and are used here merely to simplify the task of differentiating J_2 .

4.0 MOMENT INTEGRAL METHOD FOR OUTER LAYER

In order to determine the relative scale of the inner and outer layers, y_m , and the quantities r_m and q_m , which are related to the quantities of interest, namely C_f and St , in the equations given in Appendix 1, a moment integral method is used in the outer layer. In this layer independent two-parameter families of profiles are chosen for u and H . The "free" parameters of the profiles are determined implicitly by matching with relations obtained for the inner layer (law of the wall and Crocco integral) for u and H and the lateral and streamwise derivatives of these quantities along the unknown match point y_m . The profiles selected are power-laws of the form

$$\bar{U} \equiv U/U_e = 1 - (1 - \bar{U}_m)(1 - \eta)^n, \quad n > 0 \quad (35)$$

$$\bar{H} \equiv H/H_e = 1 - (1 - \bar{H}_m)(1 - \eta)^m, \quad m > 0 \quad (36)$$

so that very "full" profiles without overshoot are possible with $n, m \gg 1$. In order for a Crocco integral to exist in the outer layer m must equal n but in general this will not be true. In fact, in terms of the more conventional definitions

$$C_H \equiv -q_w / (H_w - H_e) \rho_e u_e = \frac{2 m_e St}{(1 + m_e)(1 - H_w/H_e)} \quad (37)$$

$$\tilde{C}_f \equiv 2 r_w / \rho_e u_e^2 = 2 C_f \quad (38)$$

it is easy to show, using Eq. (A 1-2) and the definition of B that a Crocco integral ($m = n$) exists in the outer layer only when the Reynolds analogy holds, i.e., when $C_H = \tilde{C}_f / 2$.

In the above profile families

$$\eta \equiv (Y - Y_m) / \delta \quad (39)$$

where δ is the thickness of the outer layer in the transformed coordinate

$$Y - Y_m = \int_{y_m}^y \frac{a_e \rho}{a_o \rho_o} dy \quad (40)$$

Because the momentum and energy equations are satisfied exactly in the inner layer using the law of the wall (Eqs. (A1-5) and A1-6), no new information would be obtained by integrating the conservation equations and velocity moment across the inner layer. The momentum integral, first velocity moment and energy integral for the outer layer are obtained by integrating the transformed conservation equations from $Y = Y_m$ to $Y = Y_m + \delta$.

Momentum Integral - Outer Layer

$$\left. \begin{aligned} -\delta A_1 \frac{d\bar{U}_m}{dx} + \delta A_2 \frac{dn}{dx} + I_5 \frac{d\delta}{dx} + (\rho_s/\rho_o)(1+m_e)^{\frac{-(\gamma+1)}{2(\gamma-1)}} \cdot M(1-\bar{U}_m) \\ -(1-\bar{U}_m) \left(\frac{1}{\rho_o U_e} \frac{d\dot{m}}{dx} \right) = (E_1 - I_5 - I_2) \frac{\delta}{M_e} \frac{dM_e}{dx} - \left(\frac{a_o}{U_e^2 a_e \rho_o} \right) r_m \end{aligned} \right\} \quad (41)$$

First Velocity Moment - Outer Layer

$$\left. \begin{aligned} -\delta A_3 \frac{d\bar{U}_m}{dx} + \delta A_4 \frac{dn}{dx} + I_6 \frac{d\delta}{dx} + (\rho_s/\rho_o)(1+m_e)^{\frac{-(\gamma+1)}{2(\gamma-1)}} \cdot M(1-\bar{U}_m^2) \\ -(1-\bar{U}_m^2) \left(\frac{1}{\rho_o U_e} \frac{d\dot{m}}{dx} \right) = (2E_2 - I_6 - 2I_3) \frac{\delta}{M_e} \frac{dM_e}{dx} \\ - 2 \left(\frac{a_o}{U_e^2 a_e \rho_o} \right) r_m (\bar{U}_m + a_o) \end{aligned} \right\} \quad (42)$$

Energy Integral - Outer Layer

$$\begin{aligned} -\delta B_3 \frac{d\bar{U}_m}{dx} + \delta B_4 \frac{dn}{dx} + E_4 \frac{d\delta}{dx} + \delta B_1 \frac{d\bar{H}_m}{dx} + \delta B_2 \frac{dm}{dx} \\ + (\rho_s/\rho_o)(1+m_e)^{\frac{-(\gamma+1)}{2(\gamma-1)}} \cdot M(1-\bar{H}_m) - (1-\bar{H}_m) \left(\frac{1}{\rho_o U_e} \frac{d\dot{m}}{dx} \right) \\ = -E_4 \frac{\delta}{M_e} \frac{dM_e}{dx} - \left(\frac{1}{\rho_o U_e H_e} \right) q_m - \left(\frac{a_e}{\rho_o a_o H_e} \right) \bar{U}_m r_m \end{aligned} \quad (43)$$

where the integral functions A_i , B_i , E_i and I_i are given in Appendix 2. The equations for $\dot{m}/\rho_o U_e$ and the normalized stress and heat flux at y_m , obtained from the inner layer, are given in Appendix 1. The term involving the integral of the turbulent stress across the outer layer in the velocity moment (the turbulent production) is

$$\alpha_0 = \int_0^1 \frac{r}{r_m} \left(\frac{\partial \bar{U}}{\partial \eta} \right) d\eta \quad (44)$$

According to the work of Maise and McDonald, there is virtually no effect of compressibility on the normalized stress distribution, r/r_m , across the turbulent boundary layer. Thus, we can evaluate r/r_m as though the density is constant, i.e.,

$$\frac{r}{r_m} = \left(\frac{\epsilon}{\epsilon_m} \right) \frac{(\partial \bar{U} / \partial \eta)}{(\partial \bar{U} / \partial \eta)_m} \quad (45)$$

Since $\epsilon \rightarrow 0$ at the edge of the layer, the lateral variation of ϵ in the outer layer can be approximated by

$$\epsilon / \epsilon_m = 1 - \eta^\omega \quad (46)$$

where, according to measurements by Bradshaw and the analysis of data for supersonic layers by Maise and McDonald, ω has a value around 2 or 3. On the basis of stability of solutions over a wide range of Mach numbers we tentatively select the value $\omega = 3$. (See discussion in Sections 2 and 8.)

Finally, a relation for r_m is obtained in terms of the eddy viscosity and velocity gradient at the matching point y_m . Following the suggestion of Herring and Mellor and the results of Maise and McDonald, the length scale for the eddy viscosity is the constant density displacement thickness

$$\tilde{\delta}_i^* = \int_0^{\tilde{\delta}_e} (1 - u/u_\infty) d\tilde{y} \quad (47)$$

and

$$\epsilon_m = F u_e \tilde{\delta}_i^*, \quad F \approx 0.018. \quad (48)$$

Then, since

$$r_m = \rho_m \epsilon_m (\partial \tilde{u} / \partial \tilde{y})_m$$

and $(\partial \tilde{u} / \partial \tilde{y})_m$ is known from the solution of the inner layer, the normalized stress along y_m is given by

$$\left(\frac{a_0}{U_e^2 a_e \rho_0} \right) r_m = (\rho_s / \rho_0)^2 (1 + m_e)^{-\frac{(\gamma+1)}{\gamma-1}} \frac{F \cdot (\delta_1^* / \delta) a^* \dot{n}}{[\bar{H}_m + m_e (\bar{H}_m - \bar{U}_m^2)]^2} \quad (49)$$

With the three integral equations for the outer layer, the above equation for r_m , and the matching relations from the inner layer, the system of ordinary differential equations can be integrated downstream. Since the solution of the inner layer involves three "parameters" (C_f , St and γ_m), and the unknown in the outer layer is δ , these four quantities must be specified at the initial station in order to form all other quantities (n , m , etc) and all the initial streamwise derivatives.

5.0 INITIAL CONDITIONS AND INTEGRAL THICKNESS

Instead of having to specify y_m and δ along with C_f and St at the initial station $\tilde{x}=0$, it is more convenient to specify θ and δ_e , the momentum thickness and thickness of the layer. From the equations for J_1 and J_2 in the inner layer and the integral functions in the outer layer one obtains the following:

$$\delta_e = y_m + (\rho_o/\rho_s)(1+m_e) \frac{\gamma+1}{2(\gamma-1)} [(1+m_e)E_1 - m_e I_2] \delta \quad (50)$$

$$\theta = \frac{\bar{U}_m (1 - \bar{U}_m) y_m}{(h_m/h_e)} + \frac{C_f^{1/2} y_m}{K (h_m/h_e)^{1/2}} (2\bar{U}_m - 1) \beta_o - (2/K^2) C_f y_m \beta_o^2 \quad (51)$$

$$+ (\rho_o/\rho_s)(1+m_e) \frac{\gamma+1}{2(\gamma-1)} [I_1 - I_2] \delta$$

$$\delta^* = \left[1 - \frac{\bar{U}_m}{(h_m/h_e)} \right] y_m + \frac{C_f^{1/2} y_m \beta_o}{K (h_m/h_e)^{1/2}} + (\rho_o/\rho_s)(1+m_e) \frac{\gamma+1}{2(\gamma-1)} [(1+m_e)E_1 - m_e I_2 - I_1] \delta \quad (52)$$

$$\delta_i^* = y_m (1 - \bar{U}_m) + (C_f h_m/h_e)^{1/2} (y_m \beta_o/K) + \left(\frac{\rho_o}{\rho_s} \right) (1+m_e) \frac{\gamma+1}{2(\gamma-1)} [(1+m_e)(E_1 - E_2) - m_e(I_2 - I_3)] \delta \quad (53)$$

Also,

$$\delta_e = (r/L) \tilde{\delta}_e, \quad \delta^* = (r/L) \tilde{\delta}^*, \quad \theta = (r/L) \tilde{\theta} \quad (54)$$

By specifying C_f , C_H , δ_e and θ at the initial station, the above expressions and matching conditions are used to calculate the remaining unknowns: y_m , U_m , δ , m , n , H_m , and B .

6.0 FINAL VELOCITY AND ENTHALPY PROFILES

Since at hypersonic speeds the peak boundary layer temperature can occur well within the wall layer, accurate velocity and enthalpy profiles near the wall are required. In order to avoid the logarithmic singularity at the surface given by the law of the wall, the laminar sublayer and transition layer are included in the determination of final profiles (as well as arbitrary laminar and turbulent Prandtl numbers) so that $\tilde{u} = 0$ at $\tilde{y} = 0$. This is accomplished by including the laminar contribution to the total stress and heat flux in the expressions for $\tau(\tilde{y})$ and $q(\tilde{y})$ in the wall layer and by using the Van Driest variation for the dimensionless mixing length Φ , i.e.,

$$\Phi = K \tilde{y}^+ [1 - \exp(-\tilde{y}^+/a)] \quad (55)$$

where

$$\Phi(\tilde{y}^+, a) = \tilde{u}_r \ell / \nu_w. \quad (56)$$

For adiabatic flows with $M = 0$, a is a constant and equals the incompressible value $a = 25$. For cold walls and $M \neq 0$ the experimental velocity profiles of Danberg and Squire show that B decreases with increasing injection and indicate large variations in a . The determination of a from these experimental profiles is discussed below.

Introducing the normalized wall layer variables

$$\tilde{u}^+ = \tilde{u} / \tilde{u}_r, \quad h^+ = h / h_w, \quad \tilde{y}^+ = \tilde{u}_r \tilde{y} / \nu_w$$

the differential equations for \tilde{u}^+ and h^+ obtained from the equations for the total stress and heat flux become

$$\frac{\Phi^2}{h^+} \left(\frac{d\tilde{u}^+}{d\tilde{y}^+} \right)^2 + h^+ \frac{d\tilde{u}^+}{d\tilde{y}^+} = 1 + (\tilde{v}_w / \tilde{u}_r) \tilde{u}^+ \quad (57)$$

$$\left. \begin{aligned} \frac{\Phi^2}{h^+ Pr_t} \left(\frac{d\tilde{u}^+}{d\tilde{y}^+} \right) \left(\frac{dh^+}{d\tilde{y}^+} \right) + \frac{h^+}{Pr_L} \frac{dh^+}{d\tilde{y}^+} &= - \frac{(\tilde{v}_w / \tilde{u}_r)}{M} \left(1 - \frac{H_e}{H_w} \right) C_H \\ &- \left(\frac{m_e}{1 + m_e} \right) \left(\frac{\rho_e H_e}{\rho_w H_w} \right) \tilde{C}_f \left(1 + \frac{\tilde{v}_w \tilde{u}^+}{\tilde{u}_r} \right) \tilde{u}^+ + (\tilde{v}_w / \tilde{u}_r) \left(\frac{H}{H_w} - 1 \right) \end{aligned} \right\} \quad (58)$$

with boundary conditions, $\tilde{y}^+ = 0 : \tilde{u}^+ = 0 ; h^+ = 1$.

The differential equations for \tilde{u}^+ and h^+ need only be solved at selected points in the flow field where accurate profiles near the wall, including the sublayer, are required. Since both boundary conditions for the two first order equations are known at the wall, the solution does not require iteration and is

performed as an auxiliary calculation in the downstream integration of the two-layer equations.

The asymptotic integral of the equation for \tilde{u}^+ for $\tilde{y}^+ \gg 1$ is

$$\int_0^{\tilde{u}^+} \frac{d\tilde{u}^+}{[h^+ (1 + \tilde{v}_w \tilde{u}^+ / \tilde{u}_\tau)]^{1/2}} = \frac{1}{K} \ln \tilde{y}^+ + \bar{B} \quad (59)$$

which, for a given value of α and solution of the differential equations for \tilde{u}^+ and h^+ , can be solved for \bar{B} . By iterating on an assumed value of α and matching the computed \bar{B} with the experimental values reported by Danberg and Squire the variation of α with H_w/H_e and M for various Mach numbers was obtained. (See Figure 1.)

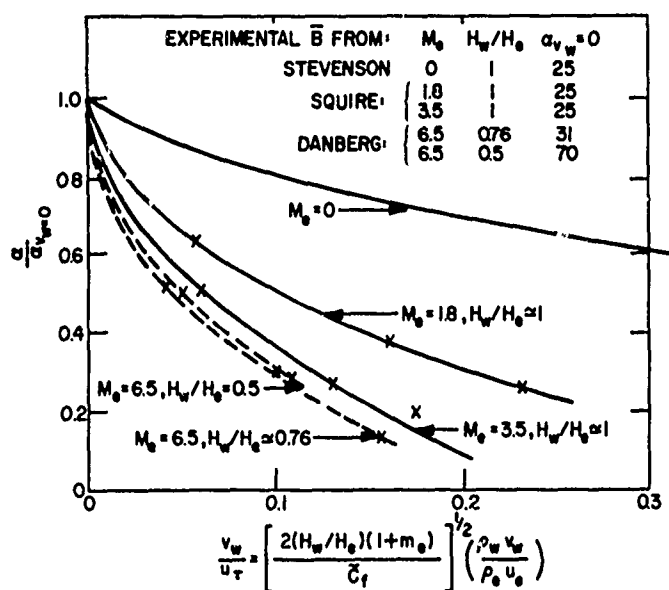


Figure 1 α VARIATION WITH M_e, H_w, v_w OBTAINED FROM EXPERIMENTAL VALUES OF \bar{B}

Eqs. (57) and (58) determine \tilde{u}^+ and h^+ as functions of \tilde{y}^+ in the inner layer, i.e., $0 \leq \tilde{y}^+ \leq \tilde{y}_m^+$. The profiles of \tilde{u}/\tilde{u}_e , h/h_e and H/H_e as functions of \tilde{y} are found from

$$\tilde{u}/\tilde{u}_e = \tilde{u}^+ [(h_w/h_e) C_f]^{1/2} \quad (60)$$

$$h/h_e = h^+ (h_w/h_e) \quad (61)$$

$$H/H_e = (1 + m_e)^{-1} [(h/h_e) + m_e (\tilde{u}/\tilde{u}_e)^2] \quad (62)$$

where

$$\tilde{y} = \tilde{y}^+ \left[\left(\frac{\rho_s}{\rho_o} \right) \left(\frac{\rho_o a_o}{\mu_o} \right) M_e (1 + m_e)^{-\frac{(3\gamma-1)}{2(\gamma-1)}} \left(\frac{H_e}{H_w} \right)^{1+\sigma} (C_f')^{1/2} \right]^{-1} \quad (63)$$

In the outer layer $\tilde{u}/\tilde{u}_e = \bar{U}$ and $H/H_e = \bar{H}$ are calculated using Eqs. (35) and (36) and (h/h_e) is computed from Eq. (62). The distance \tilde{y} is found from Eq. (11).

$$\tilde{y} = \tilde{y}_m + \left(\frac{\rho_o}{\rho_s} \right) (1 + m_e)^{\frac{\gamma+1}{2(\gamma-1)}} \left(\frac{L}{r} \right) \delta \int_0^\eta (h/h_e) d\eta \quad (64)$$

7.0 COMPUTER RESULTS AND EXPERIMENTAL COMPARISONS

7.1 Results for Zero Injection

By specifying initial values for δ_e , θ , \tilde{C}_f and C_H , and also the unit stagnation Reynolds number, where if $\mu \sim T^\sigma$

$$\rho_0 a_0 / \mu_0 = (u_e / \nu_e) \left/ (\rho_s / \rho_0) M_e (1 + m_e) \right.^\sigma \frac{\gamma + 1}{2(\gamma - 1)}$$

Eqs. (23), (26), (50), (51), (A 1-1) and (A 1-2) are solved simultaneously to give all the necessary starting conditions. A set of nine nonlinear differential equations is then integrated to give the solution downstream of the initial station. These differential equations are the momentum, first moment and energy equations for the outer layer, the equation for r_m from the inner layer, and equations obtained by differentiating the relations for \bar{U}_m , \bar{H}_m , m , n and B with respect to x . The method used to solve the system, which is linear when solving for the derivatives, uses Gauss elimination with partial pivoting, with an iterative routine to improve the solution.¹⁵ A comparison of this method of solving systems of linear equations with other techniques is given in Reference 16.

For zero pressure gradient, nonadiabatic flows the average computing time on an IBM 360-75 machine is about 15 seconds for Re_θ to increase by a factor of 10^2 . This is approximately the computing time required by finite difference methods to calculate a single station.¹¹ As of the date of completion of this report, computer runs have been made for adiabatic and cold walls ($0.05 < H_w/H_e < 1$) up to Mach 10, relaxing flows where \tilde{C}_f and/or C_H are far from their equilibrium values initially, boundary layers in strong positive and negative pressure gradients and flows with a varying spreading metric. Comparisons have been made with several of the experiments for incompressible flows reported at the AFOSR-Stanford conference¹⁷ and results for \tilde{C}_f , θ and δ^*/θ compare quite well with most of these experiments. For example, Figure 2 shows a comparison with one of the more interesting experiments -- the relaxing flow from a positive pressure gradient reported by Bradshaw and Ferriss. Momentum balance considerations show that the first experimental value for (at $x = 4.4$ ft.) is probably too small. If the initial θ had been taken to be about 0.475 in. the theoretical curve would have just about passed through the five values of θ measured farther downstream.

Figure 3 shows that Eqs. (57) and (58) yield quite accurate results for the velocity profile in the wall layer with surface mass injection, provided that empirical values of the additive constant \bar{B} are available. These results show that not only is the linear law of the wall, (Eq. (59)), still in evidence with blowing but that the value of y^+ where the profile deviates from a linear law can be represented reasonably well. Here $f(u^+)$ is the integral on the left hand side of Eq. (59).

The variation of the equilibrium flat plate \tilde{C}_f with Re_θ and M_e is compared with several experiments in Figures 4 and 5. These results (with the exception of the experiments by Lee, *et. al.*) are for adiabatic flow, however, the theory predicts a relatively weak effect of wall cooling on skin friction. At Mach 6

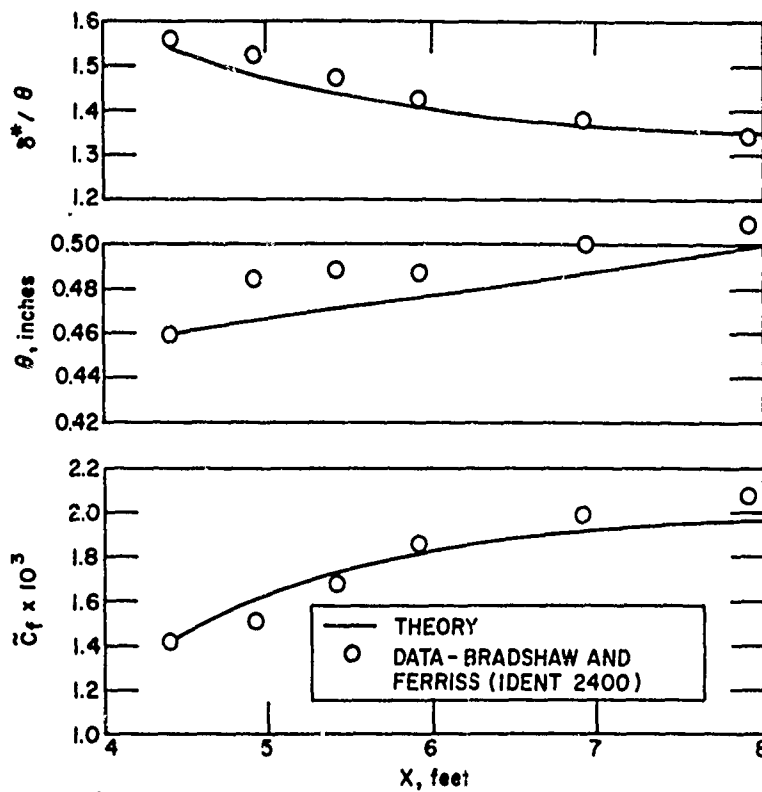
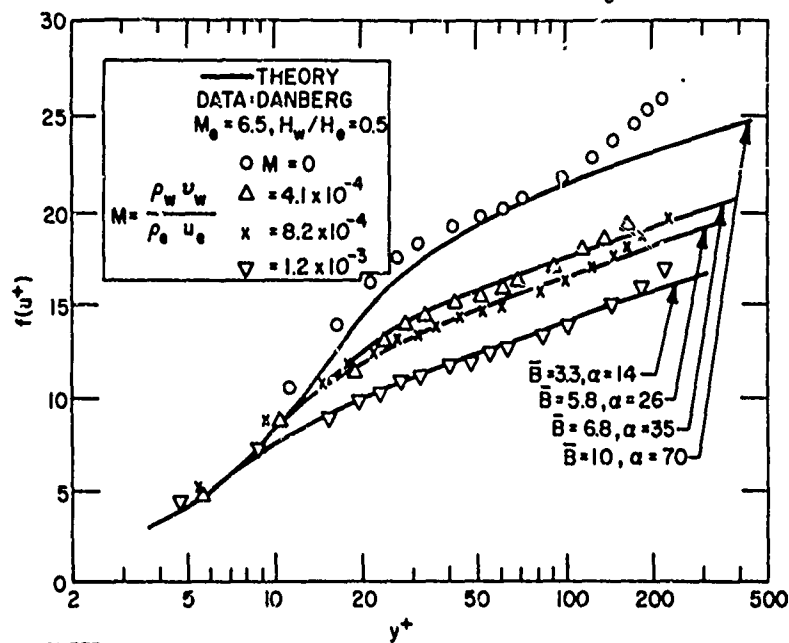
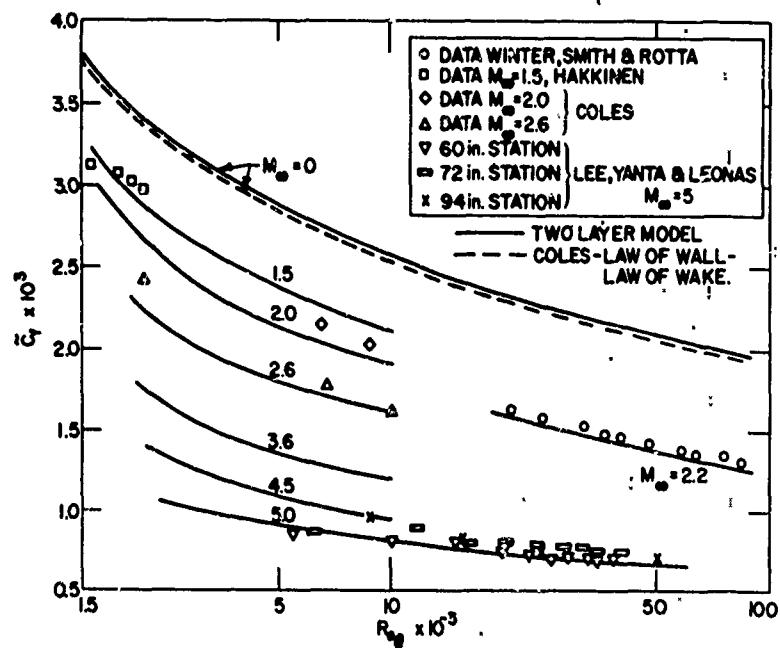


Figure 2 RELAXING FLOW - ABRUPT REMOVAL OF POSITIVE PRESSURE GRADIENT, $M_0 = 0$



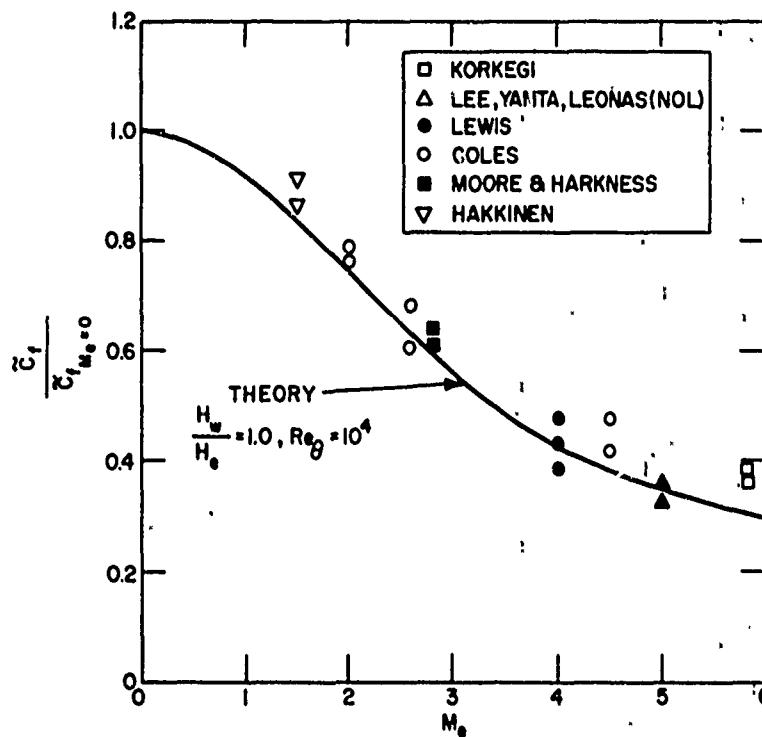
81-773

Figure 3 COMPARISON OF LAW OF THE WALL WITH DATA FOR SURFACE MASS INJECTION



91-774

Figure 4 \tilde{C}_f VERSUS Re_θ FOR EQUILIBRIUM $dp/dx = 0$



91-775

Figure 5 EFFECT OF M_∞ ON \tilde{C}_f

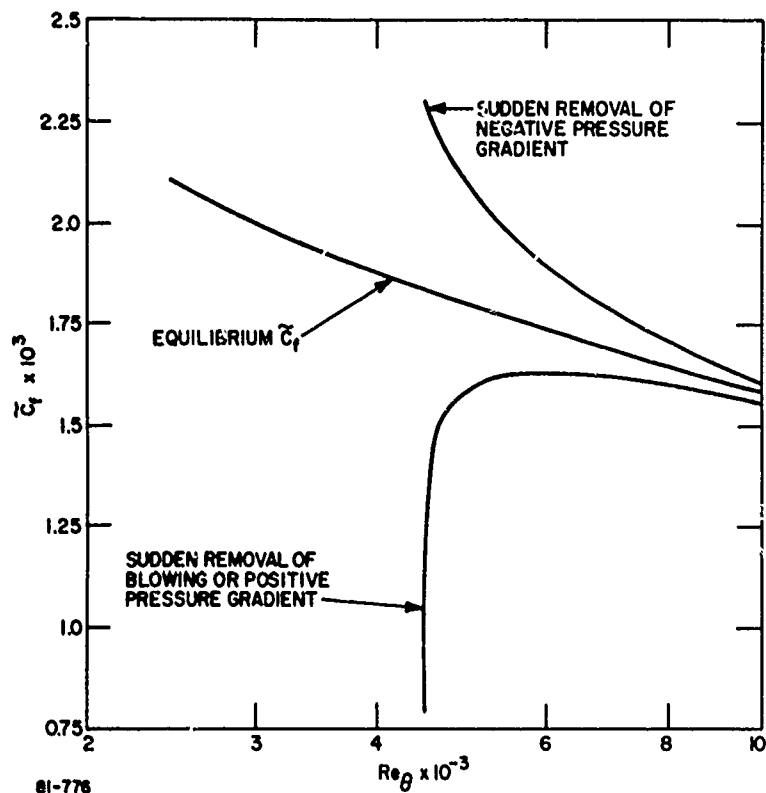
and $Re_\theta = 10^4$, for example, \tilde{C}_f for $H_w/H_e = 0.05$ is only about 15 percent greater than the adiabatic value of \tilde{C}_f . At these same conditions the Reynolds number based on δ^* for a cold wall is about one-third the value for an adiabatic wall.

Figure 6 demonstrates the existence of an equilibrium \tilde{C}_f variation with Re_θ and the approach to this equilibrium variation if the initial \tilde{C}_f is too large or too small. A similar type of relaxation for the heat transfer and total enthalpy profile is shown in Figure 7. For these solutions the initial \tilde{C}_f was set equal to the equilibrium value but the initial value of the Reynolds analogy parameter $2C_H/\tilde{C}_f$ was set at values other than one. This resulted in an initial H versus u profile which was nonlinear in the outer layer. The solutions shown in Figure 7 demonstrate the relaxation of the Reynolds analogy parameter back to one, and relaxation of an initially perturbed H versus u profile back to a linear Crocco integral for the whole layer. (See schematic inserts of profiles in Figure 7.) Relaxing flows of this sort have been measured on wind tunnel walls downstream of the nozzle throat.

Figure 8 shows results for \tilde{C}_f , θ , \bar{U}_m , and the Reynolds analogy parameter for a boundary layer in a region where $dp/dx_1 > 0$ followed by a region where $dp/dx < 0$. The edge Mach number decreases from 2.6 to 1.3 over the first 50 inches and then increases to 2.6 again at $x = 100$ inches. In each case the results are compared with a solution for $M_e = \text{constant} = 2.6$. In the region of positive pressure gradient the wall layer thickness decreases but then increases as $dp/dx < 0$. This behavior is reflected in the variation of \bar{U}_m , which shows that near $x = 100$ inches most of the velocity variation across the boundary layer occurs in the wall layer. Thus, the two-layer model is seen to predict the kind of behavior hypothesized by Coles² in his paper on the law of the wake.

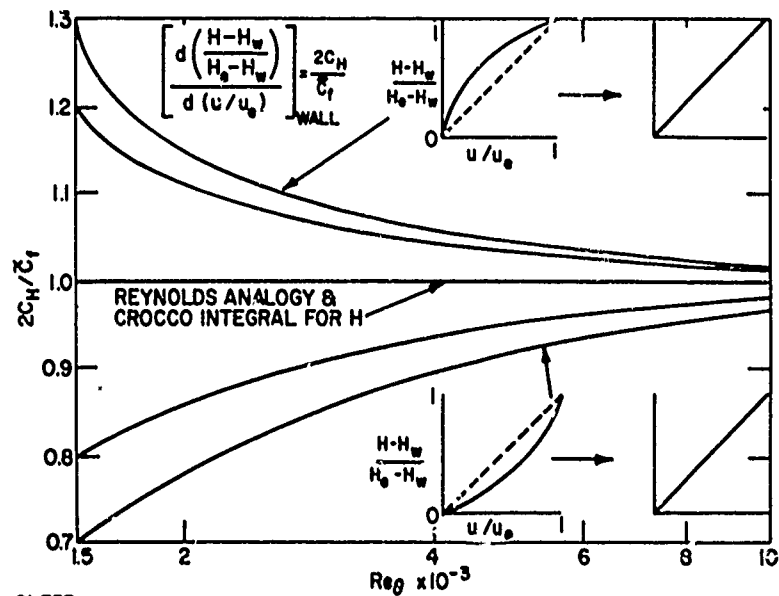
Figures 9 and 10 show comparisons of the theory with data^{18,19} for two-dimensional flows in negative pressure gradients at initial Mach numbers of 1.5 and 3.9, respectively, while Figure 11 shows a comparison with the method of Bradshaw for a flow in zero pressure gradient at Mach 3, followed by a region of strong adverse pressure gradient. Both methods predict that the flow separates, i.e., $\tilde{C}_f \rightarrow 0$. For the two-layer model the solution was stopped when \tilde{C}_f decreased to 2×10^{-5} at $x = 67.8$ cm. In this region $\bar{U}_m \approx 0$ and the layer was composed almost entirely of the outer layer, again demonstrating the kind of behavior predicted by Coles.

Comparison with data obtained by Lewis²⁰ for boundary layers in an initially positive followed by a negative pressure gradient are shown in Figures 12 and 13. In the "strong" pressure gradient case, the Mach number varied from 4 to 2.57 to 4.17 over a distance of about 34 inches. In the "moderate" pressure gradient case the Mach number varied from 4 to 3.2 to 3.8. The experiments were performed with an outer hollow cylinder and an inner axisymmetric pressure generating body. The boundary layer data was taken on the inside surface of the outer cylinder in order to eliminate effects produced by longitudinal curvature. The curves for δ^* and θ are compared with predicted variations for zero pressure gradient in both Figures 12 and 13. The local decrease in δ^* in the region of strong positive pressure gradient (Figure 12) demonstrates the supercritical behavior of turbulent boundary layers at high Mach numbers. Figure 14 shows the predicted skin friction variations for the two cases. Despite the relatively large peak pressure ratio of about 8 in the strong pressure gradient case, the theory predicts that the skin friction coefficient is reduced by only about 50 percent from the local flat plate \tilde{C}_f .



81-776

Figure 6 RELAXING FLOWS AT $M_e = \text{CONSTANT} = 2.6$



81-777

Figure 7 RELAXING FLOW - INITIAL $H \neq A + BU$,
 $M_e = 3.6$, $H_w/H_\theta = 0.5$

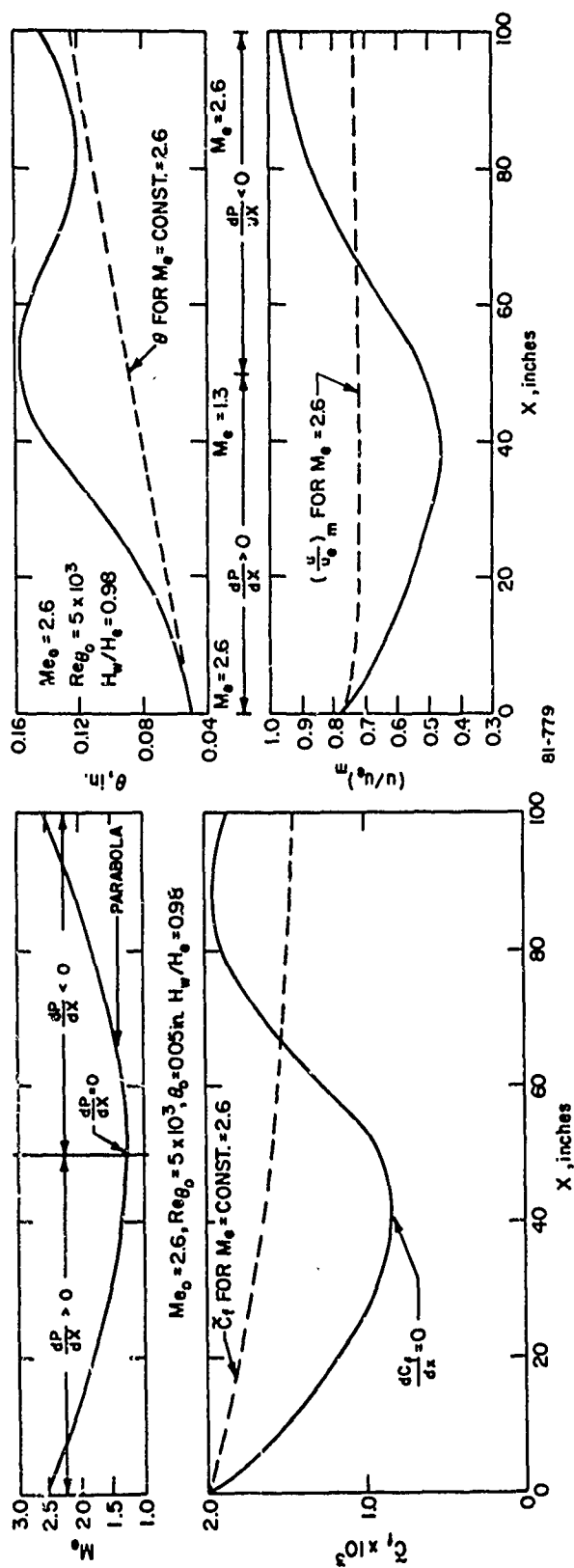


Figure 8a EFFECT OF dP/dx ON \tilde{C}_f

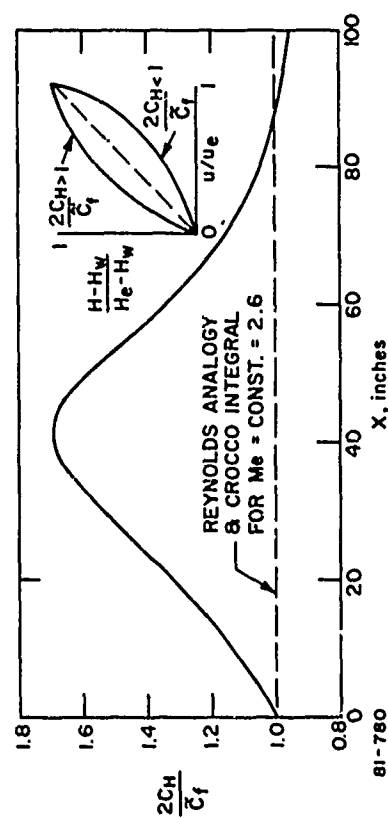


Figure 8b EFFECT OF dP/dx ON θ AND VELOCITY RATIO AT MATCH POINT

Figure 8c EFFECT OF dP/dx ON H VERSUS U PROFILE AND ON REYNOLDS ANALOGY

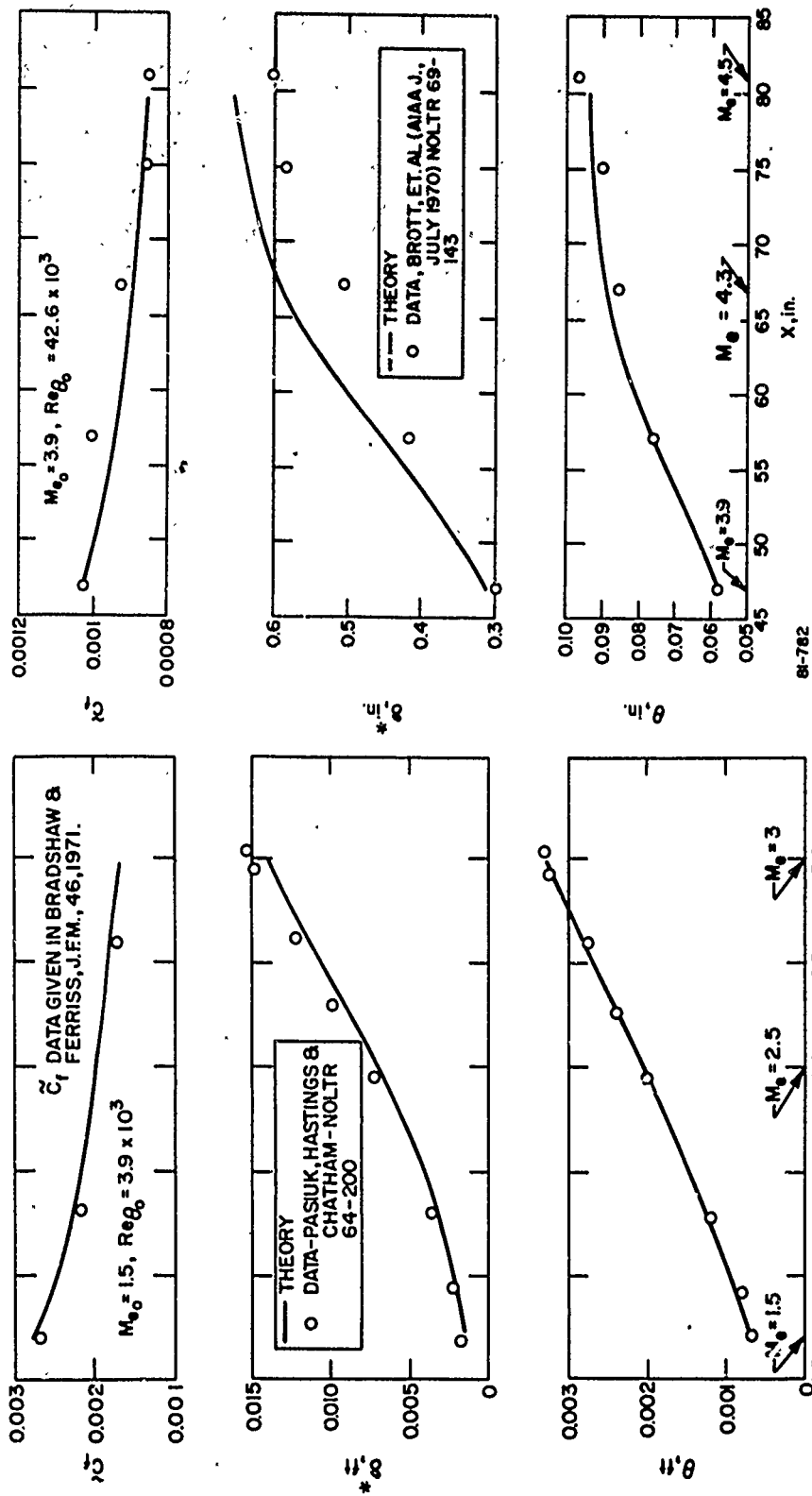


Figure 9 COMPARISON WITH DATA FOR $dP/dx < 0$

Figure 10 COMPARISON V.J. TH DATA, $dP/dx < 0$

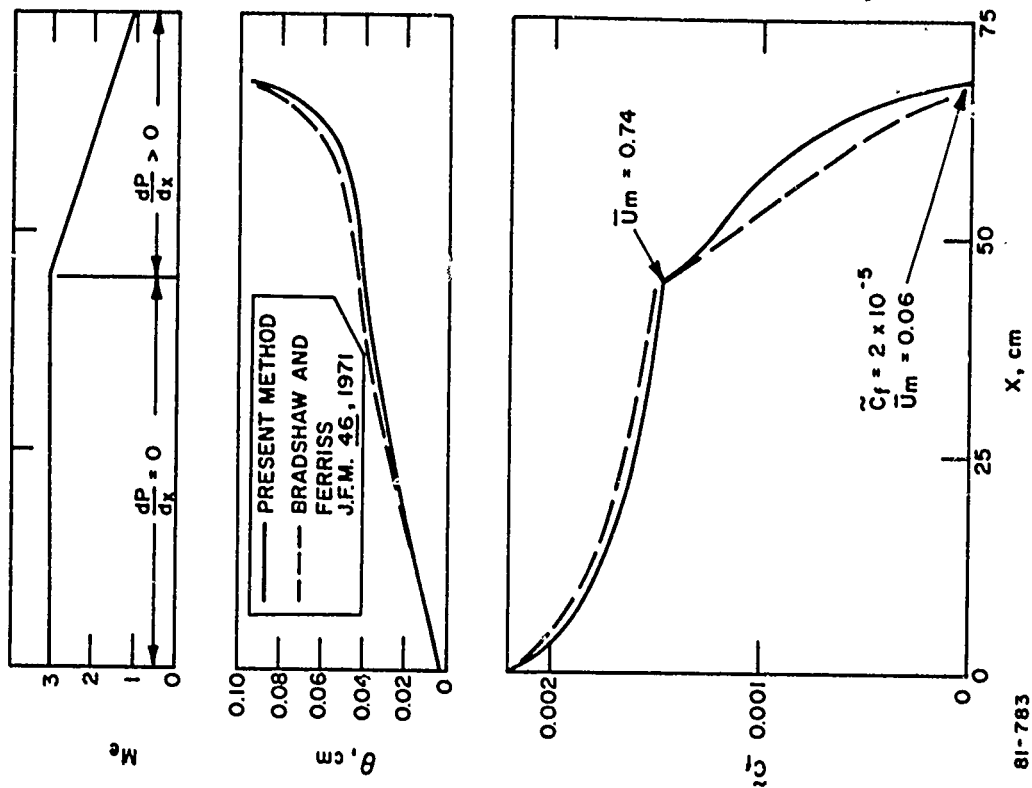


Figure 11 COMPARISON OF TWO-LAYER MODEL WITH
BRADSHAW METHOD, $H_w/H_e = 0.9$, $Re_{\theta_o} = 10^3$

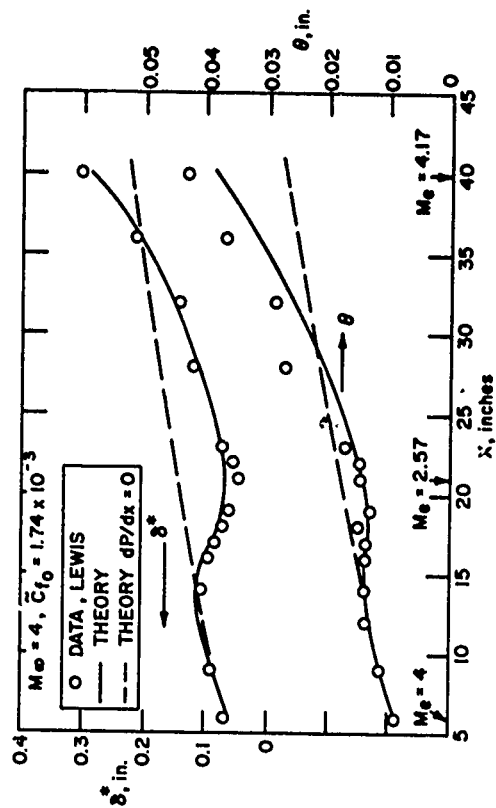


Figure 12 COMPARISON WITH LEWIS, STRONG POSITIVE AND
NEGATIVE PRESSURE GRADIENTS

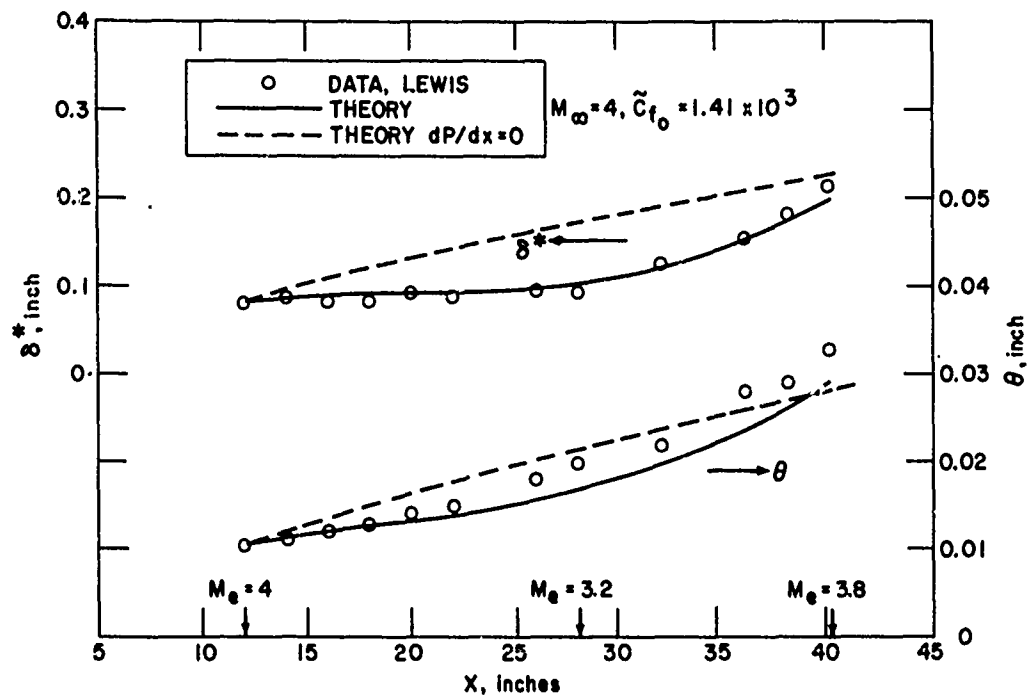


Figure 13 COMPARISON WITH LEWIS, MODERATE PRESSURE GRADIENT

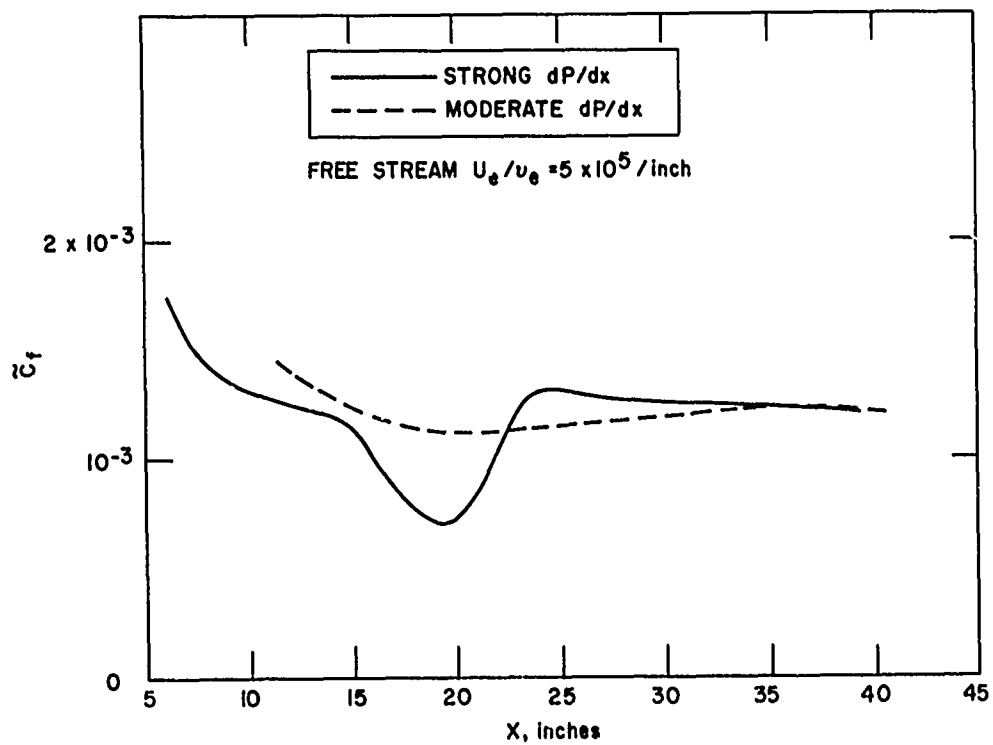


Figure 14 THEORETICAL \tilde{C}_f VARIATIONS FOR EXPERIMENTS PERFORMED BY LEWIS

Figure 15 shows several solutions (various initial values of \tilde{C}_f) for the experiments conducted by McLafferty and Barber,²¹ which were performed on a two-dimensional curved compression ramp. The Mach number decreased from 3 to 1.8 in a distance of 3 inches, and the boundary layer was tripped upstream of the ramp by normal injection. Thus, \tilde{C}_f initially was probably slightly less than the equilibrium value of 1.8×10^{-3} . Figure 15 shows that for an initial $\tilde{C}_f = 1.75 \times 10^{-3}$ the flow remains attached (McLafferty and Barber reported that the flow did not separate) but for an initial $\tilde{C}_f = 1.5 \times 10^{-3}$ the flow separates at $x = 2.73$ inches. In the latter case the strong pressure gradient did not permit relaxation back to the equilibrium \tilde{C}_f so that flow separation on the ramp could have been produced if the injection upstream of the ramp had been stronger.

Comparison of the theory with data taken on an axisymmetric curved compression ramp is shown in Figures 16 and 17. In this case the Mach number decreased from 5.75 to 2.6 and the spreading metric increased by a factor of 1.7. Figure 17 shows that \tilde{C}_f actually increases slightly due to the metric effect (the two-dimensional results show only a 40 percent decrease in \tilde{C}_f at the trailing edge) and the layer does not even come close to separating. Both theory and experiment show a substantial increase in the wall heating (Figure 17).

Comparisons with data on a waisted body of revolution at $M_\infty = 1.4$ and 2.4 are shown in Figures 18 and 19 which indicate large effects produced by the spreading metric, particularly on the momentum thickness variations.

Figure 20 shows some results for relaxing flows produced by taking a given initial turbulent boundary layer profile and letting it relax downstream over conical bodies with different cone angles. These solutions illustrate, for example, the behavior downstream of a sphere-cone junction. The solution for $\beta = 90$ degrees is representative of the flow over the windward side of a sphere-cone at large angle of attack, i.e., the effective cone angle $\beta = \theta_c + \alpha$ is 90 degrees, where θ_c is the cone half angle. The solutions were all obtained for a boundary layer initially in equilibrium for a constant metric (flat plate or cylinder), with $\delta_0/\tau_0 = 0.1$. Thus, the solution for $\beta = 0$ degrees remains in equilibrium for $\tilde{x} > \tilde{x}_0$. The results for $\beta > 0$ degrees all show that the momentum thickness grows more slowly with \tilde{x} than if $\beta = 0$, while the skin friction coefficient increases with increasing β at a given point downstream of \tilde{x}_0 . In fact, for large β (see results for $\beta = 90$ degrees) the momentum thickness actually decreases at the beginning of the relaxation. Far downstream the curves for Re_θ (and also C_f) for $\beta > 0$ degrees all coalesce into a single curve, which is displaced from the $\beta = 0^\circ$ solution by a constant factor in $Re(\tilde{x} - \tilde{x}_0)$. Table I shows results obtained for the various values of β at $Re_\theta = 3 \times 10^4$ from which it is evident that the boundary layers for $\beta > 0^\circ$ are virtually identical to the boundary layer for $\beta = 0^\circ$ if $Re(\tilde{x} - \tilde{x}_0)$ for $\beta > 0^\circ$ is about twice the value of $Re_{\tilde{x} - \tilde{x}_0}$ for $\beta = 0^\circ$. This is a well known result for flow over sharp cones and flat plates in equilibrium.²⁴

Some results computed for a turbulent boundary layer around a sphere-cone nosetip at $\alpha = 0$ and 20° angle of attack (windward side) are shown in Figures 21a, b, c. The solutions were performed by starting 15 degrees from the stagnation point with a transition $Re_\theta = 200$ and several values of \tilde{C}_{f_0} .

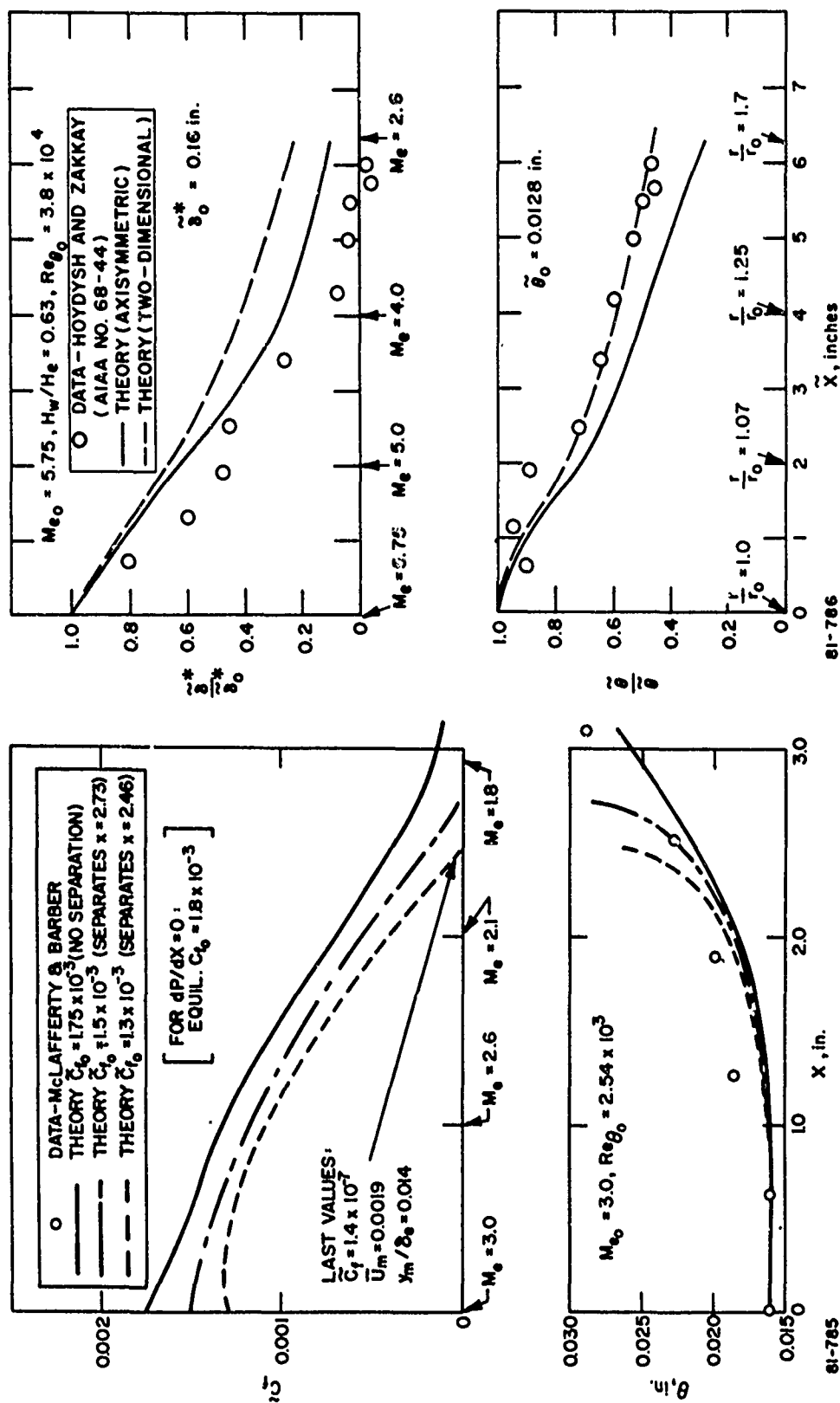


Figure 15 COMPARISON WITH DATA FOR $dP/dx \geq 0$

Figure 16 COMPARISON WITH DATA ON AN AXISYMMETRIC COMPRESSION SURFACE

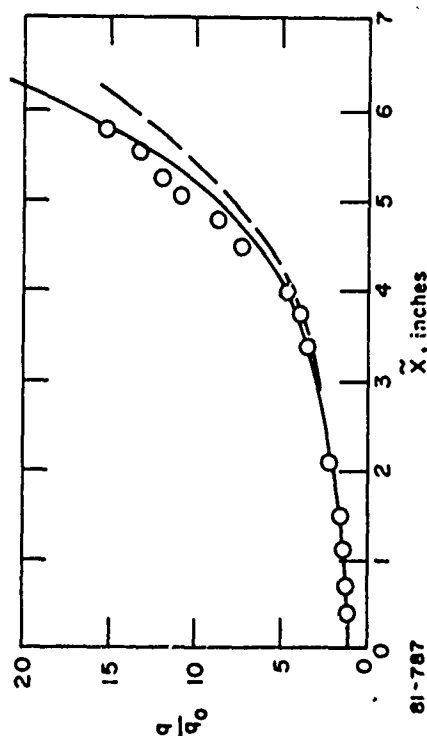
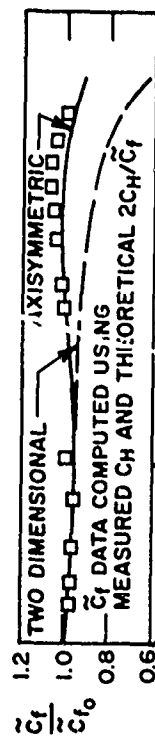
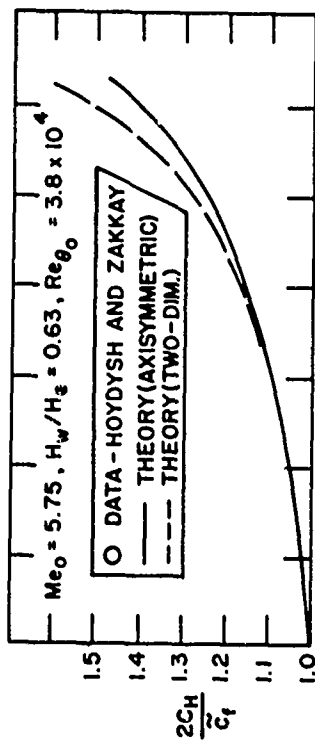


Figure 17 COMPARISON WITH DATA ON AN AXISYMMETRIC COMPRESSION SURFACE

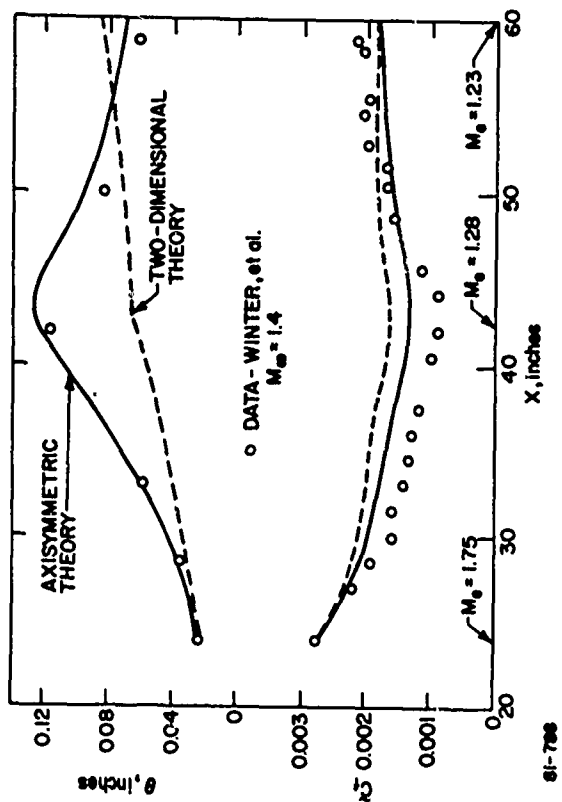


Figure 18 WAISTED BODY OF REVOLUTION

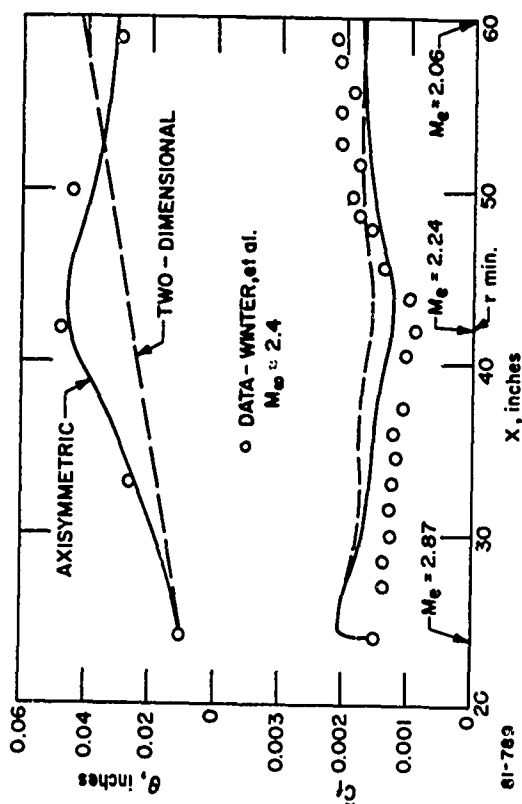


Figure 19 WAISTED BODY OF REVOLUTION

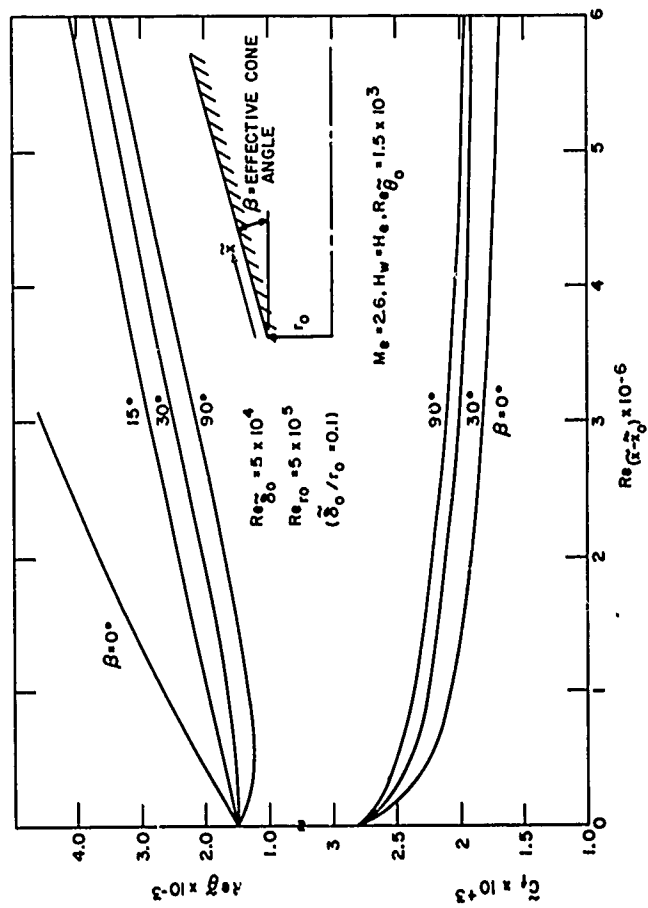


Figure 20 RELAXATION PRODUCED BY CHANGE IN SPREADING METRIC:
EFFECT OF CONE ANGLE FOR A GIVEN INITIAL PROFILE

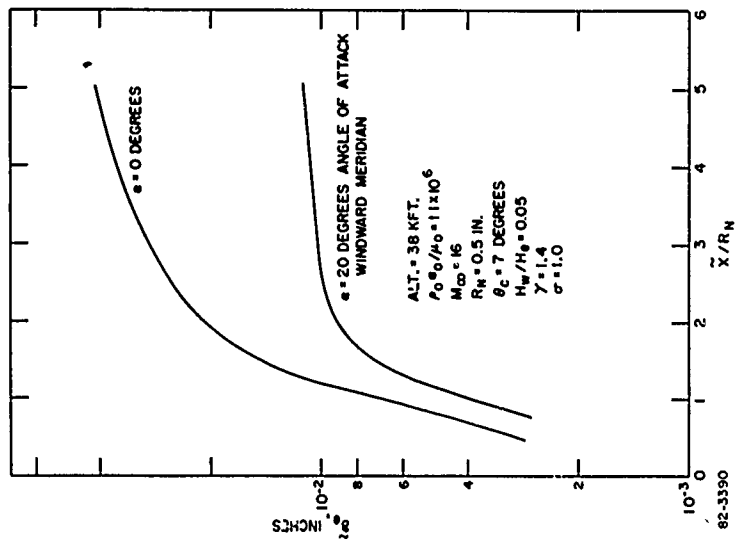


Figure 21a EFFECT OF ANGLE OF ATTACK ON BOUNDARY
LAYER THICKNESS ON NOSE TIP, $M_\infty = 16$

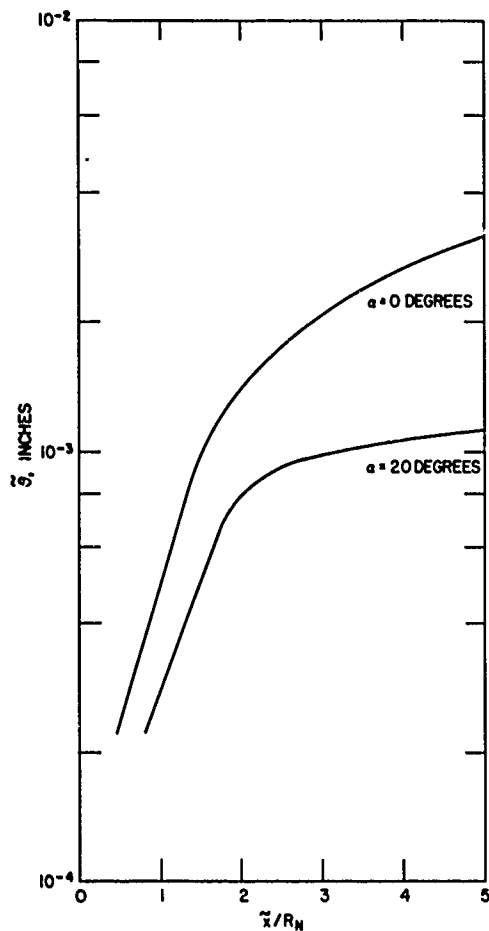


Figure 21b BOUNDARY LAYER MOMENTUM THICKNESS ON NOSE TIP

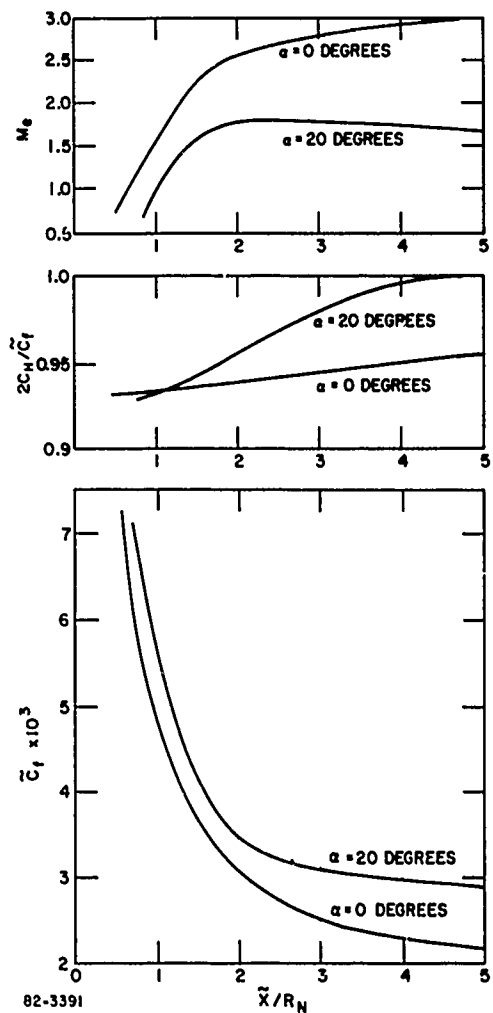


Figure 21c MACH NUMBER, STANTON NUMBER, AND SKIN FRICTION ON NOSE TIP, $M_\infty = 16$

For these conditions the solutions became independent of the starting value of \tilde{C}_f at about 35 degrees from the stagnation point. The solutions demonstrate the relatively slow growth of $\tilde{\theta}$ and $\tilde{\delta}_e$ along the windward side at angle of attack. Along the windward meridian \tilde{C}_f increases by about 35 percent as α increases from 0 to 20 degrees. Also, $2C_H/\tilde{C}_f$ is less than one in both cases which is characteristic of turbulent boundary layers in negative pressure gradients. (See Figures 7 and 8c.)

TABLE I
EFFECT OF CONE ANGLE FOR A GIVEN INITIAL PROFILE
(SOME RESULTS AT EQUILIBRIUM FAR DOWNSTREAM OF INITIAL
STATION. $M_e = 2.6$)

β°	$Re_{(\tilde{x}-\tilde{x}_0)}$	\tilde{C}_f	$Re_{\tilde{\theta}}$	$Re_{\tilde{\delta}_e}$
0	3.81×10^7	1.314×10^{-3}	3.02×10^4	1.22×10^5
15	8.35×10^7	1.323×10^{-3}	3.04×10^4	1.22×10^5
30	8.49×10^7	1.322×10^{-3}	3.06×10^4	1.23×10^5
60	8.41×10^7	1.325×10^{-3}	3.02×10^4	1.22×10^5
90	8.45×10^7	1.324×10^{-3}	3.03×10^4	1.22×10^5

In Equilibrium, Boundary Layer on a Cone is Equivalent to that on a
Plate if Cone $Re_{\tilde{x}} \approx 2.2 \times$ Plate Re_x

Figure 22 shows some results for \tilde{C}_f as a function of $Re_{\tilde{\theta}}$ calculated for relaxing flows at a constant Mach number of 9.37. Several solutions with various starting values of \tilde{C}_f and $2C_H/\tilde{C}_f$ were performed to obtain a qualitative comparison with experiments performed by Laderman and Demetriades²⁵ in the boundary layer on the wall of a wind tunnel. The various initial conditions were used to try and ascertain the effect of the strong negative pressure gradient at the nozzle throat on the downstream properties of the boundary layer. The experimental profile data of Laderman and Demetriades was taken at a station 160 inches downstream of the nozzle throat and shows a nonlinear stagnation enthalpy versus velocity profile characteristic of turbulent boundary layers on wind tunnel walls. This nonlinear profile has been interpreted as evidence that the layer is still in a state of relaxation produced by the strong negative pressure gradient at the nozzle throat.

The theoretical solutions were started at an arbitrary value of $Re_{\tilde{\theta}} = 1.5 \times 10^4$ and were stopped when $Re_{\tilde{\theta}}$ reached the value 3.68×10^4 , which is the value measured by Laderman and Demetriades at the 160-inch station. The solutions show that even over a streamwise distance of about 805 inches (corresponding to the increase of $Re_{\tilde{\theta}}$ from 1.5×10^4 to 3.68×10^4 and a value of $\theta = 0.29$ in. at

$Re_\theta = 3.68 \times 10^4$) the value of \tilde{C}_f at the end of the runs is still dependent upon the initial conditions of \tilde{C}_f and $2C_H/\tilde{C}_f$. Thus, it appears likely that the data of Laderman and Demetriades are for a layer relaxing to equilibrium and that because the throat in their experiments was located at $x \approx 690$ inches (Figure 22), their reported value of $\tilde{C}_f = 0.46 \times 10^{-3}$ is probably larger than the equilibrium flat plate \tilde{C}_f at $Re_\theta = 3.68 \times 10^4$. Because the flow is still relaxing and data was presented at only one streamwise station it is impossible to give a precise comparison between experiment and theory. For example, it is possible to match the experimental values of $\theta = 0.29$ in. and $\delta^* = 2.29$ in. measured at $x = 160$ inches with various pairs of values of \tilde{C}_f and $2C_H/\tilde{C}_f$ at the initial station. One such pair: $\tilde{C}_{f_0} = 0.6 \times 10^{-3}$ and $(2C_H/\tilde{C}_f)_0 = 0.76$ resulted in the values: $\tilde{C}_f = 0.37 \times 10^{-3}$, $\theta = 0.29$ in., $\delta^* = 2.31$ in., $\delta_c = 5.53$ in. at $Re_\theta = 3.68 \times 10^4$, while the values measured by Laderman and Demetriades were $\tilde{C}_f = 0.46 \times 10^{-3}$, $\theta = 0.29$ in., $\delta^* = 2.29$ in., and $\delta_c = 6.01$ inch. At these conditions the theory predicted that wall layer extended out to $y_m = 1.74$ in. where the values of u/u_c and H/H_c were computed to be 0.794 and 0.782, respectively. (The value of $2C_H/\tilde{C}_f$ at $Re_\theta = 3.68 \times 10^4$ was 0.815). The profile data measured by Laderman and Demetriades gave $u/u_c = 0.77$ and $H/H_c = 0.74$ at $y = 1.74$ in. However, a valid comparison would require data to be obtained at two and preferably three streamwise stations so that the relaxation process could be duplicated. As a matter of reference, for the $M_c = 9.37$ results presented in Figure 22, a perturbation of the initial \tilde{C}_f by 20 percent resulted in a perturbation of \tilde{C}_f by 5.5 percent after a streamwise relaxation distance of 160 inches or an $x/\theta_0 = 1.36 \times 10^3$. Consequently, it appears that virtually all data obtained on side-walls of wind tunnels contain upstream relaxation effects in \tilde{C}_f as well as in $2C_H/\tilde{C}_f$ and some of these data may be far out of fluid dynamic equilibrium.

In order to test the present turbulent boundary layer model in a highly nonequilibrium flow situation, a solution was performed for flow over a wavy wall. Experiments by Bertram, et. al.²⁶ for turbulent boundary layers over wavy walls at Mach 6 have demonstrated significant surface pressure and heating variations (by as large a factor as 2) along a wave train. Maximum heating was measured on the forward face of each wave while minimum heating was obtained on the rearward faces. In order to compute the turbulent boundary layer development over waves with wave length of the order of the boundary layer thickness, the solution was obtained as a quasi boundary layer-inviscid flow interaction. The boundary layer at the start of the wave train is in equilibrium ($dp/dx = 0$) for $M_c = 3.6$ and $Re_\theta = 4.5 \times 10^3$. The equilibrium boundary layer profile at these conditions was used as the initial condition for a rotational characteristics calculation of the surface pressure distribution along the waves. The turbulent boundary layer development over the waves was then computed using the surface pressure distribution generated by the characteristics solution. Figure 23 shows the results obtained for a wave train with wave length equal to the initial boundary layer thickness and wave amplitude equal to 0.004 times the wave length. The notation max., min. along the x coordinate refers to the peaks and troughs of the surface waves.

The response of the momentum thickness to the periodic surface pressure variation (or edge Mach number variation shown in Figure 23) is characteristic of supercritical layers, increasing when dp/dx is negative and decreasing when dp/dx is positive, giving a periodic variation of θ with x . The results for δ^*

EXPERIMENT: LADERMAN AND DEMETRADES ON A
WIND TUNNEL NOZZLE WALL.
 $H_w/H_e = 0.385$, $u_0/v_0 = 1.27 \times 10^{-3}/\text{IN.}$
AT $Re_0 = 3.68 \times 10^3$,
 $\theta = 0.29 \text{ IN.}$, $\theta^* = 2.29 \text{ IN.}$, $\tilde{C}_f = 0.46 \times 10^{-3}$
THEORY: $(2C_H/\tilde{C}_f)_0 = 0.76$, $(\tilde{C}_f)_0 = 0.55 \times 10^{-3}$ AND 0.65×10^{-3}
----- $(2C_H/\tilde{C}_f)_0 = 0.70$, $(\tilde{C}_f)_0 = 0.60 \times 10^{-3}$
----- $(2C_H/\tilde{C}_f)_0 = 0.85$, $(\tilde{C}_f)_0 = 0.60 \times 10^{-3}$

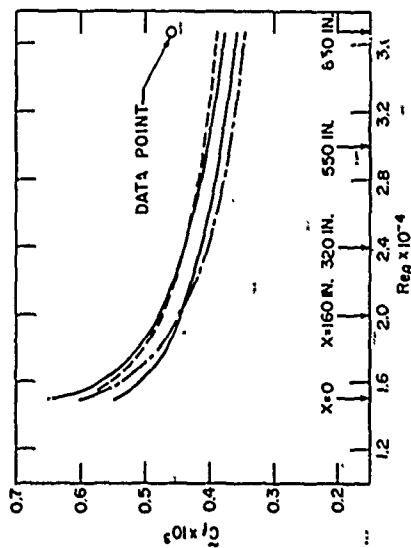


Figure 22-- EFFECT OF INITIAL \tilde{C}_f AND $2 C_H/\tilde{C}_f$ VARIATION
WITH Re_0 WITH $M_e = 9.37$, ZERO PRESSURE
GRADIENT

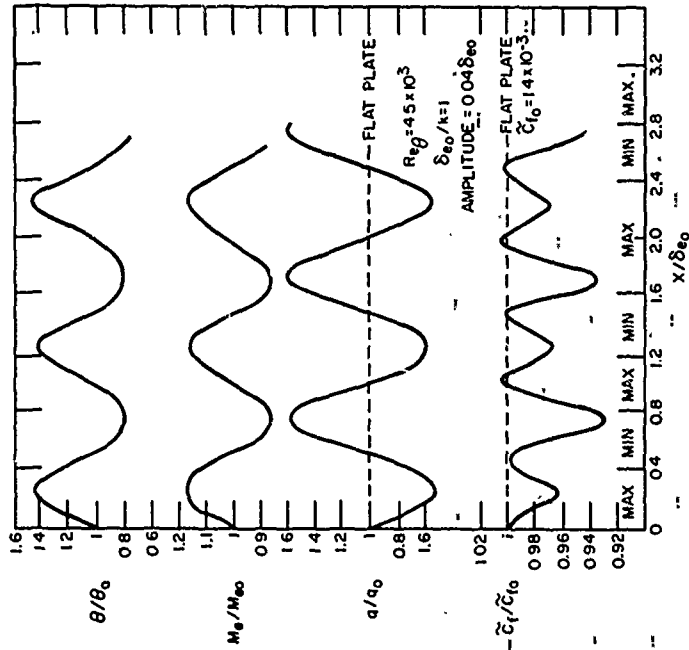


Figure 23- LOCAL FLOW PROPERTIES FOR A TURBULENT
BOUNDARY LAYER OVER A WAVY WALL

and δ_e are also periodic with roughly the same phase as θ . As expected, the heat flux is virtually in phase with the surface pressure with the average being somewhat higher than for a flat plate. However, the average skin friction coefficient is less than the flat plate value and the streamwise variation reveals local minima in \bar{C}_f just upstream of the points of both maximum and minimum in surface pressure. This peculiar variation of \bar{C}_f with x may be a result of the supercritical response of the layer.

The influence of the additive constant \bar{B} in the generalized compressible law of the wall on the turbulent boundary layer over a sharp 20° cone at Mach 5.7 is illustrated in Figure 24. A decrease in \bar{B} , which could be the result of an increase in surface roughness,¹⁰ produces an increase in the integral thicknesses $\bar{\theta}$, $\bar{\delta}^*$, and $\bar{\delta}_e$, and an increase in \bar{C}_f as well. Because the boundary layer solutions shown in Figure 24 are in equilibrium for $x \gtrsim 10$ inches, with $2 C_H \bar{C}_f = 1$, the Stanton number also increases with decreasing \bar{B} . For rough walls

$$\bar{B}_r = \bar{B} - \Delta u_1 / u_r$$

where \bar{B} is the "constant" for smooth walls. For roughness densities of the order 4 to 10,

$$\frac{\Delta u_1}{u_r} = \frac{1}{K} \ln (u_r y_r / \nu_w)$$

where y_r is the roughness height. These expressions were used to relate y_r to \bar{B}_r for the results shown in Figure 24. Evidently, a roughness height of 0.016 inch produces an increase in \bar{C}_f by a factor of about 2.5 above the smooth wall value.

Calculations showing the effect of a sudden expansion on turbulent boundary layer heating are compared with some measurements in Figures 25, 26, and 27. The experiments were conducted at a free stream Mach number of 5 in a hypersonic wind tunnel at the U.S. Naval Ordnance Laboratory. The measurements were performed on a sharp 50-8 degree biconic model and are reported in Reference 27. The results presented in Figures 25 through 27 are for three values of the free stream unit Reynolds number. As indicated by the heat flux levels reported in Reference 27, the boundary layer was fully turbulent over at least half of the 50 degree cone for all three Reynolds numbers.

At the 50 and 8 degree cone junction both experiment and theory show a sudden decrease in heating, however, the data shows that for a certain distance after the expansion the heating falls well below theoretical predictions. At the two highest values of Reynolds number (Figures 25 and 26) the heating drops to about 30 percent of the theoretical prediction at the end of the expansion but after a certain distance downstream (about 65 times the boundary layer thickness before the expansion for the case shown in Figure 26) it increases to about the level predicted. At the lowest Reynolds number (Figure 27) the heating

* A continuous turbulent boundary layer solution over the sudden expansion was obtained by assuming that the complete expansion from $\theta_c = 50^\circ$ ($M_c = 1.15$) to $\theta_c = 8^\circ$ ($M_c = 2.73$) takes place over a streamwise distance of 0.16 in. or about 5 local boundary layer thicknesses ($\delta_c = 0.032$ in. ahead of the expansion).

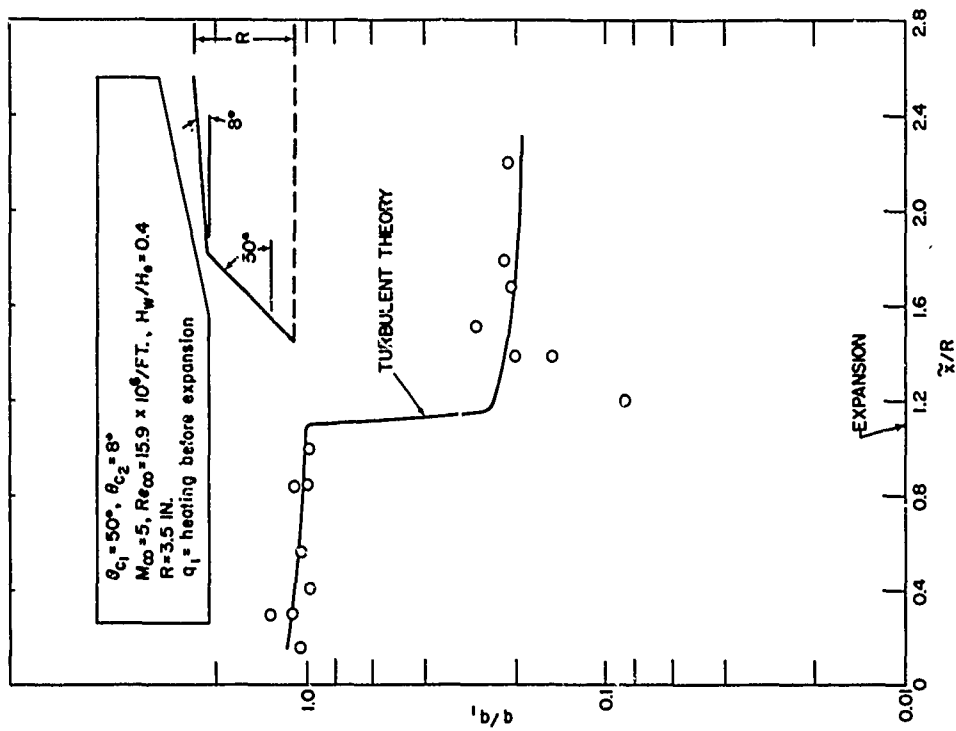


Figure 25 RELAMINARIZING FLOW: HEAT TRANSFER DISTRIBUTION ON A SHARP BICONIC

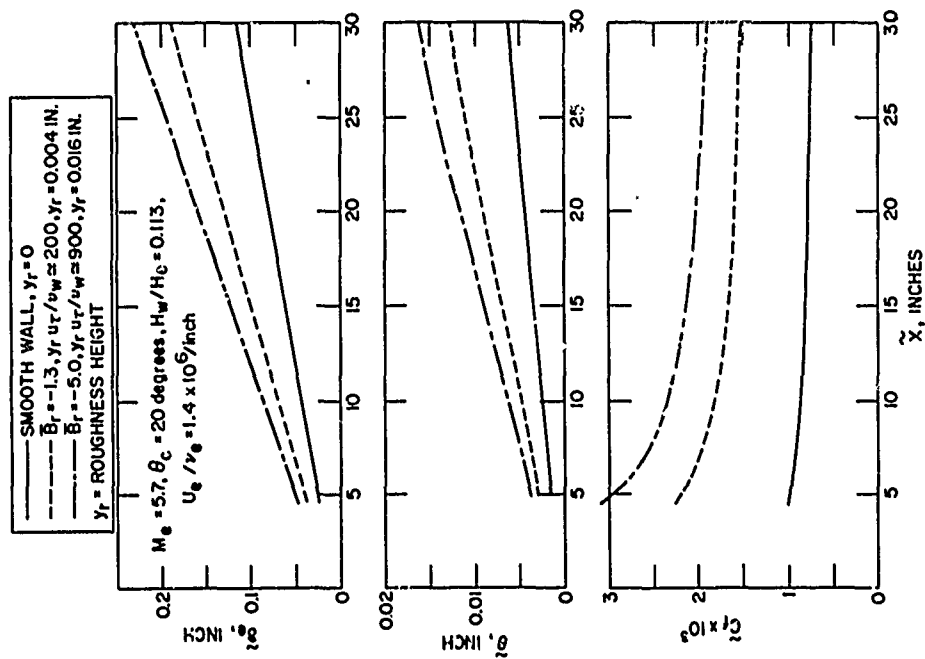


Figure 24 EFFECT OF SURFACE ROUGHNESS ON TURBULENT BOUNDARY LAYER ON SHARP CONE

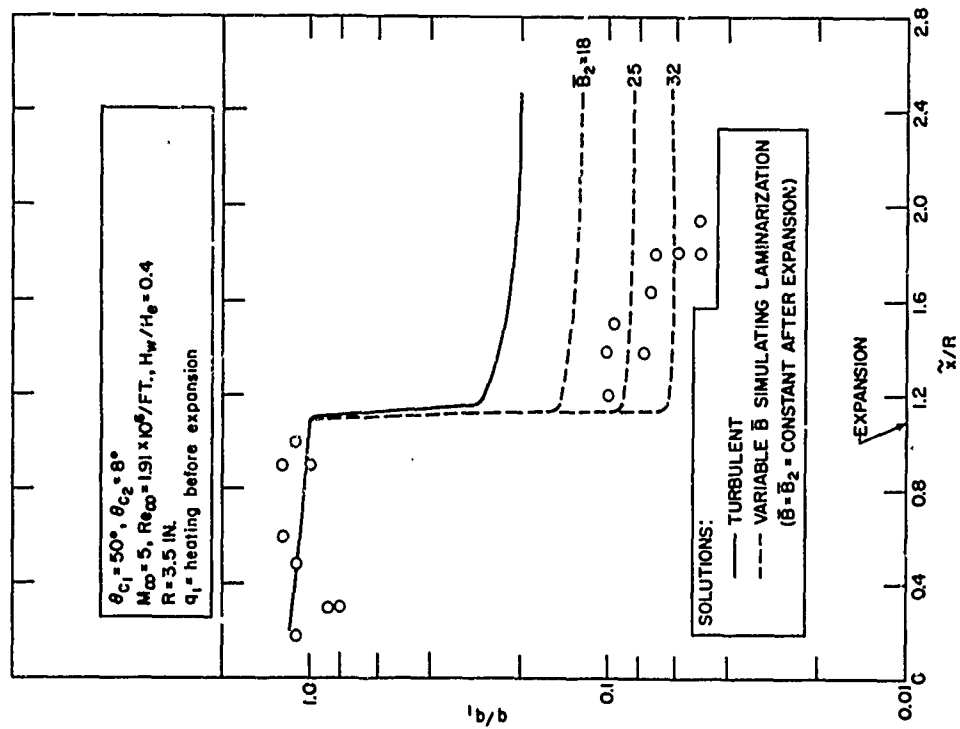


Figure 26 RELAMINARIZING FLOW: HEAT TRANSFER DISTRIBUTION ON A SHARP BICONIC

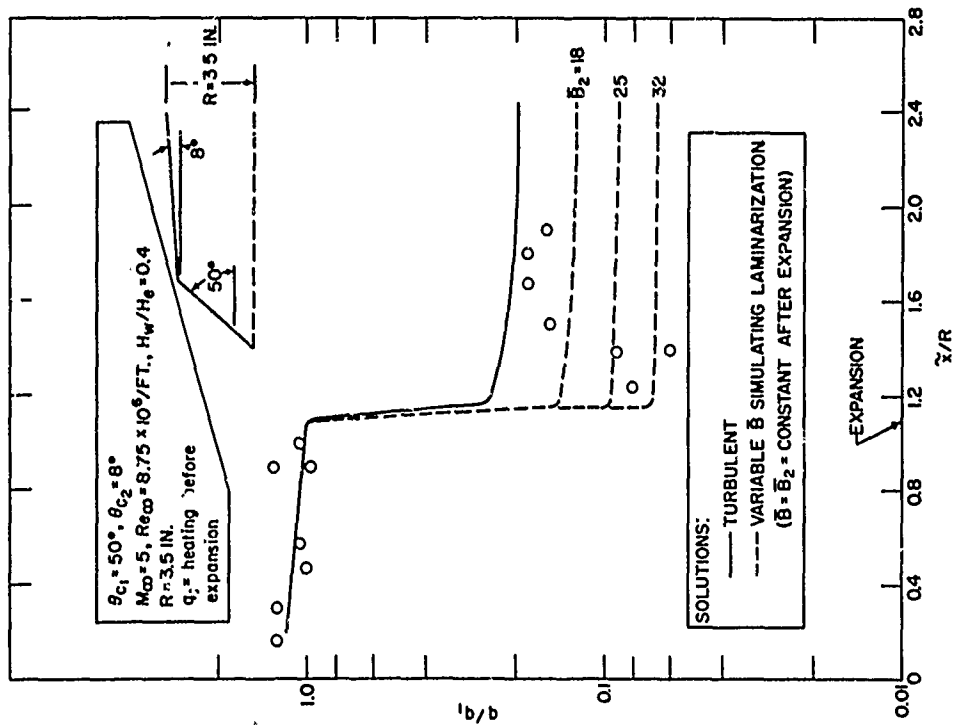


Figure 27 RELAMINARIZING FLOW: HEAT TRANSFER DISTRIBUTION ON A SHARP BICONIC

drops suddenly at the expansion, as in the other two cases, but then continues to decrease at a fairly rapid rate along the 8 degree cone. At the last data point ($\tilde{x}/R = 1.93$) the heating is only about 25 percent of that predicted by the theory. Apparently, the decrease in heating across the expansion is controlled by the pressure gradient for these cases because q/q_1 at the start of the 8 degree cone is approximately the same for all three Reynolds numbers.

The behavior of the heating data in these experiments suggests that the turbulent boundary layer on the 50 degree cone partially or even completely relaminarized in the sudden expansion at the junction of the 50 and 8 degree cones. The abrupt increase in q at some distance downstream of the expansion at the two highest Reynolds numbers suggests a retransition of the laminarized layer. Evidently, at the lowest Reynolds number retransition occurred downstream of the last heating gage so that the flow remained laminarized for at least 90 boundary layer thicknesses (based on the layer thickness just upstream of the expansion).

Several experiments^{28,29} on turbulent boundary layer laminarization in incompressible flows have demonstrated that during a strong expansion the sudden reduction of turbulence production in the wall layer produces a departure of the velocity profiles from the law of the wall. When \tilde{u}^+ is plotted against \tilde{y}^+ the profiles shift progressively upward away from the law of the wall as the flow proceeds through a sufficiently strong expansion. Launder and Jones²⁸ have suggested that this upward shift in the velocity profile and the simultaneous increase in the laminar sublayer thickness can be characterized by an increase in the parameter α in the relation for the variation of mixing length through the sublayer and transition layer, Eq. (55). As shown in Figure 3, an increase in α produces an increase in the additive "constant" \bar{B} in the law of the wall so that one of the observed features of laminarization can be simulated by permitting \bar{B} to increase with \tilde{x} through an expansion. Figures 26 and 27 show results obtained by letting \bar{B} increase linearly with \tilde{x} through the expansion ($\Delta\tilde{x} = 0.162$ in.) from the initial value of 6.1 (for $H_w/H_e = 0.4$) to selected values ($\bar{B}_2 = 18, 25$ and 32) at the end of the expansion. Along the 8 degree cone following the expansion, $\bar{B} = \bar{B}_2 = \text{constant}$. These results demonstrate that a decrease in heating below the turbulent prediction is consistent with an increasing \bar{B} (or increasing α) in the expansion. By modeling the variation of α rather than \bar{B} through strong expansions, and by including the contribution of the laminar sublayer in the relations for mass, momentum and energy flux in the wall layer, it should be possible to reproduce even more closely some of the features of laminarization and retransition displayed by the data in Figures 25 through 27.

7.2 Results for Uniform and Discontinuous Distributions of Surface Mass Injection

The predicted variation of \tilde{C}_f with Re_θ for various blowing rates in incompressible flow is shown in Figure 28. The results show that at a given Re_θ , \tilde{C}_f decreases steadily to zero as M increases. Values of \tilde{C}_f as low as 10-15 have been computed for $M = 0.05$ and $Re_\theta \approx 10^5$ so that with the two-layer model there is no evidence of an Emmons type singularity for massive blowing.

Although the experimental data for \tilde{C}_f with surface mass injection is highly scattered, Squire⁸ has attempted a best fit of data obtained by McQuaid³⁰, Jeromin³¹ and Squire⁸ at $M_e = 0, 2.5$ and 3.5 , which is compared with the theory

in Figure 29. Following Squire and others, the $\tilde{C}_f/\tilde{C}_{f_0}$ ratio is plotted versus the usual injection parameter¹ $2M/\tilde{C}_{f_0}$. Both the experiments and theory indicate that the decrease in \tilde{C}_f at a given value of the blowing parameter is less severe as the Mach increases.

One possible reason for the large scatter in \tilde{C}_f data with blowing is shown in Figure 30, where we have compared predictions with the data of Danberg⁹ at Mach 6.7. When plotted in the standard way, i.e., $\tilde{C}_f/\tilde{C}_{f_0}$ versus $2M/\tilde{C}_{f_0}$, the theory reveals a significant variation with the local Re_θ , which apparently has not been accounted for in past presentations of data. The theory also predicts a variation in the $\tilde{C}_f/\tilde{C}_{f_0}$ ratio with wall to free-stream stagnation enthalpy ratio, as shown in Figure 30.

The effect of surface mass injection on the form parameter $\bar{H} = \delta^*/\bar{\theta}$, where δ^* and $\bar{\theta}$ are the displacement and momentum thicknesses in transformed, Howarth coordinates is shown in Figure 31. The data extends over a Mach number range of 0 to 6.2, and was compiled by Fernandez and Zukoski³². Results of the two-layer model were obtained for $M_e = 0$ and are seen to agree quite well with the data up to the largest value of M (0.013) for which there are measurements at $M_e = 0$. For $M > 0.015$ the theoretical curve diverges rapidly from the data, which, for these large blowing rates was all obtained for $M_e = 2.5$. Thus, it is not clear whether the divergence of the curve from the data signals the failure of the two-layer model for large blowing rates or a breakdown in the Howarth transformation in collapsing all compressible profiles to a constant density form.

An increase in the physical δ^*/θ ratio with increasing blowing is predicted at all Mach numbers. For example, Figure 32 shows a comparison of results at Mach 6.7 with data obtained by Danberg⁹, while Figures 33 and 34 show comparisons with the streamwise variations of θ and δ^* measured by Jeromin³¹ at Mach 2.5 and 3.5, respectively.

Figure 35 gives a comparison of predicted momentum thickness variations with the measurements of Martellucci³³ for uniform injection through a 7.25-degree half-angle cone at $M_\infty = 8$. All solutions were started at $\tilde{x} = 8.4$ inches, which was the station at which injection began on the model. This station also corresponded approximately to the point where boundary layer transition began in the experiments, having evidently been tripped by the injection, while the end of transition was located at about $\tilde{x} = 16.5$ inches. Two solutions were performed for $M = 0$, starting with $\tilde{\theta}_0 = 0.003$ and 0.004 inch, to test whether the downstream $\tilde{\theta}$ variations would be strongly influenced by the initial conditions for \tilde{C}_f , $\tilde{\theta}$ and δ_e , which were not measured at $\tilde{x} = 8.4$ inches and, therefore, had to be assumed. The two solutions for $M = 0$ are seen to converge rapidly to a more or less unique $\tilde{\theta}$ variation with \tilde{x} , indicating that the solutions have relaxed to equilibrium for $\tilde{x} > 25$ inches. It is assumed that the solutions for $M \neq 0$ have also achieved equilibrium and are virtually independent of the starting conditions for $\tilde{x} > 25$ inches.

Figure 35 shows that for $M = 0$ and the two lowest injection rates the theory predicts values of $\tilde{\theta}$ well below the data, while for the two highest injection rates the results are in good agreement. Since the measurements were all obtained

¹ Examination of the equations for the two-layer model (Appendix 1) shows that the proper injection parameter is $2M/\tilde{C}_f$.

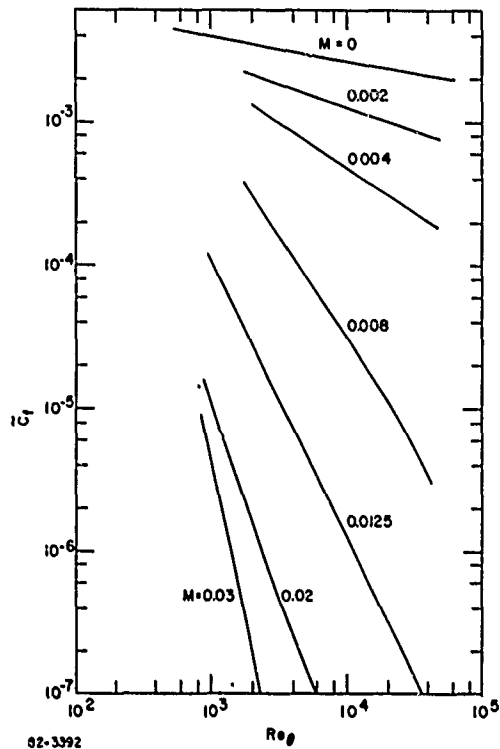


Figure 28 EFFECT OF BLOWING ON \tilde{C}_f FOR INCOMPRESSIBLE FLOW

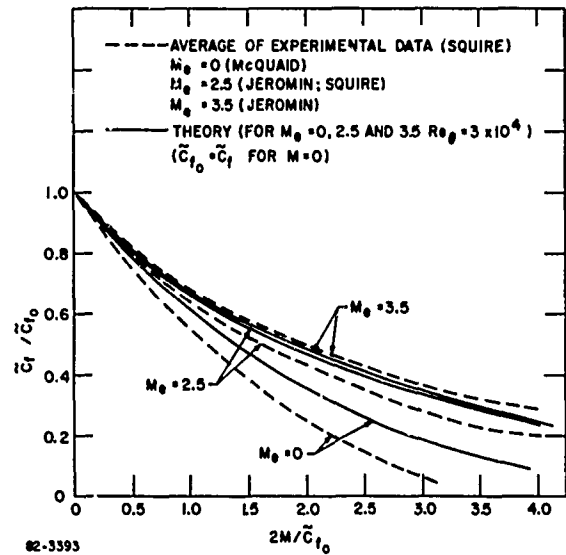


Figure 29 VARIATION OF \tilde{C}_f WITH BLOWING

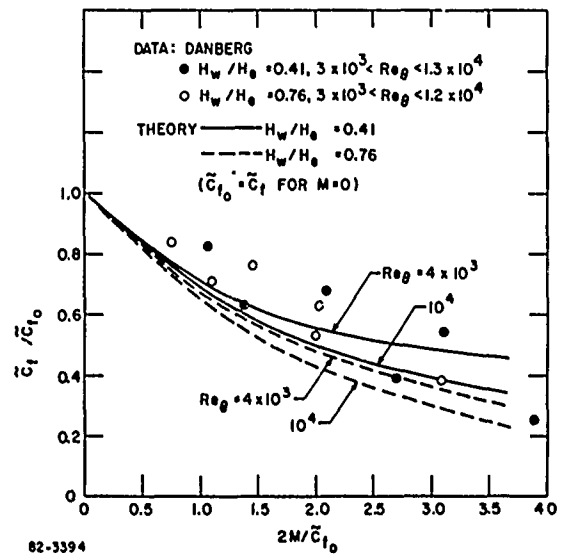


Figure 30 VARIATION OF \tilde{C}_f WITH BLOWING AT MACH 6.7

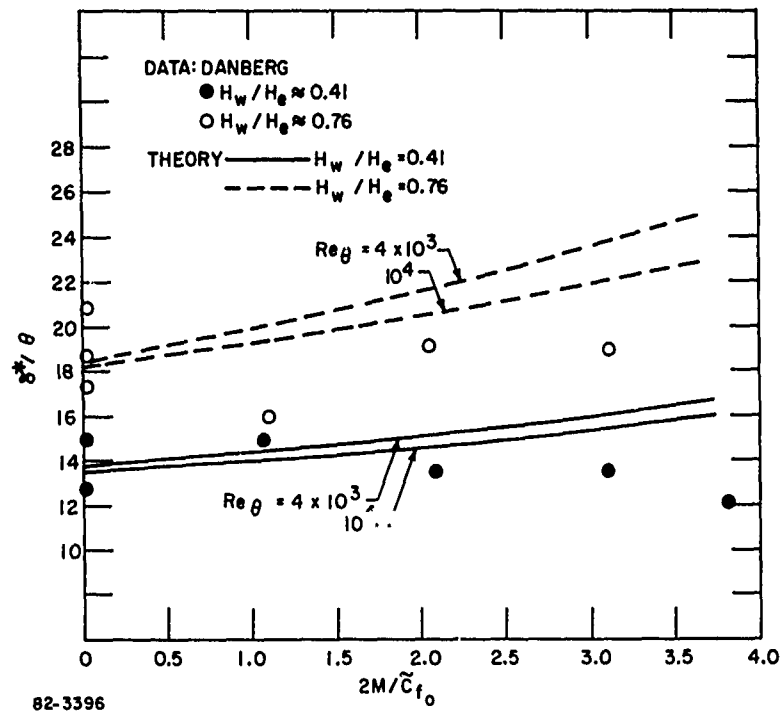


Figure 31 FORM PARAMETER COMPARISON, $dp/dx = 0$

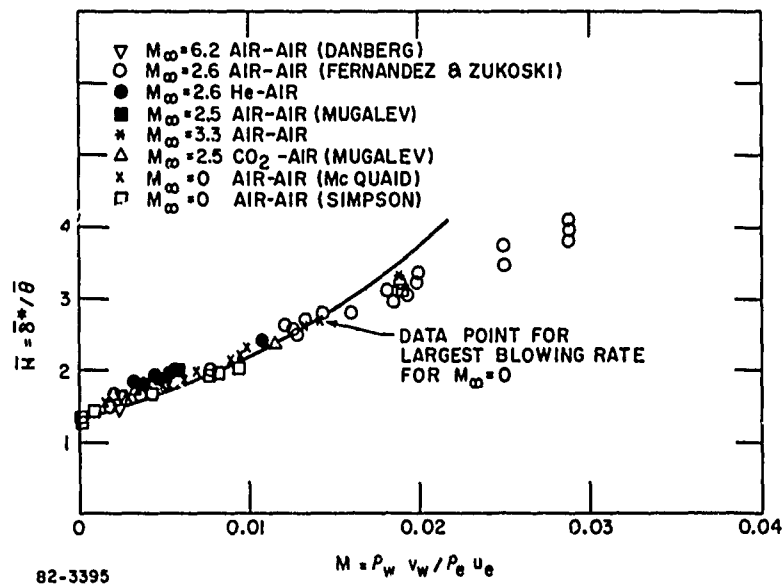


Figure 32 VARIATION OF δ^*/θ WITH BLOWING AT MACH 6.7

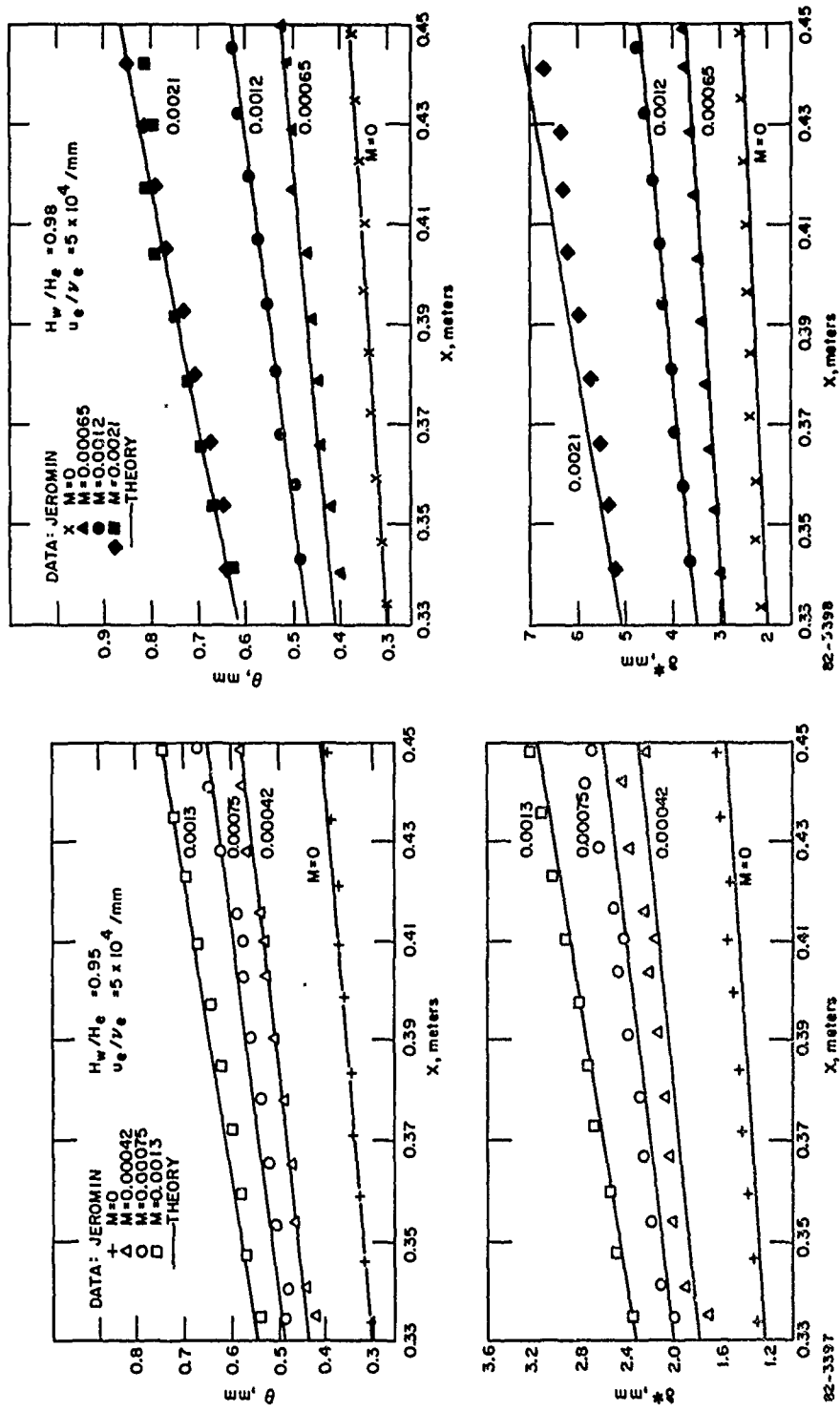


Figure 33 VARIATIONS OF θ AND δ^* AT $M_e = 2.5$

Figure 34 VARIATIONS OF θ AND δ^* AT $M_e = 3.5$

with the porous sintered steel model, the wide disagreement between the experiments and theory for $M = 0$ is apparently caused by surface roughness (see, for example, Figure 24). But as M increases, producing larger boundary layer thicknesses compared to the roughness height, the influence of surface roughness evidently disappears. These results demonstrate that the combined effects of mass injection and surface roughness can be important and will require further study to produce reliable boundary layer predictions, especially for very cold walls where effects of surface roughness are magnified and where there is little or no data on the effect of H_w/H_c and M on the additive constant \bar{B} in the law of the wall. It is also quite likely that roughness effects are responsible for most of the scatter in \bar{C}_f and C_H data with surface mass injection.

Solutions for discontinuous blowing distributions in incompressible flows are compared with some measurements by McQuaid³⁰ and Simpson³⁴ in Figures 36 and 37. For the step decrease in blowing data on McQuaid, the solution was performed by constructing a continuous ramp function for M , which decreased from 3.4×10^{-3} to zero over a streamwise distance equal to the local momentum thickness. The initial abrupt increase in \bar{C}_f shows that at the first station the theoretical solution is out of equilibrium, with \bar{C}_f being below the theoretical equilibrium value. \bar{C}_f then reaches the equilibrium value and then decreases with x to the point where the injection stops.

A continuous ramp function was used to increase M from zero to 0.002 over a streamwise distance equal to the local θ in the solution given in Figure 37. The solid curves show the behavior of the solution for $M = 0.002$ downstream of $x \approx 37.5$ inches, while the dashed curves show the behavior if the blowing had remained equal to zero.

Velocity profiles with surface mass injection (see Section 6.0) are compared with incompressible data of McQuaid³⁰ in Figure 38 and with data obtained by Jeromin³¹ at $M_e = 3.5$ in Figure 39. In both cases α , which is determined by matching \bar{B} computed from Eq. (59) with the empirical relations for \bar{B} given in Section 3.0, decreases steadily with increasing M (see Figure 1). At some sufficiently large value of M , depending on H_w/H_c and M_e , $\alpha \rightarrow 0$, which implies that the laminar sublayer vanishes. For incompressible flow α vanishes at $M \approx 0.01$ so that in order to maintain $\alpha = 0$ for $M \approx 0.01$ \bar{B} would have to increase with increasing M . This conjectured behavior of \bar{B} for large blowing is just

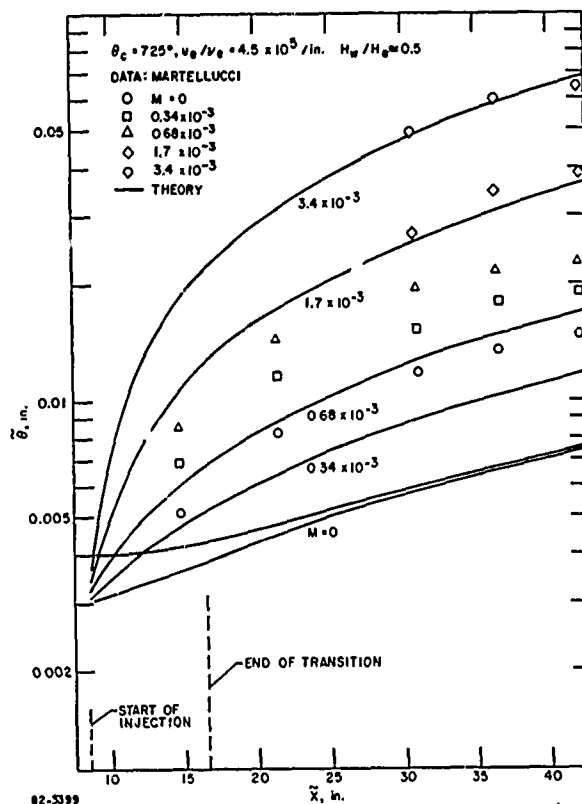


Figure 35 MOMENTUM THICKNESS DISTRIBUTIONS ON A SHARP CONE AT MACH 8

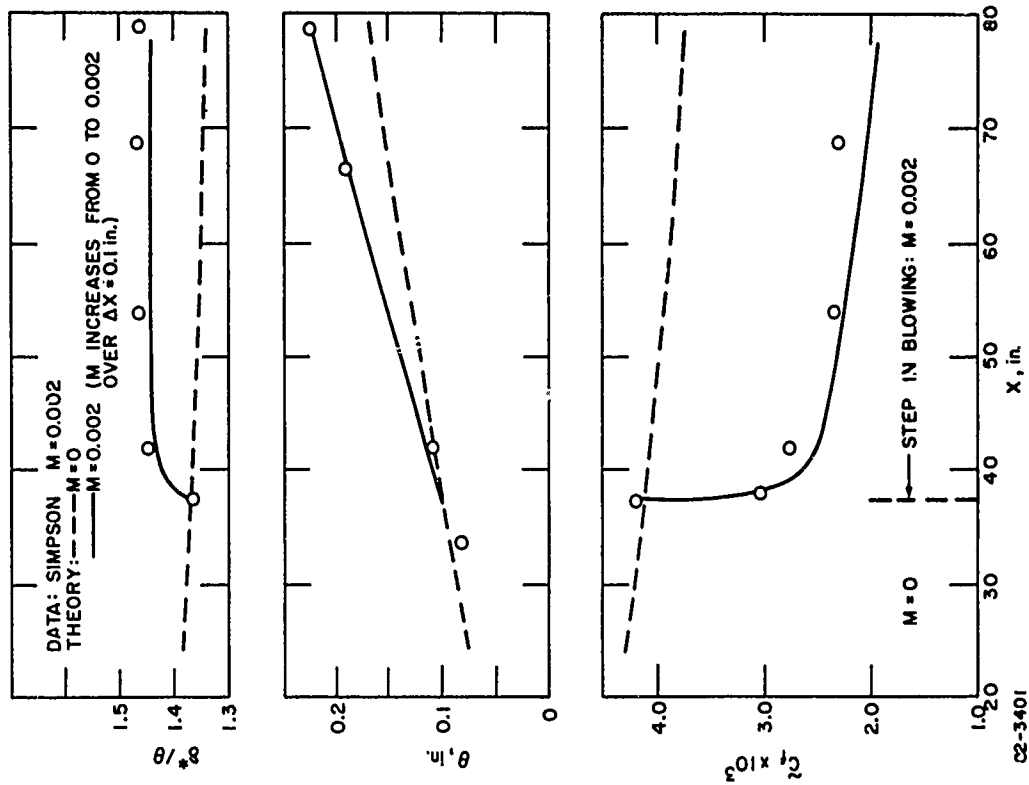


Figure 37 DISCONTINUOUS INCREASE IN BLOWING, INCOMPRESSIBLE FLOW

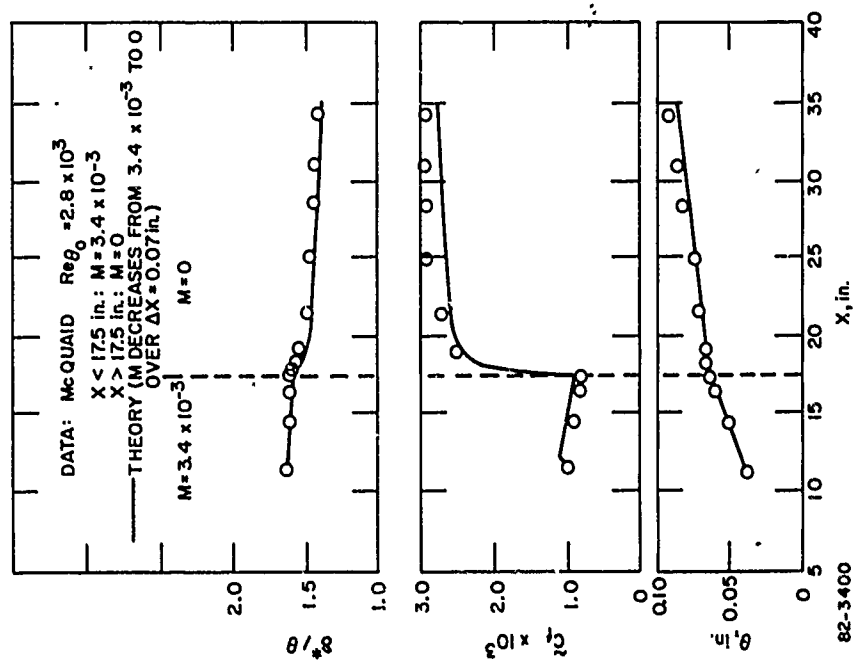


Figure 5 DISCONTINUOUS DECREASE IN BLOWING, INCOMPRESSIBLE FLOW

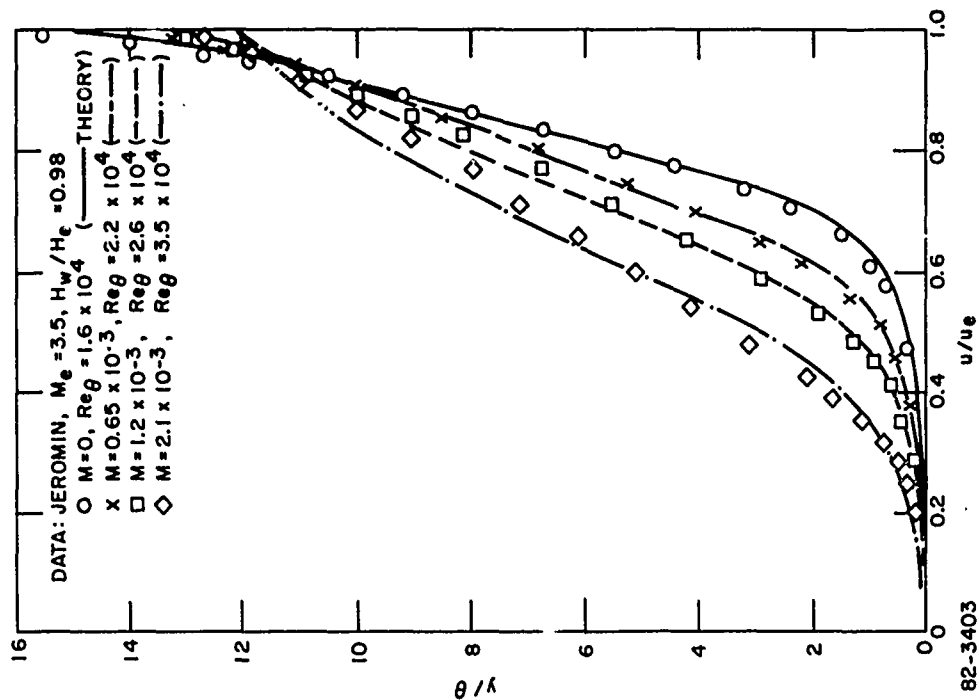


Figure 38 VELOCITY PROFILES WITH INJECTION, $M_e = 0$

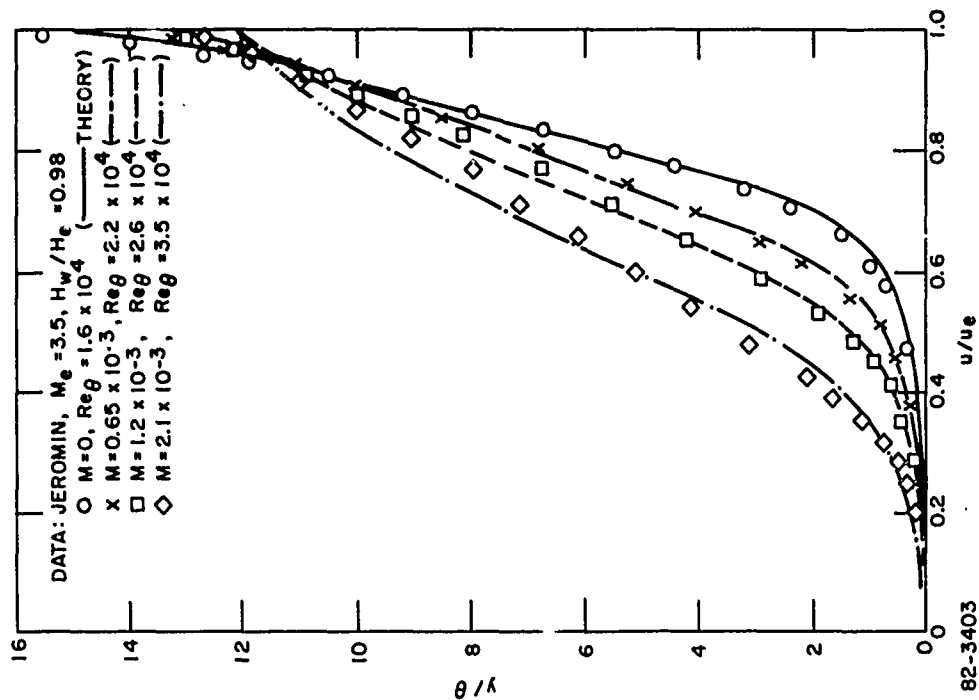


Figure 39 VELOCITY PROFILES WITH INJECTION, $M_e = 3.5$

opposite to the variation of \bar{B} with M which was established from the data of Squire and Danberg for small blowing at supersonic speeds.

As M increases above 0.01, the velocity profiles obtained using the law of the wall in the inner layer, rather than Eqs. (57) and (58), become highly inflected, with most of velocity increase taking place in the outer part of the boundary layer. This behavior was also found in the analyses of turbulent boundary layers with massive blowing in References 35 and 36 and in the experiments reported in Reference 32.

7.2.1 Ablation and Transpiration Cooling: Solutions for Flows with the Mass Injection Distribution Determined by an Energy Balance at the Surface

A crucial feature of flows with ablation or transpiration cooling is the interaction mechanism between the rate at which gas is sublimated or evaporated into the boundary layer and the heat flux which reaches the solid or liquid surface. In this situation the mass injection rate is determined by a local energy balance at the surface and the blowing parameter M becomes an additional dependent variable in the system of simultaneous differential equations.

If H_i is the effective heat of ablation or evaporation, which includes the heat capacity, i.e., $H_i = H_v + C_p \Delta T$, where H_v is heat of sublimation or evaporation, then

$$q_w = \rho_w \tilde{v}_w H_i \quad (65)$$

For negligible gas radiation and negligible conduction in the liquid or solid, q_w is the convective heat flux. Combining Eqs. (37) and (65) gives

$$M = H_e/H_i (1 - H_w/H_e) C_H \quad (66)$$

From Eqs. (25) and (37)

$$C_H = \frac{H_w/H_e}{(1 - H_w/H_e)} B C_f \quad (67)$$

Substituting Eq. (67) into (66) and differentiating with respect to the streamwise distance x gives (assuming H_i is independent of x)

$$\frac{dM}{dx} = \frac{H_w}{H_i} \left[C_f \frac{dB}{dx} + B \frac{dC_f}{dx} \right] \quad (68)$$

By using Eq. (66) as an additional initial condition, and by adding Eq. (68) to the system of simultaneous differential equations, the coupled "feedback" problem of the effect of blowing on the heat flux can be computed as part of the downstream integration scheme. The use of Eq. (68) obviates having to perform lengthy iterations for the proper matched boundary conditions on M and C_H at each point along the surface so that the computing time is about the same as if M is a specified function of \tilde{x} .

Figure 40 shows some results computed with the coupled energy balance at the surface for a 0.25-inch radius spherical nose at hypersonic flow conditions. The stagnation pressure behind the normal shock is 40 atm, the free-stream stagnation enthalpy is 2,600 Btu/lb and the wall temperature is 1000° R, resulting in $H_w/H_e = 0.092$. At these conditions, $\gamma = 1.23$ and $\sigma \approx 0.5$ for equilibrium air. The Mach number distribution around the sphere was computed assuming isentropic flow and a static pressure distribution given by

$$p/p_{t_2} = 0.77 \cos^2 \theta + 0.23$$

The solutions were all started at 10 degrees from the stagnation point using more or less arbitrary initial conditions for $\bar{\theta}$, $\bar{\delta}_e$, \bar{C}_f , C_H . Solutions obtained using different sets of initial conditions gave results for \bar{C}_f and C_H that were virtually independent of the initial conditions for angles greater than 25 degrees from the stagnation point. Figure 40 shows the effect of the parameter H_e/H_i on distributions of the blowing parameter M and the nondimensional heat flux. As the parameter H_e/H_i increases the rate at which material is ablated or evaporated into the boundary layer increases, resulting in a net decrease in the heat flux which reaches the gas-solid or gas-liquid interface.

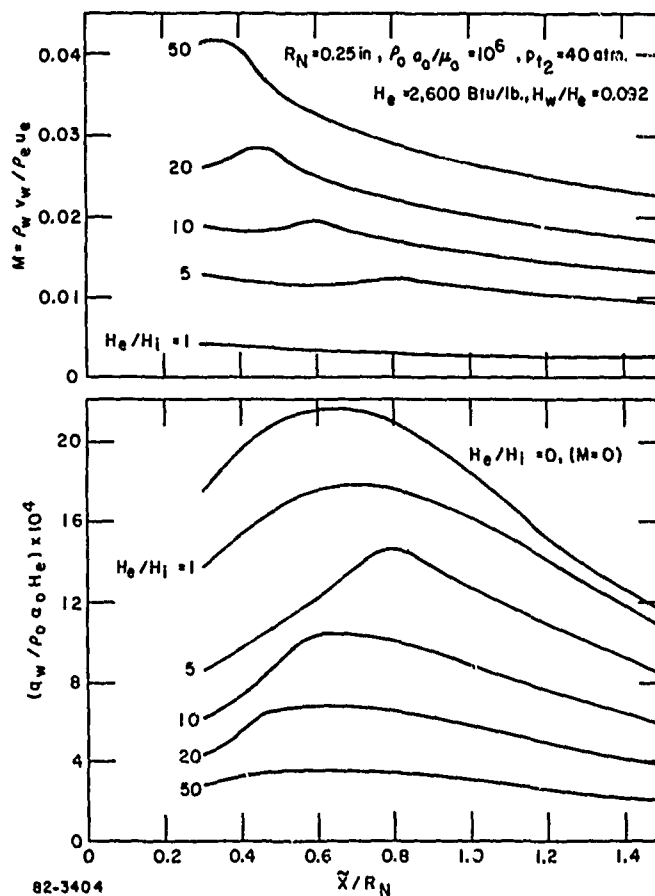


Figure 40 BLOWING AND HEATING DISTRIBUTIONS AROUND A SPHERICAL NOSE WITH COUPLED ENERGY BALANCE AT THE SURFACE

8.0 CONCLUDING REMARKS

All results reported in this report have been obtained by evaluating the turbulent production integral over the outer layer using a cubic variation of ϵ between y_m and δ_e ($\omega = 3$ in Eq. (46)). Stable solutions, in the sense that the power-law exponent n in the outer layer velocity profile remains bounded, have been obtained for negative and positive pressure gradients, with cold and adiabatic walls, up to Mach 10. It is really quite remarkable that the evaluation of the production integral with a simple cubic variation of ϵ produces stable solutions for such a wide range of flow conditions. For incompressible flow in zero pressure gradient, for example, a constant value of the production integral α_0 equal to 0.18 gives a downstream solution of the type $n \rightarrow \infty$, while a value $\alpha_0 = 0.09$ gives a solution in which $n \rightarrow 0$. Moreover, these instabilities occur after a streamwise distance of only about 10 boundary layer thicknesses. Despite this rather sensitive dependence of the streamwise variation of n on the magnitude of α_0 , the values of \tilde{C}_f along the integral curves differ by less than one percent for $\alpha_0 = 0.18$ and $\alpha_0 = 0.09$. Clearly, then, the stability of the interaction between the inner and outer layers is much more sensitive to the level of turbulence production in the outer layer than is the streamwise development of the layer as a whole. In other words, as long as a way of calculating α_0 can be found which keeps the inner-outer layer interaction stable (n finite), the results for $\tilde{C}_f(\bar{x})$, $\tilde{\theta}(\bar{x})$, etc. should be within a few percent of the results of all other stable solutions obtained with slightly different methods of calculating α_0 . This is true whether α_0 is computed using eddy viscosity or other, more sophisticated, stress models.

Solutions for boundary layers in strong expansions have exhibited instabilities of the type $n \rightarrow \infty$ for $\omega = 3$ so that the cubic variation of ϵ/ϵ_m obviously cannot be considered "universal." Because for this type of instability ($n \rightarrow \infty$), α_0 , and hence ω , must be decreased to produce stable solutions, a quadratic or even linear variation of ϵ/ϵ_m across the outer layer may be required. An example of the unstable behavior in a strong negative pressure gradient is shown in Figure 41. The calculations were performed for a flow in which the inviscid Mach number increases linearly from 1.5 to 4.5 over a streamwise distance equal to 660 times the initial boundary layer thickness. Solutions were performed for $\omega = 1, 2$ and 3, starting with an initial boundary layer in equilibrium for zero pressure gradient at $Re_\theta = 10^4$. As indicated in the figure, n grows to 10^3 for $\omega = 3$ and 2 at $x/\delta_{e_0} = 390$ and 430, respectively. Both solutions are unstable with n increasing exponentially at these values of x . The solution for $\omega = 1$ is stable throughout the expansion, with $n = 27.6$ at the end of the run. Despite the wide difference in the stability characteristics of the solutions, Figure 41 shows that the maximum difference in \tilde{C}_f along the integral curves for the three values of ω is only about 4 percent. A stable solution is found by lowering the value of ω (decreasing α_0) from 3 to 1 but the effect of this operation on the boundary layer solution is practically negligible. Consequently, it appears that the two-layer model can provide quantitative results for the streamwise variation of the turbulence production in the outer layer simply on the basis of the stability of the inner-outer layer interaction. Solutions obtained using finite difference methods^{11,12} and prescribed lateral variations of mixing length or eddy viscosity have also shown that the overall boundary layer development is rather insensitive to assumed levels of intermittency at the outer edge.

However, these methods are incapable of providing much insight into the inner-outer layer interaction, at least as they are presently formulated.

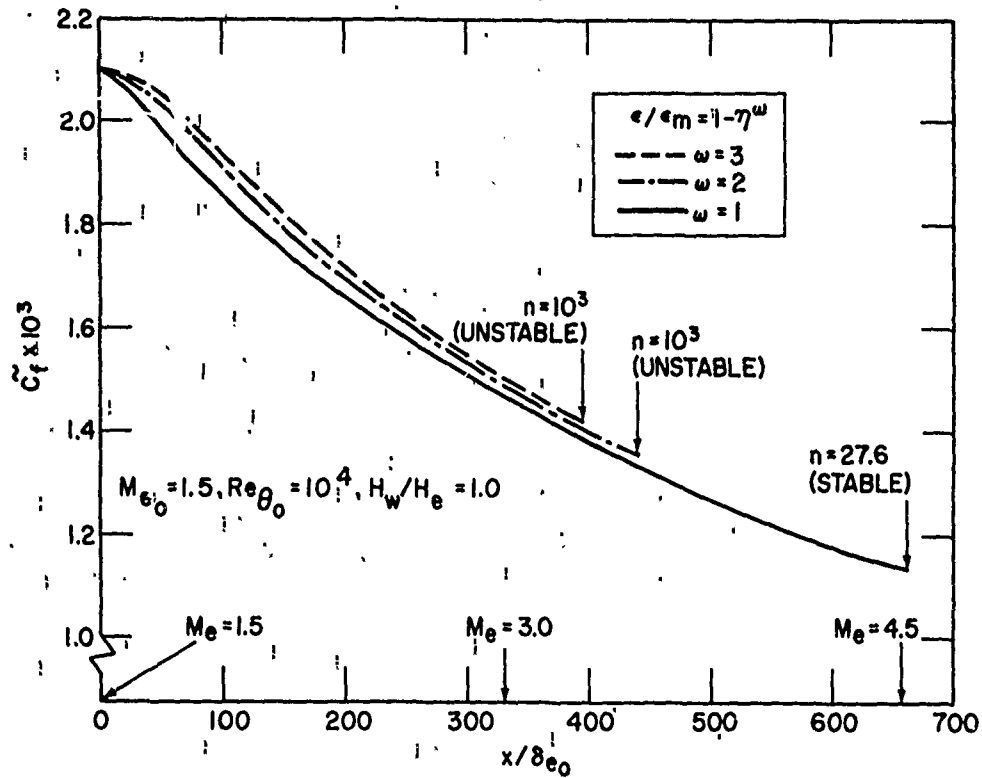


Figure 41 SKIN FRICTION VARIATIONS IN A NEGATIVE PRESSURE GRADIENT WITH $\omega = 1, 2$, AND 3 IN TURBULENT PRODUCTION INTEGRAL, α_0

9.0 REFERENCES

1. Hunter, L. G., and B. L. Reeves, "Results of a Strong Interaction, Wake-Like Model of Supersonic Separated and Reattaching Turbulent Flows," AIAA J., 9, 703-712 (1971).
2. Coles, D., "The Law of the Wake in the Turbulent Boundary Layer," J.F.M., 1, 191-226 (1956).
3. Maise, G., and H. McDonald, "Mixing Length and Kinematic Eddy Viscosity in a Compressible Boundary Layer," AIAA J. 6, 73-80 (1968).
4. Fannelop, T. K., and G. D. Waldman, "Displacement Interaction and Flow Separation on Cones at Incidence to a Hypersonic Stream," paper presented at AGARD conference on "Hypersonic Boundary Layers and Flow Fields," at Royal Aeronautical Society, London (May 1968).
5. Lewis, J. E., T. Kubota, and W. Webb, "Transformation Theory for the Compressible Turbulent Boundary Layer with Arbitrary Pressure Gradient," SAMSO-TR-68-439 (September 1968).
6. Nee, V., and L. Kovaszny, "Simple Phenomenological Theory of Turbulent Shear Flows," Physics of Fluids, 12, 473-484 (1969).
7. Bradshaw, P., and D. Ferriss, "Calculation of Boundary Layer Development Using the Turbulent Energy Equation," J.F.M., 46, 83-110 (1971).
8. Squire, L. C., "A Law of the Wall for Compressible Turbulent Boundary Layers with Air Injection," J.F.M. 37, 449-456 (1969).
9. Danberg, J. E., "Characteristics of the Turbulent Boundary Layer with Heat and Mass Transfer at $M = 6.7$ ", Naval Ordnance Laboratory, Report NOLTR 64-99 (October 1964).
10. Van Driest, E. R., "On Turbulent Flow Near a Wall," JAS 23, 1007-1011 (1956).
11. Smith, A. M. O. and T. Cebeci, "Numerical Solution of the Turbulent Boundary Layer Equations," McDonnell Douglas Report No. DAC 33735 (May 1967).
12. Herring, H. J., and G. L. Mellor, "A Method of Calculating Compressible Turbulent Boundary Layers", NASA CR-1144 (September 1968).
13. Clauser, F., "The Turbulent Boundary Layer", Adv. in Applied Mech. 4, Academic Press, 1-51 (1956).
14. Bradshaw, P., and D. Ferriss, "The Response of a Retarded Equilibrium Turbulent Boundary Layer to the Sudden Removal of Pressure Gradient", NPL Report 1145 (1965).

15. Forsythe, G., and C. Moler, Computer Solution of Linear Algebraic Systems, Prentice Hall (1967).
16. Fitzgerald, K. E., "Error Estimates for the Solution of Linear Algebraic Systems", Journal of Research N.B.S., Math. Sci., 74B (1970).
17. Kline, S., M. Morkovin, G. Sovran, and D. Cockrell, AFOSR-IFP-Stanford Conference on Turbulent Boundary Layers, Stanford University Press (1968).
18. Pasiuk, L., S. Hastings and R. Chatham, "Experimental Reynolds Analogy Factor for a Compressible Turbulent Boundary Layer with a Pressure Gradient", NOL Report NOLTR 64-200 (1965).
19. Brott, D., W. Yanta, R. Voisinet, and R. Lee, "Experiment of the Compressible Turbulent Boundary Layer with a Favorable Pressure Gradient", NOL Report 69-143 (1969).
20. Lewis, J., private communication, 1970, TRW Systems Division, Redondo Beach, California.
21. McLafferty, G., and R. Barber, "Effect of Adverse Pressure Gradients on Turbulent Boundary Layers in Supersonic Streams", J.A.S., 29, 1-10 (1962).
22. Hoydysh, W., and V. Zakkay, "An Experimental Investigation of Hypersonic Turbulent Boundary Layers in Adverse Pressure Gradient", AIAA Preprint No. 68-44 (1968).
23. Winter, K., K. Smith, and J. Rotta, "Turbulent Boundary Layer Studies on a Waisted Body of Revolution in Subsonic and Supersonic Flow", AGARDOGRAPH 97 (1965).
24. Moore, F. K., "Three-Dimensional Boundary Layer Theory," Advances in Applied Mechanics, Vol. IV, pp. 159-228, (1956).
25. Laderman, A., and A. Demetriades, "Mean Flow Measurements in a Hypersonic Turbulent Boundary Layer," Philco-Ford Corporation Pub. No. U-4950, (August 1971).
26. Bertram, M., L. Weinstein, A. Cary, and J. Arrington, "Heat Transfer to Wavy Wall in Hypersonic Flow," AIAA J. 5, 1760-1767 (1967).
27. Otis, J. H., et al., "Nosetip Ablation Phenomena," Strategic Reentry Technology Program Final Report, Vol. II, Avco Government Products Group, Avco Systems Division, AVSD-0210-70-RR, (SAMS0-TR-70-247) (1970).
28. Launder, B., and W. Jones, "Sink Flow Turbulent Boundary Layers," J.F.M., 38, 817-831 (1969).
29. Badri Narayanan, M., and V. Ramjee, "On the Criteria for Reverse Transition in a Two-Dimensional Boundary Layer Flow," J.F.M., 35, 225-241 (1969).

30. McQuaid, J., "Incompressible Turbulent Boundary Layers with Distributed Injection", Ph.D. Thesis, Cambridge University (September 1966).
31. Jeromin, L., "An Experimental Investigation of the Compressible Turbulent Boundary Layer with Air Injection", Aeronautical Research Council of England, Report A.R.C. 28549 (November 1966).
32. Fernandez, F. and E. Zukoski, "Experiments in Supersonic Turbulent Flow with Large Distributed Surface Injection", AIAA J., 7, 1759 - 1767 (1969).
33. Martellucci, A., "Effects of Mass Transfer on Hypersonic Turbulent Boundary-Layer Properties", AIAA J., 10, 181-187 (1972).
34. Simpson, R., W. Kays and R. Moffat, "The Turbulent Boundary Layer on a Porous Plate: An Experimental Study of the Fluid Mechanics with Injection and Suction", Stanford University, Dept. of Mech. Engineering, Report No. MMT2 (1967).
35. Reeves, B., "Turbulent Mixing in Supersonic Flow Past Slender Bodies with Large Blowing", AGARD Conference Proceedings No. 4, AGARD Fluid Dynamics Panel Meeting on Separated Flows, Rhode-Saint-Genése, Belgium (May 1966).
36. Lees, L. and R. Chapkis, "Surface Mass Injection at Supersonic and Hypersonic Speeds as a Problem in Turbulent Mixing", AIAA J., 7, 671-680 (1969).

APPENDIX 1

MATCHING CONDITIONS

In addition to the law of the wall for U_m and the Crocco integral for H_m/H_w , matching relations for $(\partial u/\partial y)_m$ and $(\partial H/\partial y)_m$ are required to determine the exponents n and m of the power-law profiles in the outer layer. These are given below along with the expressions for τ_m , $(q + u\tau)_m$ and \dot{m} the mass flux in the inner layer. These expressions are applicable to a boundary layer growing into a rotational (variable entropy but constant stagnation temperature) inviscid flow.

From continuity of $(\partial u/\partial y)$ at y_m :

$$n = \frac{\rho_o}{\rho_s} (1 + m_e) \frac{\gamma + 1}{2(\gamma - 1)} \cdot \frac{(h_m/h_e)^{3/2} C_f^{1/2} \delta \beta_o^{1/2}}{K a^* y_m} \quad (A 1-1)$$

From continuity of $(\partial H/\partial y)$ at y_m :

$$m = \frac{(H_w/H_e) B a^* n}{1 - \bar{H}_m} \quad (A 1-2)$$

where

$$\bar{H}_m = (H_w/H_e)(1 + B \bar{U}_m), \quad h_m/h_e = \bar{H}_m + m_e (\bar{H}_m - \bar{U}_m^2) \quad (A 1-3)$$

$$\beta_o = \left(1 + \frac{M}{C_f} \bar{U}_m\right)^{1/2} \quad (A 1-4)$$

Stress at y_m (obtained by differentiating J_2 and inserting results into relation for τ_m :

$$\left. \begin{aligned} & (\rho_o/\rho_s)(1 + m_e) \frac{\gamma + 1}{2(\gamma - 1)} \left(\frac{a_o}{U_e^2 a_e \rho_o} \tau_m \right) - C_f = \\ & a_{01} \frac{d \bar{U}_m}{dx} + a_{02} \frac{d y_m}{dx} + a_{03} \frac{d C_f}{dx} + a_{04} \frac{d B}{dx} + a_{05} \frac{d M}{dx} \\ & + a_{06} \frac{d M_e}{dx} + a_{07} \frac{d}{dx} \left(\frac{\rho_s}{\rho_o} \right) + M \bar{U}_m \end{aligned} \right\} \quad (A 1-5)$$

where

$$a_{01} = \frac{J_1}{(h_w/h_e)} - \frac{\beta_3 C_f^{1/2} y_m}{(h_m/h_w)^{1/2}} \left[1 - \frac{\bar{U}_m (B - 2A^2 \bar{U}_m)}{2(h_m/h_w)} + \frac{\bar{U}_m M}{2\beta_o^2 C_f} \right] + \frac{2 y_m M}{K^2}$$

$$a_{02} = - \frac{\beta_3 C_f^{1/2} \bar{U}_m}{(h_m/h_w)^{1/2}} + \frac{2\beta_o^2 C_f}{K^2}$$

$$a_{03} = - \frac{\beta_3 \bar{U}_m y_m}{2(h_m/h_w)^{1/2} C_f^{1/2}} \left[1 - \frac{M \bar{U}_m}{\beta_o^2 C_f} \right] + \frac{2\beta_o^2 y_m}{K^2} - \frac{2 y_m M \bar{U}_m}{K^2 C_f}$$

$$a_{04} = \frac{\beta_3 C_f^{1/2} \bar{U}_m^2 y_m}{2(h_m/h_w)^{3/2}}$$

$$a_{05} = - \frac{\beta_3 \bar{U}_m^2 y_m}{2\beta_o^2 (h_m/h_w)^{1/2} C_f^{1/2}} + \frac{2 y_m \bar{U}_m}{K^2}$$

$$a_{06} = \frac{J_1 \bar{U}_m}{M_e (1+m_e) (h_w/h_e)} - \frac{y_m}{M_e (1+m_e)} + \frac{4 C_f y_m \beta_o^2}{K^2 M_e} \left[1 - \left(\frac{\gamma}{\gamma-1} \right) \frac{m_e}{(1+m_e)} \right]$$

$$- \frac{\bar{U}_m y_m \beta_o}{K M_e} \left[\frac{(H_e/H_w) C_f}{(1+m_e) (h_m/h_w)} \right]^{1/2} \left[2 - \frac{(3\gamma-1)}{(\gamma-1)} \frac{m_e}{(1+m_e)} + \frac{m_e}{(1+m_e)^2} \frac{(H_e/H_w) \bar{U}_m^2}{(h_m/h_w)} \right]$$

$$a_{07} = \left[- \frac{\bar{U}_m y_m \beta_o}{K} \left[\frac{(H_e/H_w) C_f}{(1+m_e) (h_m/h_w)} \right]^{1/2} + (2/K^2) C_f y_m \beta_o^2 \right] \frac{\rho_o}{\rho_s}$$

$$\beta_3 = \frac{\beta_o}{K} \left[\frac{H_e/H_w}{1+m_e} \right]^{1/2}$$

Heat flux at y_m (from equation for $(q + ur)_m$):

$$\left. \begin{aligned} & \left(\frac{1}{\rho_o U_e H_e} \right) q_m + \left(\frac{s_e}{\rho_o s_o H_e} \right) \bar{U}_m r_m = \\ & a_{11} \frac{d \bar{U}_m}{dx} + a_{12} \frac{d y_m}{dx} + a_{13} \frac{d C_f}{dx} + a_{14} \frac{d B}{dx} + a_{15} \frac{d M}{dx} \\ & + a_{16} \frac{d M_e}{dx} + a_{17} \frac{d}{dx} \left(\frac{\rho_s}{\rho_o} \right) + a_{18} St + a_{19} M \bar{U}_m \end{aligned} \right\} \quad (A 1-6)$$

where

$$a_{11} = \frac{\rho_s}{\rho_o} \left[- \frac{\beta_1 C_f^{1/2} y_m}{(h_m/h_w)^{1/2}} \left\{ 1 - \frac{\bar{U}_m (B - 2A^2 \bar{U}_m)}{2(h_m/h_w)} + \frac{\bar{U}_m M}{2\beta_o^2 C_f} \right\} + \beta_2 y_m M \right. \\ \left. + (1+m_e) \frac{1-3\gamma}{2(\gamma-1)} J_1 B \right]$$

$$a_{12} = \frac{\rho_s}{\rho_o} \left[- \frac{\beta_1 C_f^{1/2} \bar{U}_m}{(h_m/h_w)^{1/2}} + \beta_2 \beta_o^2 C_f \right]$$

$$a_{13} = \frac{\rho_s}{\rho_o} \left[- \frac{\beta_1 \bar{U}_m y_m}{2(h_m/h_w)^{1/2} C_f^{1/2}} \left(1 - \frac{\bar{U}_m M}{\beta_o^2 C_f} \right) + \beta_2 \beta_o^2 y_m - \beta_2 y_m M \bar{U}_m / C_f \right]$$

$$a_{14} = \frac{\rho_s}{\rho_o} \left[\frac{1-3\gamma}{(1+m_e) 2(\gamma-1)} (J_1 \bar{U}_m + J_2) + \frac{\beta_1 C_f^{1/2} \bar{U}_m^2 y_m}{2(h_m/h_w)^{3/2}} \right]$$

$$a_{15} = \frac{\rho_s}{\rho_o} \left[\beta_2 y_m \bar{U}_m - \frac{\beta_1 \bar{U}_m^2 y_m}{(h_m/h_w)^{1/2} C_f^{1/2}} \right]$$

$$a_{16} = \frac{\rho_s}{\rho_o} \left[\frac{\beta_2 C_f^{1/2} \beta_o^2}{M_e} \left\{ 1 - \left(\frac{\gamma+1}{\gamma-1} \right) \frac{m_e}{(1+m_e)} \right\} - \frac{\beta_1 C_f^{1/2} \bar{U}_m^3 y_m (H_e/H_w) (\gamma-1) M_e}{2(h_m/h_w)^{3/2} (1+m_e)^2} \right. \\ \left. - \frac{(H_w/H_e)^{1/2} B C_f^{1/2} \bar{U}_m y_m \beta_o}{K M_e (h_m/h_w)^{1/2}} (1+m_e) - \frac{\gamma}{\gamma-1} \left\{ 1 - \left(\frac{2\gamma}{\gamma-1} \right) \frac{m_e}{(1+m_e)} \right\} \right]$$

$$a_{17} = - \frac{\beta_1 C_f^{1/2} \bar{U}_m y_m}{(h_m/h_w)^{1/2}} + \beta_2 C_f \beta_o^2 y_m$$

$$a_{18} = 2(\rho_s/\rho_o) m_e (1+m_e) \frac{1-3\gamma}{2(\gamma-1)}$$

$$a_{19} = (\rho_s/\rho_o) (1+m_e) \frac{-(\gamma+1)}{2(\gamma-1)} (H_w/H_e) B$$

$$\beta_1 = (H_w/H_e)^{1/2} (1+m_e) \frac{-\gamma}{\gamma-1} (B \beta_o/K)$$

$$\beta_2 = 2(H_w/H_e) (1+m_e) \frac{-(\gamma+1)}{2(\gamma-1)} (B/K^2)$$

The mass flux in the inner layer is

$$\dot{m}/\rho_o U_e = \frac{1}{\rho_o U_e} \int_0^{y_m} \rho u dy = (\rho_s/\rho_o) (1+m_e) \frac{-(\gamma+1)}{2(\gamma-1)} \left[\frac{\bar{U}_m}{(h_m/h_e)} - \frac{C_f^{1/2} \beta_o}{K (h_m/h_e)^{1/2}} \right] y_m \quad (A 1-7)$$

Also, from the definition of B

$$\frac{dB}{dx} = \left(\frac{H_e}{H_w} \right) \left(\frac{2 m_e}{1+m_e} \right) \left[\frac{2 (St/C_f)}{M_e (1+m_e)} \frac{dM_e}{dx} + \frac{d}{dx} \left(\frac{St}{C_f} \right) \right] \quad (A 1-8)$$

The velocity ratio \bar{U}_m along the match point $y = y_m$ is found from the law of the wall, Eq. (26). Differentiating this equation with respect to x results in

$$\left. \begin{aligned} & a_{21} \frac{d\bar{U}_m}{dx} + a_{22} \frac{dy_m}{dx} + a_{23} \frac{dC_f}{dx} + a_{24} \frac{dB}{dx} + a_{25} \frac{dM}{dx} \\ & + a_{26} \frac{dM_e}{dx} + a_{27} \frac{dA^2}{dx} = \frac{\rho_o}{K \rho_s} \frac{d}{dx} \left(\frac{\rho_s}{\rho_o} \right) - \frac{1}{K r} \frac{dr}{dx} + \frac{d\bar{B}}{dx} \end{aligned} \right\} \quad (A 1-9)$$

where, for $k^2 = (C_2 - C_1)/(C_3 + C_2) < 1$,

$$a_{21} = (C_{21} H_w/H_e)^{-1/3} [(C_2 - \bar{U}_m)(\bar{U}_m - C_1)]^{-1/2} (\partial \mathcal{F}/\partial \theta)_{\xi} = \bar{U}_m$$

$$a_{22} = -1/K y_m$$

$$a_{23} = (1+m_e) A^2 C_{26}/C_{21} + C_{23}/M - 1/2 K C_f$$

$$a_{24} = \frac{B C_{22}}{A^2 (B^2 + 4 A^2)^{1/2}} + \left[1 + \frac{B}{(B^2 + 4 A^2)^{1/2}} \right] \left[\frac{C_{25}}{2 A^2} + \frac{C_{26}(1+m_e)M}{2 C_5} \right]$$

$$a_{25} = -C_{23} C_f/M^2 + (C_3 + C_2 - C_f/M) C_{26} (1+m_e) A^2/C_{21}$$

$$a_{26} = (\gamma-1) M_e A^2 M (C_3 + C_2) C_{26}/C_{21} - \left[1 - \left(\frac{2\gamma}{\gamma-1} \right) \left(\frac{m_e}{1+m_e} \right) \right] \frac{1}{k M_e}$$

$$a_{27} = \frac{C_{26}(1+m_e)M}{C_{21}} \left\{ (C_3 + C_2) - \frac{1}{2A^2} \left[B + \frac{B^2 + 2A^2}{(B^2 + 4A^2)^{1/2}} \right] \right\}$$

$$- \frac{C_{22}(B^2 + 2A^2)}{A^4(B^2 + 4A^2)^{1/2}} - \frac{C_{25}}{2A^4} \left[B + \frac{B^2 + 2A^2}{(B^2 + 4A^2)^{1/2}} \right]$$

and

$$C_{21} = (H_w/H_e)^{1/2} [(1+m_e)A^2 M(C_3 + C_2)]^{3/2}$$

$$C_{22} = -(C_{21} H_w/H_e)^{-1/3} \left\{ (C_3 + C_2)^{1/2} (C_2 - C_1)^{1/2} \left[\left(\frac{\partial \mathcal{F}}{\partial k} \right)_{\xi=\bar{U}_m} - \left(\frac{\partial \mathcal{F}}{\partial k} \right)_{\xi=0} \right] \right.$$

$$\left. - \frac{(C_2 - \bar{U}_m)^{1/2}}{(C_2 - C_1)(\bar{U}_m - C_1)^{1/2}} \left(\frac{\partial \mathcal{F}}{\partial \theta} \right)_{\xi=\bar{U}_m} + \frac{C_2^{1/2}}{(-C_1)^{1/2} (C_2 - C_1)} \left(\frac{\partial \mathcal{F}}{\partial \theta} \right)_{\xi=0} \right\}$$

$$C_{23} = (C_{21} H_w/H_e)^{-1/3} \left\{ (C_2 - C_1)^{1/2} (C_3 + C_2)^{-3/2} \left[\left(\frac{\partial \mathcal{F}}{\partial k} \right)_{\xi=\bar{U}_m} - \left(\frac{\partial \mathcal{F}}{\partial k} \right)_{\xi=0} \right] \right\}$$

$$C_{24} = a_{21}$$

$$C_{25} = C_{23} + (C_{21} H_w/H_e)^{-1/3} \left\{ (-C_1 C_2)^{-1/2} \left(\frac{\partial \mathcal{F}}{\partial \theta} \right)_{\xi=0} \right.$$

$$\left. - [(C_2 - \bar{U}_m)(\bar{U}_m - C_1)]^{-1/2} \left(\frac{\partial \mathcal{F}}{\partial \theta} \right)_{\xi=\bar{U}_m} \right\}$$

$$C_{26} = \mathcal{F}(\theta_{\xi=\bar{U}_m}, k) - \mathcal{F}(\theta_{\xi=0}, k)$$

$$\frac{\partial \mathcal{F}}{\partial \theta} = [1 - k^2 \sin^2 \theta]^{-1/2}$$

$$\frac{\partial \mathcal{F}}{\partial k} = \frac{\mathcal{E}(\theta, k) - (1 - k^2) \mathcal{F}(\theta, k)}{k(1 - k^2)} - \frac{k \sin \theta \cos \theta}{(1 - k^2)[1 - k^2 \sin^2 \theta]^{1/2}}$$

and $\mathcal{E}(\theta, k)$ is the elliptic integral of the second kind

$$\mathcal{E}(\theta, k) = \int_0^\theta [1 - k^2 \sin^2 \theta]^{1/2} d\theta$$

Also,

$$\frac{dA^2}{dx} = \frac{(\gamma - 1)M_e}{(H_w/H_e)(1 + m_e)^2} \frac{dM_e}{dx}$$

Differential equations for $d\bar{H}_m/dx$, dn/dx , dm/dx and $(1/\rho_0 U_e)(dm/dx)$ are also required as part of the system of equations to be solved, and are obtained by differentiating Eqs. (A 1-1), (A 1-2), (A 1-3), and (A 1-7), respectively.

Since all the differential equations obtained from the matching conditions are somewhat lengthy, a system of redundant checks has been built in to the computer program. The values of \bar{U}_m , \bar{H}_m , n , m and $\dot{m}/\rho_0 U_e$ calculated from the system of simultaneous differential equations are compared at each station with the values obtained from the associated algebraic equations for these quantities.

Two additional redundant checks are provided by overall momentum and energy integrals over the whole boundary layer.

The momentum integral equation is

$$\frac{d\theta}{dx} = - \left(2 + \frac{\delta^*}{\theta} - M_e^2 \right) \frac{\theta}{M_e(1 + m_e)} \frac{dM_e}{dx} - \frac{\theta \rho_0}{\rho_s} \frac{d}{dx} \left(\frac{\rho_s}{\rho_0} \right) + \frac{\tilde{C}_f}{2} + M \quad (\text{A 1-10})$$

and the energy integral equation is

$$\frac{d\theta_E}{dx} = - \frac{\theta_E(1 - M_e^2)}{M_e(1 + m_e)} \frac{dM_e}{dx} - \frac{\theta_E \rho_0}{\rho_s} \frac{d}{dx} \left(\frac{\rho_s}{\rho_0} \right) + \left(1 - \frac{H_w}{H_e} \right) (C_H + M) \quad (\text{A 1-11})$$

where

$$\theta_E \equiv \int_0^{\delta_e} \frac{\rho u}{\rho_e u_e} \left(1 - \frac{H}{H_e} \right) dy$$

which, when evaluated using the two-layer model, is

$$\theta_E = \frac{[1 - (H_w/H_e)(1 + B\bar{U}_m)] J_1}{(h_w/h_e)} - \frac{J_2 B}{(1 + m_e)} - \left(\frac{\rho_o}{\rho_s} \right) (1 + m_e)^{\frac{\gamma+1}{2(\gamma-1)}} E_4 \delta \quad (\text{A } 1-12)$$

Values of θ and θ_E obtained by integrating Eqs. (A 1-10) and (A 1-11) are compared with values computed using Eqs. (51) and (A 1-12) at each station. Special computer runs have been made using double precision computations with exceptionally tight error control in the simultaneous linear equation solver and in the Runge-Kutta integration. For these runs the algebraic relations for variables along the match point and for θ and θ_E agreed with the results computed from the differential equations to within nine significant figures.

APPENDIX 2

Integral functions for integral moment equations in outer layer:

$$A_1 = \frac{2a^*}{2n+1} - \frac{1}{n+1}$$

$$A_2 = \frac{a^*}{(n+1)^2} - \frac{2a^{*2}}{(2n+1)^2}$$

$$A_3 = \frac{-3a^{*2}}{3n+1} + \frac{6a^*}{2n+1} - \frac{2}{n+1}$$

$$A_4 = \frac{3a^{*3}}{(3n+1)^2} - \frac{6a^{*2}}{(2n+1)^2} + \frac{2a^*}{(n+1)^2}$$

$$B_1 = \frac{1}{m+1} - \frac{a^*}{(m+n+1)}$$

$$B_2 = \frac{(1-\bar{H}_m)}{(m+1)^2} - \frac{a^*(1-\bar{H}_m)}{(m+n+1)^2}$$

$$B_3 = \frac{(1-\bar{H}_m)}{(m+n+1)}$$

$$B_4 = \frac{-a^*(1-\bar{H}_m)}{(m+n+1)^2}$$

$$E_1 = \int_0^1 \bar{H} d\eta = 1 - \frac{(1-\bar{H}_m)}{1+m}$$

$$E_2 = \int_0^1 U \bar{H} d\eta = 1 - \frac{a^*}{n+1} - \frac{(1-\bar{H}_m)}{m+1} + \frac{a^*(1-\bar{H}_m)}{m+n+1}$$

$$E_3 = \int_0^1 U^2 \bar{H} d\eta =$$

$$1 - \frac{2a^*}{n+1} + \frac{a^{*2}}{2n+1} - \frac{(1-\bar{H}_m)}{m+1} + \frac{2a^*(1-\bar{H}_m)}{m+n+1} - \frac{a^{*2}(1-\bar{H}_m)}{2n+m+1}$$

$$E_4 = \int_0^1 \bar{U}(\bar{H}-1) d\eta = (1-\bar{H}_m) \left(\frac{a^*}{m+n+1} - \frac{1}{m+1} \right)$$

$$I_1 = \int_0^1 \bar{U} d\eta = 1 - \frac{a^*}{n+1}$$

$$I_2 = \int_0^1 \bar{U}^2 d\eta = 1 - \frac{2a^*}{n+1} + \frac{a^{*2}}{2n+1}$$

$$I_3 = \int_0^1 \bar{U}^3 d\eta = 1 - \frac{3a^*}{n+1} + \frac{3a^{*2}}{2n+1} - \frac{a^{*3}}{3n+1}$$

$$I_4 = \int_0^1 \bar{U}^4 d\eta = 1 - \frac{4a^*}{n+1} + \frac{6a^{*2}}{2n+1} - \frac{a^{*4}}{4n+1}$$

$$I_5 = \int_0^1 \bar{U}(\bar{U}-1) d\eta = -\frac{a^*}{n+1} + \frac{a^{*2}}{2n+1}$$

$$I_6 = \int_0^1 \bar{U}(\bar{U}^2-1) d\eta = -\frac{2a^*}{n+1} + \frac{3a^{*2}}{2n+1} - \frac{a^{*3}}{3n+1}$$

APPENDIX 3

ENTRAINMENT AND OTHER SWALLOWING RELATIONSHIPS

For flow around blunt bodies at angle of attack the streamline locations and metrics are calculated using the method developed by Fannelop and Waldman⁴. In this calculation the local entropy (or stagnation density ratio ρ_s/ρ_o) is related to the mass flow entrained by the boundary layer between neighboring inviscid streamlines. If \dot{m}_e is the mass flow entrained by the boundary layer between two inviscid streamlines, which are separated by a distance r ,

$$\dot{m}_e = r \int_0^{\tilde{\delta}_e} \tilde{\rho} \tilde{u} d\tilde{y} - \int_0^{\tilde{x}} \rho_w \tilde{v}_w r d\tilde{x} \quad (A 3-1)$$

It is assumed here that no mass is injected or ablated into the boundary layer upstream of $\tilde{x} = 0$ which is the station where the turbulent boundary layer begins. Eq. (A 3-1) can be written

$$\frac{\dot{m}_e}{\rho_o a_o L} = \left(\frac{\rho_s}{\rho_o} \right) M_e (1+m_e)^{\frac{-(\gamma+1)}{2(\gamma-1)}} \left\{ \frac{\bar{U}_m y_m}{(h_m/h_e)} - \frac{C_f^{1/2} y_m \beta_o}{K (h_m/h_e)^{1/2}} - \int_0^{\tilde{x}} M dx \right\} + \dot{M}_e \delta l_1 \quad (A 3-2)$$

The local Reynolds number base on momentum thickness is

$$Re_{\tilde{\theta}} = \frac{\tilde{u}_e \tilde{\theta}}{\nu_e} = \frac{\rho_o a_o}{\mu_o} \left(\frac{\rho_s}{\rho_o} \right) M_e (1+m_e)^{\sigma - \frac{\gamma+1}{2(\gamma-1)}} \tilde{\theta} \quad (A 3-3)$$

while the local heat flux and shear stress along the surface are

$$\frac{q_w}{H_o a_o \rho_o} = \left(\frac{\rho_s}{\rho_o} \right) M_e (1+m_e)^{-\frac{\gamma+1}{2(\gamma-1)}} \left(1 - \frac{H_w}{H_e} \right) C_H \quad (A 3-4)$$

$$\frac{\tau_w}{\rho_o a_o^2} = \frac{1}{2} \left(\frac{\rho_s}{\rho_o} \right) M_e^2 (1+m_e)^{\frac{-\gamma}{\gamma-1}} \tilde{C}_f \quad (A 3-5)$$